SECTION I

AN ANALYTICAL AND EXPERIMENTAL STUDY OF SOME SIMPLE GEOLOGIC STRUCTURES

SECTION II

GRAVITY SURVEY OF A PART OF THE RAYMOND AND SAN GABRIEL BASINS, SOUTHERN CALIFORNIA

Thesis by

Allan Robert Sanford

In Partial Fulfillment of the Requirements

For the Degree of

Doctor of Philosophy

California Institute of Technology

Pasadena, California

1958

ACKNOWLEDGEMENTS

Several people and organizations have contributed information and suggestions which have greatly aided the writer in his research. In particular, the author is indebted to Professor C. H. Dix of the California Institute of Technology under whose guidance this research was conducted, and to Professor C. R. Allen, also of the California Institute of Technology, who has read this thesis and made many useful suggestions. The writer is also indebted to Mr. E. L. Smith of the Pasadena Water Department who supplied nearly all of the sub-surface geologic information used in the interpretation of the gravity data. Finally the author wishes to express his appreciation to the Standard Oil Company of California for the aid received through their fellowship for a period of two years.

ABSTRACT

SECTION I

The geologic structures produced by two distributions of applied vertical displacement along the base of a homogeneous layer, (1) a broad curve and (2) a sharp step, were investigated analytically and experimentally. A special form of the general theory of elasticity and scale models (with layers of dry sands and clay) were used for a two dimensional analytical and experimental study of these structures.

Each of the two distributions of applied vertical displacement produce a characteristic fracture pattern in the model experiments. For a broad curve, the fracture pattern is a complex zone of normal faults which taper inward to the axis of the fold and die out at depth. For a sharp step, the fracture pattern is (1) a series of curved reverse faults which start steeply at the base of the layer but intersect the upper surface at low angles (thrusts), and (2) a series of normal faults in the uplifted block near the reverse faults.

The initial fractures in the model experiments, for example the curved reverse faults, can be predicted on the basis of the Mohr fracture criterion and the stress distributions found in the elastic analyses. In addition, the displacement fields obtained in the elastic analyses are good first order approximations of the displacement fields observed in the model experiments.

SECTION II

A gravity survey (640 stations) was conducted over thirty-six square miles of the alluvium covered portion of the Raymond and San Gabriel basins. Corrections for latitude, elevation, and topography were applied to the gravity data. On the basis of the known surface and sub-surface geology, regional gravity due to deep crustal structure, and gravity due to near surface structure were separated and interpreted independently.

The regional gravity due to deep crustal structure indicates a uniform thickening of the earth's crust to the northeast. If all of the regional gravity is attributed to a density difference of 0.5 c.g.s. at the Mohorovicic discontinuity, the rate of thickening is about 100 meters per kilometer.

The distribution of gravity due to near surface structure shows two steep gradient valleys in the bedrock surface beneath the alluvium in the northern part of the area. The elevation to the floor of these valleys indicates at least 1000 feet of subsidence since the deposition of the alluvium (Upper Pleistocene). The bedrock relief is fairly gentle in the southern part of the area where Tertiary rock lies between bedrock and alluvium. This intermediate layer of Tertiary rock may extend more than a mile north of the Raymond fault. The vertical displacement on the Raymond fault may be 600 feet along one section of the fault in east Arcadia.

TABLE OF CONTENTS

SECTION I

SECTION II

TABLE OF CONTENTS (Cont'd)

ILLUSTRATIONS

SECTION I

ILLUSTRATIONS (Cont'd)

ILLUSTRATIONS (Cont'd)

SECTION II

TABLES

SECTION I

SECTION II

SECTION I

AN ANALYTICAL AND EXPERIMENTAL STUDY OF SOME SIMPLE GEOLOGIC STRUCTURES

INTRODUCTION

Many of the faults and folds observed in the sedimentary basins of the world are the result of differential vertical movements in the "basement" rock underlying these basins. A study of geologic structures arising in this manner was started by the writer in 1954. Deformation resulting from simple distributions of vertical displacement along the bases of homogeneous layers were investigated analytically and experimentally. A special form of the general theory of elasticity was used in the analytical work. Scale models with homogeneous layers of dry sands and clay were used in the experimental work.

The principal purposes of the investigation were to determine:

1. The character of the folding and faulting produced by simple two dimensional distributions of applied vertical displacement at the base of a homogeneous layer.
2. The similarity, if any, between a two dimensional elastic analysis and a two dimensional scale model experiment of the same physical situation.

The physical situations investigated analytically and experimentally were simple idealized representations of actual conditions in a sedimentary basin. However, investigation of these simple situations was a necessary first step towards an understanding of the more complex problems in nature.

ANALYTICAL STUDY

Introduction

This section describes the method used and the results obtained in the analytical investigation of deformation resulting from differential vertical movement along the lower boundary of a homogeneous layer. In the analytical method employed in this study, simple distributions of vertical displacement are specified along the base of a homogeneous elastic layer. The method is similar to one used by Hafner (1951) to describe the reaction of a homogeneous elastic layer to applied stresses rather than displacements along the lower boundary of the layer. There is no appreciable difference between the two methods when applied to simple geologic situations such as folding of a layer. However, there are certain structures where one or the other is superior in representing the physical problem.

Block faulting of sedimentary layers above a rigid basement is an example of a structural problem which can be represented best by specifying displacements. In simple examples of this type of structure, adjacent blocks of basement rock are moved uniformly up or down with respect to each other. The overlying layer is undeformed by the movement except in the region where the two blocks meet. There is no way of measuring the magnitude or distribution of stress along the base of the layer in the zone of deformation. The best analytical representation can be made by using the only available information--the displacements.

There is an additional reason for using an analytical method based on displacements along the base of an elastic layer. The only parameter that can be measured with any degree of accuracy in the structural scale model experiments is the displacement. A comparison between model experiments and elastic analyses is easiest when displacements similar to those used in the experiments are specified in the elastic analyses.

Theory

General Theory

The analytical method used in the study is based on the theory of elasticity for arbitrarily small strains (Timoshenko and Goodier, 1951; Love, 1944; Muskhelishvili, 1953). Several assumptions are made in this specialized theory of elasticity which restrict its application to problems that are only idealized representations of structural problems in geology. First, the displacements in the deformed layer must be arbitrarily small; so that second order strain terms can be neglected, and so that the specified boundary conditions and body forces can be considered unchanged by deformation. Second, the material undergoing deformation must be perfectly elastic (recover its initial form after removal of stresses), linearly elastic (possess a linear relationship between stress and strain), homogeneous (possess the same specific properties throughout its volume), and isotropic (possess elastic properties which are the same in all directions). The last two conditions require that no fractures and no stresses other than hydrostatic exist within the layer prior to deformation.

Even with the above simplifying assumptions, the direct application of the theory of elasticity to three dimensional problems of geologic interest remains difficult. However, a simplification of this analytical work is possible within the framework of the theory. This simplification is made by assuming that one horizontal dimension (Z) of the layer is much longer than the other (X) (see fig. 1). If the lower surface of the layer undergoes displacements which vary only in the X-Y plane and are constant along the Z axis, then all X-Y cross sections are in the same condition. Inasmuch as all cross sections are in the same condition, a two dimensional analysis of a single cross section will describe the stresses and displacements along the length of the Z axis. With this procedure, it is possible to analyze two dimensional situations similar to cross sections near the center of elongated geologic structures.

The determination of stress and strain in a cross section through a deformed elastic layer is a boundary value problem. Stresses or displacements must be specified along the boundaries of the layer in order to find the stress and strain values within the layer when it is in elastic equilibrium. The boundary conditions can be expressed in terms of stress only, displacement only, or stress along one portion of the boundary and displacement along the remainder (mixed boundary conditions). The reaction of a homogeneous elastic layer to small displacements along its lower boundary requires mixed boundary conditions; stresses are specified along the upper boundary and displacements

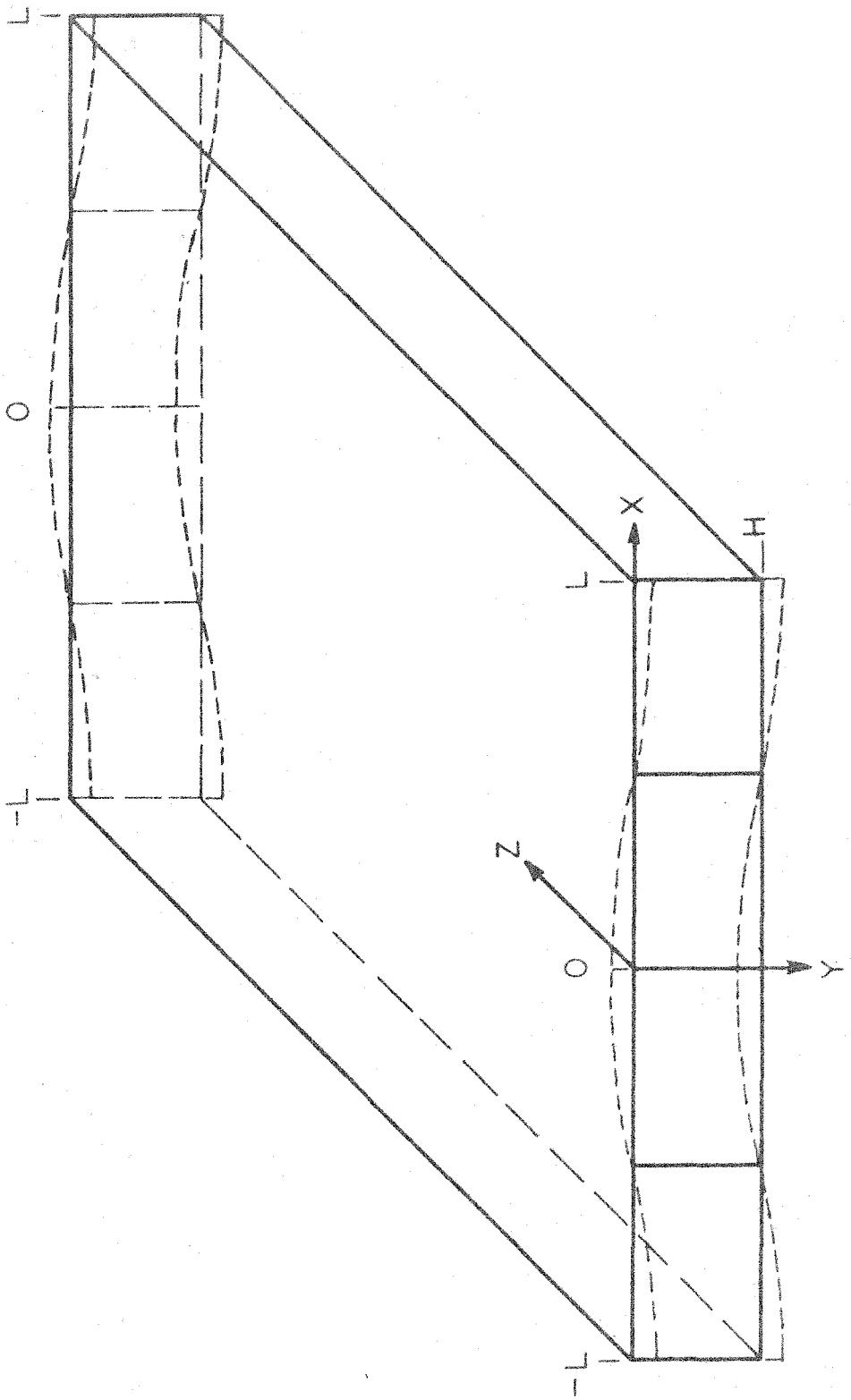

Figure 1. Coordinates for the elastic problems

along the lower boundary. The analytical procedure for solution of mixed boundary value problems of geologic interest differs from methods previously discussed in the geologic literature.

Nomenclature

The nomenclature that is used in the following derivation of the analytical method is listed below. The notation is the same as that of Timoshenko and Goodier (1951, p. xvii).

$\sigma_x, \sigma_y, \sigma_z$	Normal components of stress parallel to the X, Y, and Z axes.
τ_{xy}	Shearing stress component.
$\sigma_1, \sigma_2, \sigma_3$	Maximum, intermediate, and minimum principal stresses.
u, v	Components of displacement in the X and Y directions.
$\varepsilon_x = \frac{\partial u}{\partial x}$ $\varepsilon_y = \frac{\partial v}{\partial y}$	Unit elongations in the X and Y directions (strains).
$\gamma_{xy} = \frac{\partial u}{\partial y} + \frac{\partial v}{\partial x}$	Shearing strain.
G	Modulus of rigidity.
ν	Poisson's ratio.
λ	Lame's constant.
$K_1 = \frac{\lambda + 2G}{G} = \frac{2(1-\nu)}{1-2\nu}$	Constant used in this paper.
$K_3 = 1 - K_1 = -\frac{1}{1-2\nu}$	Constant used in this paper.
ρ	Density
g	Gravitational acceleration.
$\nabla^2 = \frac{\partial^2}{\partial x^2} + \frac{\partial^2}{\partial y^2}$	Laplacian operator.
$\alpha = \frac{m\pi}{L}$	Coefficient.
Ed	Distortional strain energy density.
H	Thickness of the elastic layer.

L	Distance between points of zero vertical displacement.
B_c	Critical displacement--the maximum amount of displacement without fracture.
σ	Normal stress across a potential fracture plane.
τ	Shearing stress across a potential fracture plane.
τ_o	Shear stress necessary to overcome the initial shear strength due to cohesion.
ϕ	Angle of internal friction.
θ	Angle between line of fracture and principal stress.

Derivation of the Analytical Method

The solution of any two dimensional elastic problem must satisfy the following equations (Timoshenko and Goodier, 1951, pp. 11-27):

$$\frac{\partial \sigma_x}{\partial x} + \frac{\partial \tau_{xy}}{\partial y} = 0 , \tag{1}$$

$$\frac{\partial \sigma_y}{\partial y} + \frac{\partial \tau_{xy}}{\partial x} = 0 , \tag{2}$$

$$\nabla^2 (\sigma_x + \sigma_y) = 0 . \tag{3}$$

Equations (1) and (2) are the differential equations of equilibrium which insure a state of static equilibrium. Equation (3) is the compatibility equation (expressed in terms of stress) which insures a proper relationship between the three components of strain so that two dimensional deformation can occur without discontinuities in displacement (Muskhelishvili, 1953, pp. 95-97). In addition to satisfying equations (1) through (3), the solution must satisfy specified

stress and/or displacement boundary conditions. If the solution of the problem gives stresses and displacements which fulfill all these conditions, then it can be shown that the solution is unique (Timoshenko and Goodier, 1951, p. 236; Muskhelishvili, 1953, pp. 66-71).

The stresses appearing in equations (1) through (3) are related to the strains in the following manner:

$$\sigma_x = \lambda\left(\frac{\partial u}{\partial x} + \frac{\partial v}{\partial y}\right) + 2G\,\frac{\partial u}{\partial x}, \tag{4}$$

$$\sigma_y = \lambda\left(\frac{\partial u}{\partial x} + \frac{\partial v}{\partial y}\right) + 2G\,\frac{\partial v}{\partial y}, \tag{5}$$

$$\tau_{xy} = G\left(\frac{\partial u}{\partial y} + \frac{\partial v}{\partial x}\right). \tag{6}$$

Rewriting equations (1) through (3) in terms of strains gives:

$$(\lambda+G)\frac{\partial}{\partial x}\left(\frac{\partial u}{\partial x} + \frac{\partial v}{\partial y}\right) + G\nabla^2(u) = 0, \tag{7}$$

$$(\lambda+G)\frac{\partial}{\partial y}\left(\frac{\partial u}{\partial x} + \frac{\partial v}{\partial y}\right) + G\nabla^2(v) = 0, \tag{8}$$

$$\nabla^2\left[2(\lambda+G)\left(\frac{\partial u}{\partial x} + \frac{\partial v}{\partial y}\right)\right] = 0. \tag{9}$$

The displacements can be expressed as algebraic sums of partial derivatives of a scalar potential $\phi(x, y)$, and a vector potential $\psi(x, y)$, in the following way (Phillips, 1933, p. 186):

$$u = \frac{\partial \phi}{\partial x} + \frac{\partial \psi}{\partial y}, \tag{10}$$

$$v = \frac{\partial \phi}{\partial y} - \frac{\partial \psi}{\partial x}. \tag{11}$$

Substituting derivatives of equations (10) and (11) into equations (7) and (8) gives the equations of equilibrium in terms of the two

potentials:

$$(\lambda+2G)\frac{\partial}{\partial x}(\nabla^2\phi) + G\frac{\partial}{\partial y}(\nabla^2\psi) = 0, \tag{12}$$

$$(\lambda+2G)\frac{\partial}{\partial y}(\nabla^2\phi) - G\frac{\partial}{\partial x}(\nabla^2\psi) = 0. \tag{13}$$

Differentiating equation (12) with respect to "x" and equation (13) with respect to "y", and adding the two equations gives:

$$\nabla^2(\nabla^2\phi) = 0 . \tag{14}$$

Similarly, differentiating equation (12) with respect to "y" and equation (13) with respect to "x", and subtracting one equation from the other gives:

$$\nabla^2(\nabla^2\psi) = 0. \tag{15}$$

Equations (14) and (15) require that ϕ and ψ be either harmonic ($\nabla^2\phi = 0$) or biharmonic functions ($\nabla^4\phi = 0$). Substitution of partial derivatives of equations (10) and (11) into the equations for σ_x and σ_y (equations 4 and 5), and summing the results gives:

$$\sigma_x + \sigma_y = 2(\lambda+G)\nabla^2\phi. \tag{16}$$

The sum of σ_x and σ_y is zero when ϕ is a harmonic function. This condition can not be satisfied by deformed layers (for example, at a free surface where $\sigma_y \equiv 0$ everywhere and σ_x has finite values). Therefore ϕ must be a biharmonic function.

The solutions adopted for ϕ and ψ must satisfy the biharmonic differential equations and prescribed boundary conditions.

The specific problem of interest here is the deformation of an elastic layer of thickness "H" which has the following stresses and displacements specified on its boundaries:

At Y = 0, $\sigma_y = 0$, and $\tau_{xy} = 0$ (Stresses zero);

At Y = H, $v = -B\cos\alpha x$, and $u = BP\sin\alpha x$,

where $0 \leq P < 1$.

The lower surface of the layer undergoes vertical and horizontal displacements proportional to the cosine and sine, respectively. Assume for the moment that the vertical and horizontal displacements within the layer are also proportional to the cosine and sine. Equations (10) and (11), which express displacements in terms of the potential functions, indicate that the above distribution of displacements may be possible with potential functions of the form:

$$\phi = \cos\alpha x \, F(y), \tag{17}$$

$$\psi = \sin\alpha x \, f(y). \tag{18}$$

At this point, there is no guarantee that equations (17) and (18) will lead to a solution of the problem. Equations (17) and (18) are the correct expressions for the potential functions only if the stresses and displacements derived from them satisfy equations (1) through (3) and the prescribed boundary conditions.

F(y) and f(y) can be determined by substituting equations (17) and (18) into equations (14) and (15) and solving the resulting fourth order differential equations. This leads to general

expressions for ϕ and ψ :

$$\phi = \cos\alpha x \left[A_1 e^{\alpha y} + A_2 y e^{\alpha y} + A_3 e^{-\alpha y} + A_4 y e^{-\alpha y}\right], \tag{19}$$

$$\psi = \sin\alpha x \left[A_5 e^{\alpha y} + A_6 y e^{\alpha y} + A_7 e^{-\alpha y} + A_8 y e^{-\alpha y}\right], \tag{20}$$

where A_1 through A_8 are arbitrary constants.

Note that equations (19) and (20) contain eight arbitrary constants, whereas only four boundary conditions are specified in the problem. Four extra arbitrary constants appear in the equations for the potential functions as a result of (1) expressing the displacements as partial derivatives of potential functions (equations 10 and 11), and (2) differentiating the equations of equilibrium to obtain the two biharmonic equations. Some of the constants in the general expressions for ϕ and ψ must be related in order to satisfy the equations of equilibrium. Substituting equations (19) and (20) into equations (12) and (13) gives:

$$A_6 = \left(\frac{\lambda+2G}{G}\right) A_2 = \frac{2(1-\nu)}{1-2\nu} A_2 = K_1 A_2 , \tag{21}$$

$$A_8 = -\left(\frac{\lambda+2G}{G}\right) A_4 = -\frac{2(1-\nu)}{1-2\nu} A_4 = -K_1 A_4 . \tag{22}$$

These relationships eliminate two of the extra constants.

The remaining two extra constants must be eliminated by trial and error until equations for ϕ and ψ are found which satisfy the four boundary conditions, and the equations of equilibrium and compatibility. The equations for ϕ and ψ satisfying the requirements for a solution of stress and strain in the elastic layer are:

$$\phi = \cos\alpha x \left[A_1 (e^{\alpha y} + e^{-\alpha y}) + A_2 y e^{\alpha y} + A_4 y e^{-\alpha y} \right], \tag{23}$$

$$\psi = \sin\alpha x \left[A_5 (e^{\alpha y} + e^{-\alpha y}) + K_1 A_2 y e^{\alpha y} - K_1 A_4 y e^{-\alpha y} \right]. \tag{24}$$

The constants in the above equations are equal to:

$$A_1 = 0$$

$$A_2 = \frac{B\alpha C_2}{N} = \frac{B\alpha}{N} \left\{ K_3 \left[(1-P) e^{\alpha H} - (1+P)(1+2\alpha H) e^{-\alpha H} \right] - 2(K_1 - P) e^{-\alpha H} \right\}, \tag{25}$$

$$A_4 = \frac{B\alpha C_4}{N} = \frac{B\alpha}{N} \left\{ K_3 \left[(1+P) e^{-\alpha H} + (1-P)(2\alpha H - 1) e^{\alpha H} \right] - 2(K_1 + P) e^{\alpha H} \right\}, \tag{26}$$

$$A_5 = \frac{BC_5}{N} = -\frac{BK_3}{N} \left\{ (K_1 + H\alpha P K_3)(e^{\alpha H} + e^{-\alpha H}) + (P - H\alpha K_3)(e^{\alpha H} - e^{-\alpha H}) \right\}, \tag{27}$$

where

$$N = \alpha N' = \alpha \left\{ K_3 (2 - e^{2\alpha H} - e^{-2\alpha H}) - K_1 K_3 (2 + e^{2\alpha H} + e^{-2\alpha H}) + 4\alpha^2 H^2 K_3^2 + 4K_1 \right\}, \tag{28}$$

and $$K_3 = (1 - K_1) = \frac{1}{1 - 2\nu} \, . \tag{29}$$

The general equations for v, u, σ_y, σ_x, and τ_{xy} are:

$$v = \frac{B\cos\alpha x}{N'} \left\{ C_2 e^{\alpha y} [y\alpha K_3 + 1] - C_4 e^{-\alpha y} [y\alpha K_3 - 1] - C_5 [e^{\alpha y} + e^{-\alpha y}] \right\}, \tag{30}$$

$$u = \frac{B\sin\alpha x}{N'} \left\{ -C_2 e^{\alpha y} [y\alpha K_3 - K_1] - C_4 e^{-\alpha y} [y\alpha K_3 + K_1] + C_5 [e^{\alpha y} - e^{-\alpha y}] \right\}, \tag{31}$$

$$\sigma_y = \frac{2GB\alpha\cos\alpha x}{N'} \left\{ C_2 K_3 \alpha y e^{\alpha y} + C_4 K_3 \alpha y e^{-\alpha y} - C_5 (e^{\alpha y} - e^{-\alpha y}) \right\}, \tag{32}$$

$$\sigma_x = -\sigma_y + \frac{2GB\alpha\cos\alpha x}{N'} \left\{ -2K_3 [C_2 e^{\alpha y} - C_4 e^{-\alpha y}] \right\}, \tag{33}$$

$$\tau_{xy} = \frac{2GB\alpha\sin\alpha x}{N'} \left\{ C_5 (e^{\alpha y} + e^{-\alpha y}) - C_2 K_3 e^{\alpha y} [\alpha y + 1] + C_4 K_3 e^{-\alpha y} [\alpha y - 1] \right\}. \tag{34}$$

The remaining equations of interest in an elastic analysis are those for the principal stresses. The principal stresses at a point within a stressed layer are the stress values normal to three perpendicular planes across which the shearing stresses vanish. In a two dimensional analysis, the intermediate principal stress (σ_2) is always parallel to the Z axis. The equations for the principal stresses are found by the following relationships between σ_x, σ_y, and τ_{xy} :

$$\sigma_1 = \frac{\sigma_x+\sigma_y}{2} + \sqrt{\left(\frac{\sigma_x-\sigma_y}{2}\right)^2+\tau_{xy}^2}\,, \tag{35}$$

$$\sigma_3 = \frac{\sigma_x+\sigma_y}{2} - \sqrt{\left(\frac{\sigma_x-\sigma_y}{2}\right)^2+\tau_{xy}^2}\,. \tag{36}$$

Superposition of Solutions

The reaction of an elastic layer to general distributions of displacement along its lower boundary can be determined by superposing several solutions of the type shown above (Timoshenko and Goodier, 1951, p. 235). Combination of solutions is accomplished by means of a Fourier series, which can be used to approximate a variety of geologically reasonable displacements at the base of a sedimentary layer.

Superposition is also used to incorporate into the solutions an initial state of stress due to the weight of the layer. A state of hydrostatic stress:

$$\sigma_x = -\rho g y\,,\quad \sigma_y = -\rho g y\,,\quad \text{and}\quad \tau_{xy} = 0\,,$$

which satisfies the equilibrium and compatibility requirements, can be superposed with stresses arising from the deformation of

the layer. This superposition of solutions gives the correct stress values for layers which are assumed to be in a state of hydrostatic equilibrium prior to deformation.

Restrictions on the Analytical Method

Arbitrarily small displacements are a mathematical restriction on the theory of elasticity arising from the exclusion of higher order strain terms in the relationships between stress and strain (equations 4 through 6). This restriction has been violated in the examples discussed later in the paper by specifying small finite displacements along the lower boundary of a homogeneous elastic layer. The errors introduced by considering finite displacements will be small if the displacements are made small. Later in the paper it will be shown that fracture imposes a small upper limit to the amount of applied displacement along the lower boundary.

The fact that the boundary conditions and the body force are specified only for the initial condition of the layer also places a restriction on the magnitude of applied displacement. In these problems, the boundary conditions and body force ($-\rho gy$) are specified for a flat homogeneous layer. After deformation, the boundary conditions and body forces are changed because the layer is no longer flat or homogeneous. If the displacements are made small, these changes will be insignificant and can be disregarded.

Application of the Analytical Method to Examples

Stress Distribution

The internal stress distribution of a deformed elastic layer can be portrayed by a set of orthogonal curves called stress

trajectories. These stress trajectories are tangent to the principal stresses at all points within the layer. The equations for the direction of one of the principal stresses (σ_1 or σ_3) in the two dimensional case is:

$$\tan 2\beta = \frac{2\tau_{xy}}{\sigma_x - \sigma_y} . \qquad (37)$$

β is the angle between the positive X axis and the principal stress measured in the direction of the positive Y axis. In the numerical examples discussed below, β values were found for a grid of points within the layer. A graphical construction of the stress trajectories was made on the basis of the contoured values of β.

For specified displacements and stresses on the boundaries of an elastic layer, the only factors which will influence the orientations of the stress trajectories are the shape of the layer and Poisson's ratio for the material. Rigidity (G), maximum applied vertical displacement (B), and hydrostatic stress cancel out of equation (37). The shape of the layer and Poisson's ratio appear in the stress equations through the constants K_3, C_2, C_4, and C_5, and therefore can not be eliminated in equation (37).

Displacement Field

The distribution of displacement in a deformed layer can be portrayed by a field of displacement vectors. The orientation and length of each vector indicate the direction and magnitude of the net displacement at the point from which the vector originates.

For specified displacements and stresses on the boundaries

of an elastic layer, the only factors which will influence the orientations of the displacement vectors are the shape of the layer and Poisson's ratio for the material. The maximum applied vertical displacement (B), which appears in both displacement equations, has no influence because orientation of the vectors is determined by the ratio of the displacements. Rigidity (G) does not appear in displacement equations. The shape of the layer and Poisson's ratio enter into the displacement expressions through constants K_1, K_3, C_2, C_4, and C_5.

Critical Displacement and Fracture

In numerical examples, it is desirable to have a method of assigning magnitudes of applied displacement so that a comparison of stress distributions and displacement fields in different examples is possible. Initiation of fracture within the deformed elastic layer was used in this work to place a limit on the applied displacement. In each numerical example considered below, the elastic layer undergoes an applied displacement which is just necessary to cause fracture.

The critical displacements (Bc), for initiating fracture in each example, were based on a special case of the Mohr fracture criterion (Jaeger, 1956, pp. 80-83). The equation for this fracture criterion is:

$$\tau = \tau_o - \sigma \tan\phi , \tag{38}$$

where τ and σ are the shearing and normal stresses across a potential fracture plane, τ_o is the shear stress necessary to

overcome the initial shear strength due to cohesion, and ϕ is the angle of internal friction. The same criterion is shown diagrammatically in fig. 2. Note that the strength is less under tensile stress and that confining stress (hydrostatic stress) increases the strength.

This special form of the Mohr criterion was selected because it satisfactorily describes the short term shear strength of many sedimentary rocks under the confining pressures normally encountered in sedimentary basins (1000 to 2000 kg/cm^2) (Jaeger, 1956, p. 82). In addition, the linear relationship between shear and normal stresses is easier to treat analytically than other fracture criteria. The Mohr criterion explains shear fracture of rock specimens subjected to axial compression and hydrostatic pressure in the perpendicular directions. However, the criterion may not explain brittle or tensile fracture of rock specimens subjected to tensile stresses. Unfortunately, many of the initial fractures in this work are tensile cracks perpendicular to the direction of a tensile stress. At the present time, there is inadequate experimental data to establish a fracture criterion for rocks under tension. As a result, the Mohr criterion was used in this work for failure under tensile as well as compressive stresses.

The adoption of a short term strength criterion was required because of the type of analysis used. The stresses computed in the analytical work for a given applied displacement remain unchanged with time. Removal of stress concentrations by plastic flow is not considered in an elastic analysis. Therefore,

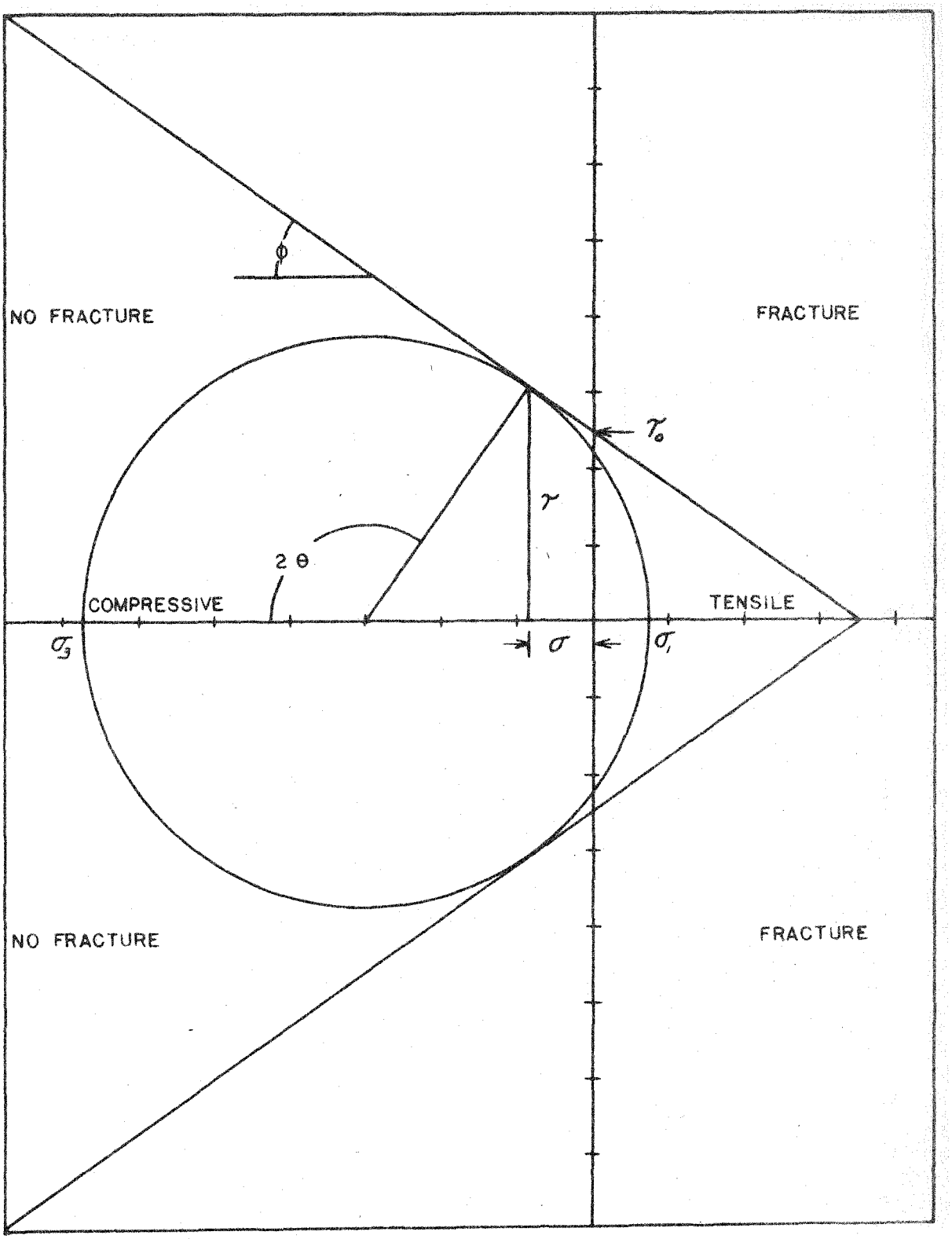

Figure 2. Diagram of the Mohr fracture criterion.

an elastic analysis can only be applied to geologic events which give rise to short term stresses. One event in nature which satisfies these conditions is rapid displacement of a rigid basement at the base of a sedimentary layer. The criterion adopted to explain fracture under the above conditions must be based on the short term strength characteristics of the layer.

The procedure used to determine critical displacements in the numerical examples was as follows:

1. The values of the principal stresses were computed as fractions of the maximum applied vertical displacement (B) for a grid of points in the layer.
2. The point most susceptible to fracture was determined by plotting the stress values as fractions of B in a Mohr diagram (fig. 2).
3. The critical displacement (Bc) necessary for fracture was found by substituting the principal stress values (expressed as fractions of B) for the point determined above into a rearranged form of equation (38):

$$\left|\frac{\sigma_1-\sigma_3}{2}\right| = \tau_0 \cos\phi - \left(\frac{\sigma_1+\sigma_3}{2}\right)\sin\phi \ . \qquad (39)$$

The critical displacement found by equation (39) is dependent on the value of the principal stresses (expressed as fractions of B) and the fracture characteristics of the material (denoted by the cohesion--τ_0, and the angle of internal friction--ϕ). The principal stress values are in turn dependent on the rigidity (G), Poisson's ratio (ν), and the dimensions of the layer. Therefore, in

the case of specified displacements and stresses on the boundaries of an elastic layer, the critical displacement is a function of both elastic and fracture properties of the layer.

Yielding by Flow

The Mohr criterion satisfactorily represents shear fracture of brittle materials. However, not all materials behave elastically up to the point of fracture as brittle substances do. Many materials flow plastically before they will fracture. However, these materials are elastic before they reach a plastic state. In the elastic region, the analytical method for these materials is identical with that for brittle substances. Initiation of flow, however, is considered to be controlled by a different condition than fracture in brittle materials. The amount of elastic deformation before plastic flow starts is thought to be a function of the elastic distortional strain energy per unit volume of deformed material. Flow occurs when the distortional strain energy reaches a value characteristic of the material (Jaeger, 1956, p. 93). The formula for this criterion in the two dimensional plane strain case is (Timoshenko and Goodier, 1951, p. 149):

$$E_d = \text{const} = \frac{1}{12G}\left\{\left[\sigma_x - \sigma_y\right]^2 + \left[\sigma_y - \nu(\sigma_x + \sigma_y)\right]^2 + \left[\nu(\sigma_x + \sigma_y) - \sigma_x\right]^2 + 6\tau_{xy}^2\right\} \quad (40)$$

This criterion, credited to von Mises, differs in two respects from the Mohr criterion. The initiation of plastic flow is independent of confining stress and occurs regardless of whether the stresses are tensile or compressive.

In the numerical examples, values of distortional strain

energy density were calculated using the values of stress dictated by the Mohr fracture criterion. The values obtained in this manner are not related to any characteristic values for rock materials. However, the distributions of distortional strain energy density do show the regions susceptible to flow in materials which favor this mode of failure. These regions are of interest because they are not always centered at points of fracture as determined by the Mohr criterion.

Numerical Examples

Introduction

Table 1 summarizes the examples used and the results obtained from numerical calculations. The examples are separated into two categories according to the nature of the displacement specified along the lower boundary of the elastic layer (see fig. 3). In the first category, the lower boundary of an elastic layer undergoes a very gradual change in vertical displacement (proportional to the cos $(\pi x/L)$), and no horizontal displacement. In the second category, the lower boundary of an elastic layer undergoes no horizontal movement, but is subjected to relatively rapid changes in vertical displacement in short transition zones connecting uniformly elevated and depressed blocks.

The elastic layers in the first example of each category have the same thickness, length (defined as the distance between points of zero vertical displacement along the lower boundary), elastic properties, and fracture properties. The additional examples in each category are for layers which differ in one or more

		Category I				
Boundary Conditions	At Y = 0	$\sigma_y = 0$			$\tau_{xy} = 0$	
	At Y = H	$v = -B\cos\frac{\pi x}{L}$			$u = 0$	
Examples		a	b	c	d	e
1. Dimensions of Layer						
H--km		5	5	5	5	5
L--km		25	25	25	15.7	15.7
2. Elastic Properties						
		.250	.167	.333	.250	.143
G--10^{00} dynes/cm^2.		2.0	3.0	2.0	2.0	2.0
3. Fracture Properties						
-deg.		35	30	35	35	35
-kg/cm^2		250	1730	250	250	250
4. Fracture Point Location						
X		0	0	0	0	0
Y		0	0	0	0	0
5. Magnitude and Location of Maximum Stresses						
x max. --kg/cm^2.		-1261	$\pm$2000	-1266	-1275	-1263
X		0	0	0	0	0
Y		H	0	H	H	H
y max. --kg/cm.^{2}		-1282	-1500	-1282	-1324	-1326
X		0	0	0	0	0
Y		H	H	H	H	H
xy max. --kg/cm.^{2}		74	577	72	103	108
X		L/2	L/2	L/2	L/2	L/2
Y		H	H	H	H	H
6. Magnitude and Location of Maximum Displacements at the Upper Boundary						
Max. v--m		7.8	43.6	7.0	3.9	4.4
X		0	0	0	0	0
Max. u--m		3.8	21.6	3.4	2.4	2.8
X		L/2	L/2	L/2	L/2	L/2
7. Magnitude and Location of Maximum Displacements at the Lower Boundary.						
Max. v--m		8.2	45.5	7.6	4.5	4.9
X		0	0	0	0	0
Max. u--m		0	0	0	0	0
X						

Category II			Example A	
$\sigma_y = 0$		$\tau_{xy} = 0$	$\sigma_y = 0$	$\tau_{xy} = 0$
$v = \frac{4B}{\pi} \sum_1^{\infty} \frac{(-1)^{n+1}}{(2n-1)} \cos(2n-1)\frac{\pi x}{L}$		$u = 0$	$\sigma_y = -A \sin \frac{\pi x}{L}$	$\tau_{xy} = 0$
a	b			
5	5			5
25	25			15.7
.250	.250			.250
2.0	3.0			2.0
35	30			35
250	2160			250
.375L	.530L			L/2
0	H			0
-1578	-2380			-1508
.45L	.45L			L/2
H	H			H
-2229	-4696			-1292
.45L	.45L			L/2
H	H			H
489	1690			63
L/2	L/2			0
H	H			H/2
3.7	8.4			5.7
0	0			L/2
3.0	6.8			2.5
L/2	L/2			0
3.7	8.4			5.8
-	-			L/2
0	0			2.4
				0

Table 1. Summary of the numerical examples.

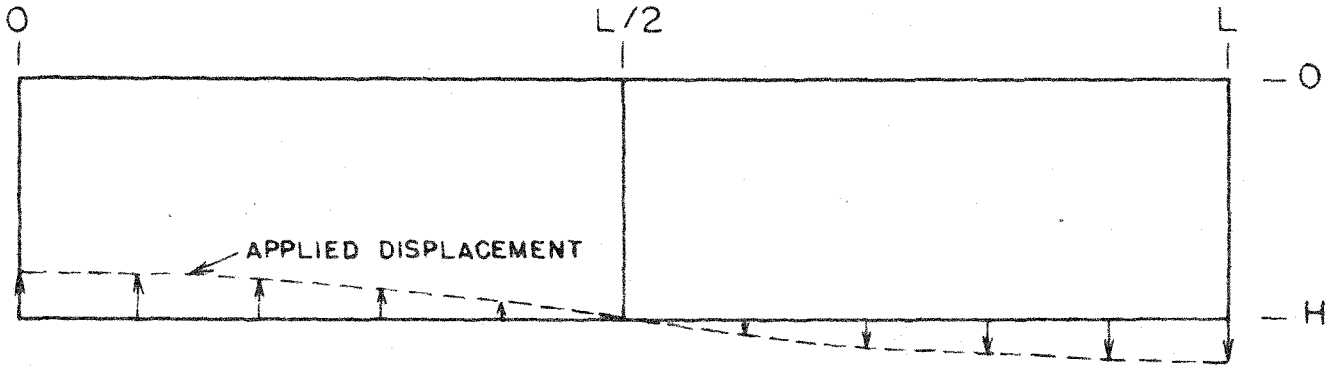

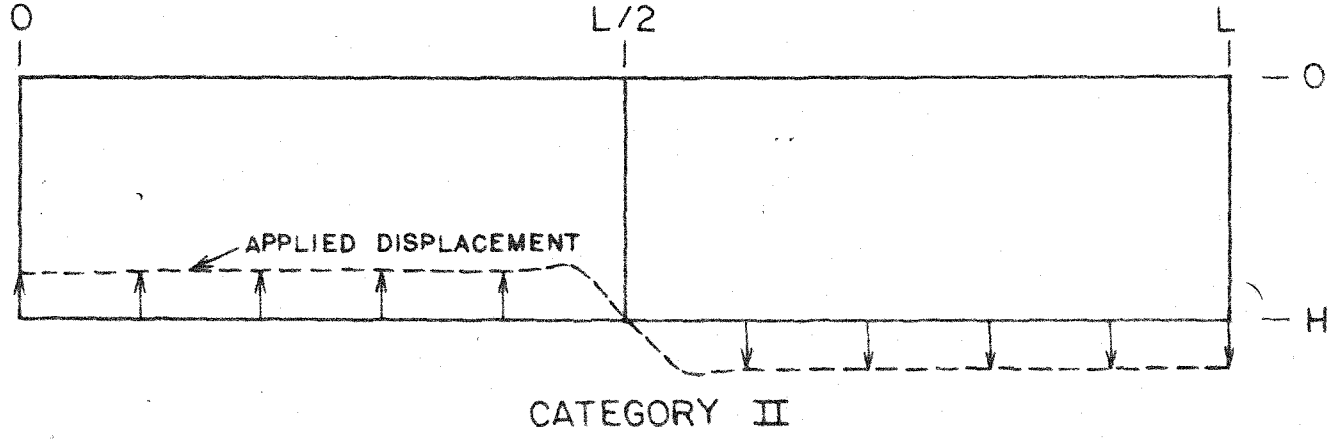

Figure 3. Classification of the numerical examples.

ways from the layer in the first example. The boundary conditions, dimensions of the layer, elastic constants, and Mohr fracture criterion parameters for each example are listed in Table 1.

Boundary Conditions

In all of the numerical examples, the boundary conditions at the upper surface of the elastic layer are $\sigma_y = 0$ and $\tau_{xy} = 0$. These conditions specify a free upper surface which corresponds to the surface of the earth. In all of the numerical examples, the lower boundary of the elastic layer undergoes no horizontal displacement, but is subjected to different distributions of vertical displacement. These boundary conditions approximate the conditions along the lower surface of an elastic sedimentary layer which is deformed by vertical movement of rigid bedrock beneath it. The contact between rigid bedrock and elastic sedimentary rock is "welded" so that horizontal movement along the contact is prevented.

Properties of the Rock Layers

Average values of the rock properties are used in the first example of each category. The density, 2.5 gms/cm^3, and Poisson's ratio, .250, are based on the values listed in the Handbook of Physical Constants (Birch, et al., 1942, pp. 8-37, 76). The value of rigidity adopted, 2.0×10^{11} dynes/cm^2, is Gutenberg's estimate of rigidity for Tertiary sandstone at a depth of 2 kilometers (Gutenberg, 1951, p. 367). The angle of internal friction, 35 degrees, is based on experimental evidence cited by Hubbert (1951). The cohesive strength, 250 kg/cm^2, was calculated from crushing strength data on sedimentary rocks (Birch, et al., 1942,

p. 116; Marin, 1952, p. 381; Mills, et al., 1955, p. 310) and the adopted angle of internal friction of 35 degrees.

The other examples have rock properties which differ from these average values. These examples are of interest because they illustrate the change in results with change in one or more properties of the layer.

Presentation of Results

The results of some of the numerical calculations are presented diagrammatically in figs. 4 through 16. These figures are drawn for a short portion of a layer between the limits $X = 0$ and $X = L$. However, the symmetry of the problem makes it possible to visualize the results for longer layers by rotating the drawings about vertical axes in the plane of the figure.

The displacements shown in these figures are only those resulting from the application of vertical displacements on the lower boundary of the layer. They do not include the displacements arising from the initial state of hydrostatic stress because these displacements can not be measured in scale model experiments. The stresses, on the other hand, are referred to a state of no stress, because total stress, including the initial hydrostatic stress, is important in determining the point of fracture.

Check of the Calculations

One primary requirement for a valid solution of these examples is that the layer be in equilibrium in the stressed condition. The equilibrium requirements for a stressed layer which is L/2 long and H thick are:

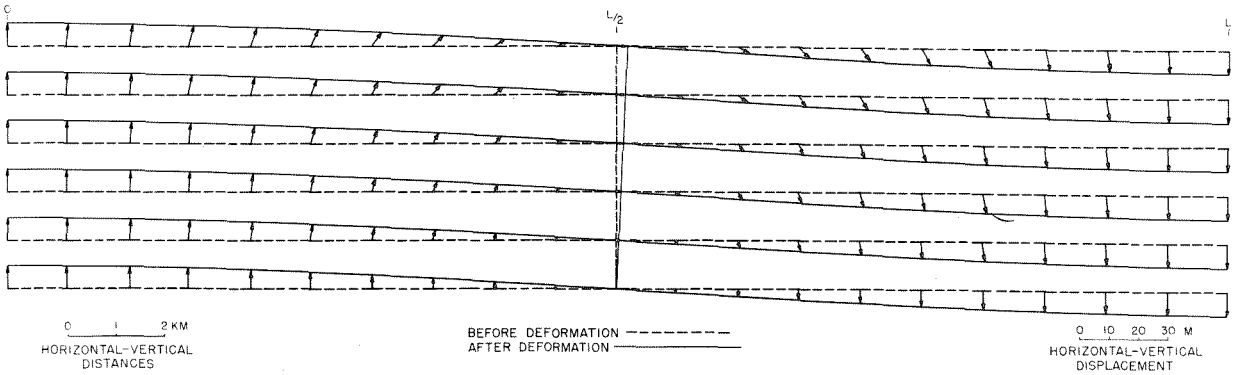

Figure 4. Example Ia - Displacement field.

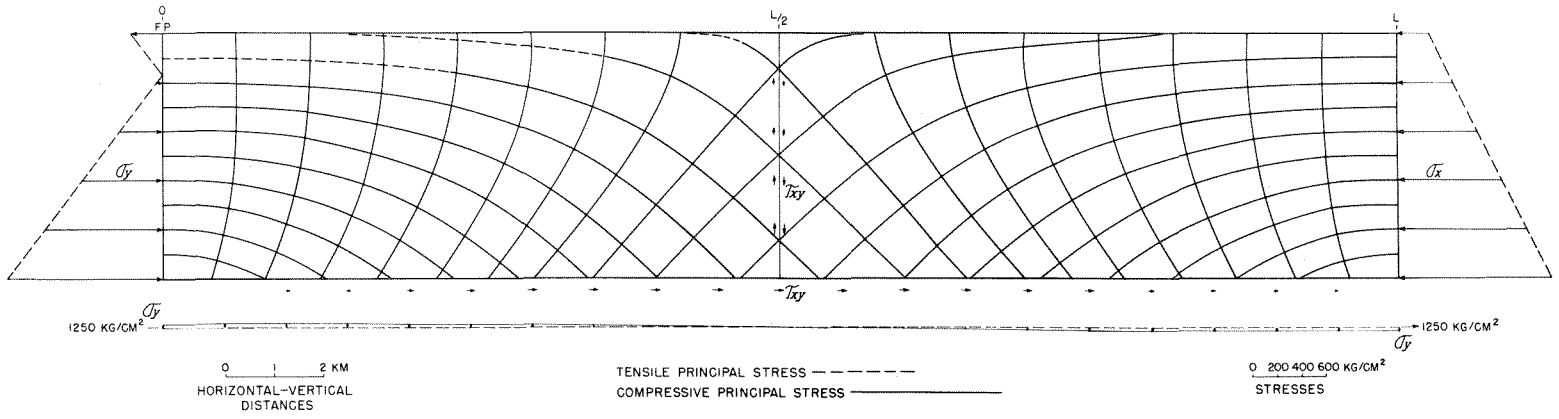

Figure 5. Example Ia - Stress distribution.

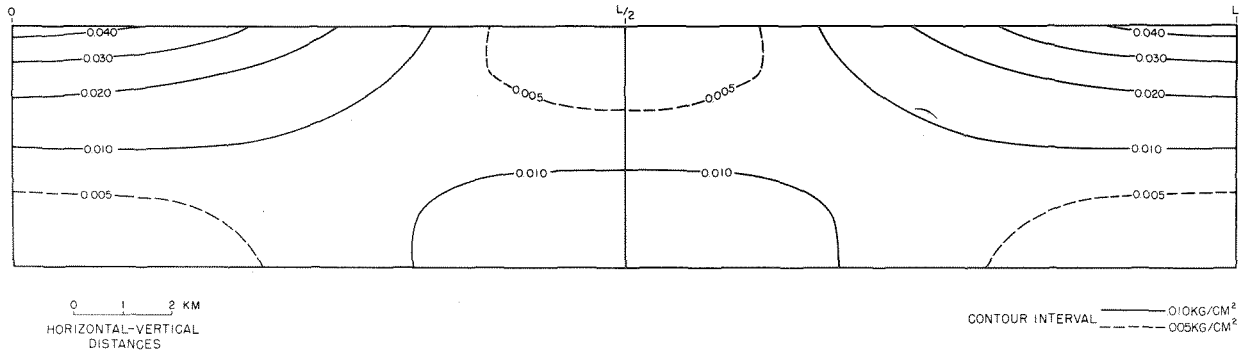

Figure 6. Example Ia - Distortional strain energy density.

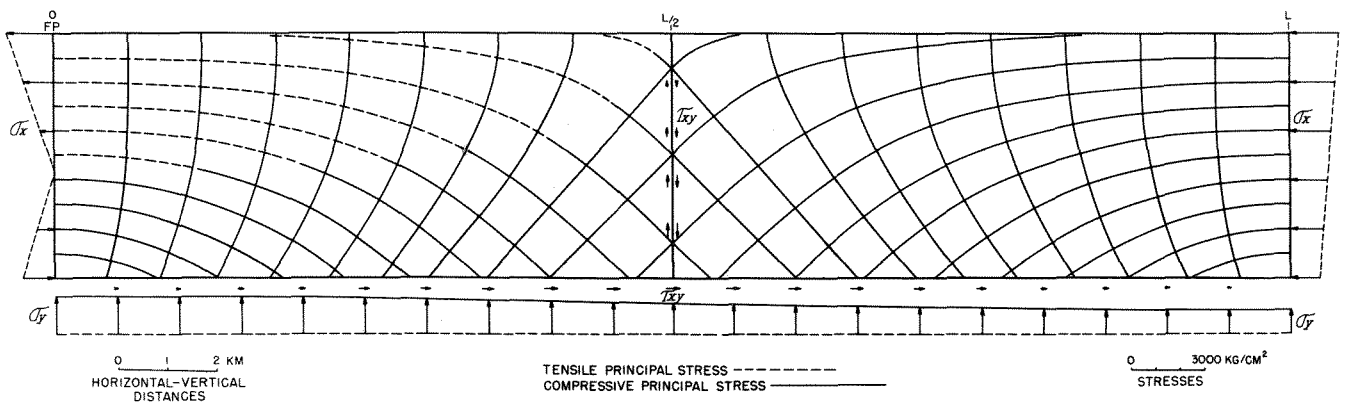

Figure 7. Example Ib - Stress distribution.

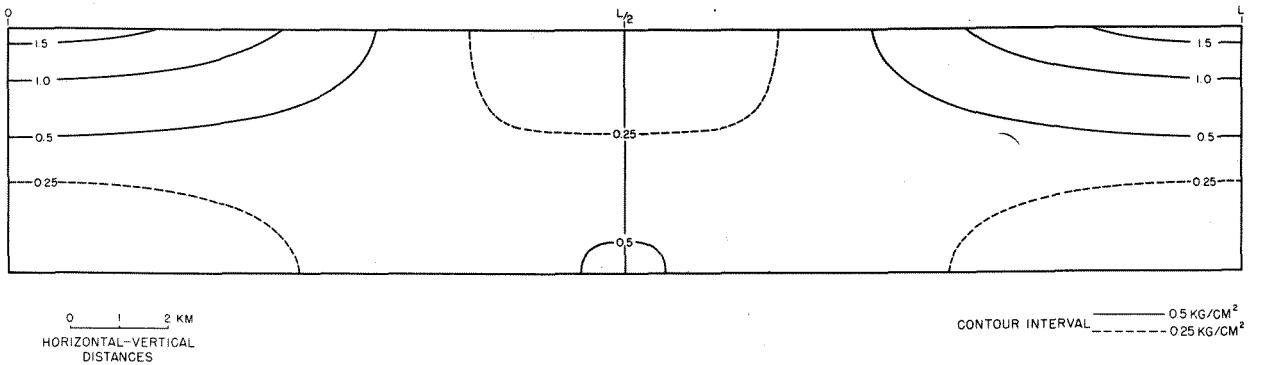

Figure 8. Example Ib - Distortional strain energy density.

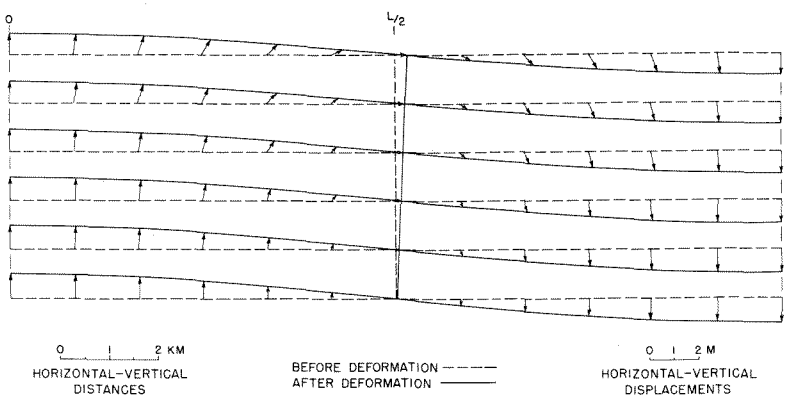

Figure 9. Example Id - Displacement field.

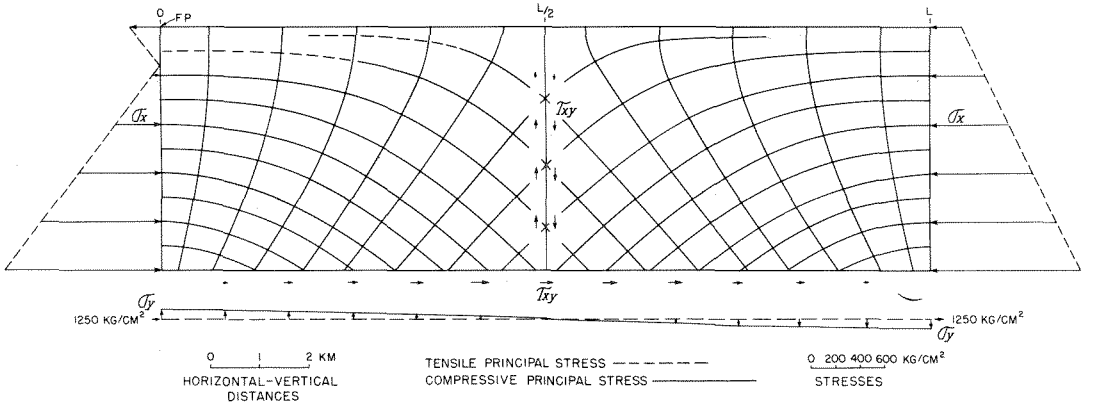

Figure 10. Example Id - Stress distribution.

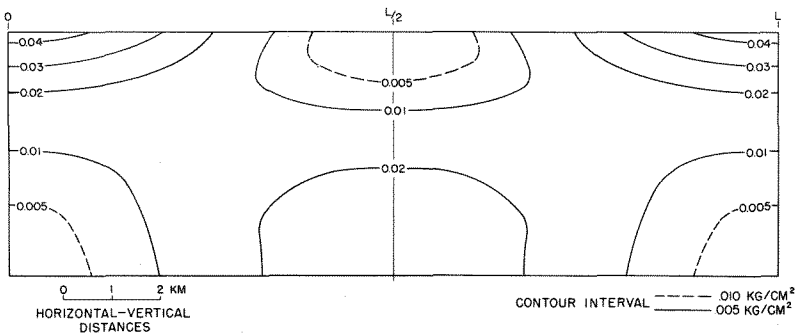

Figure 11. Example Id - Distortional strain energy density.

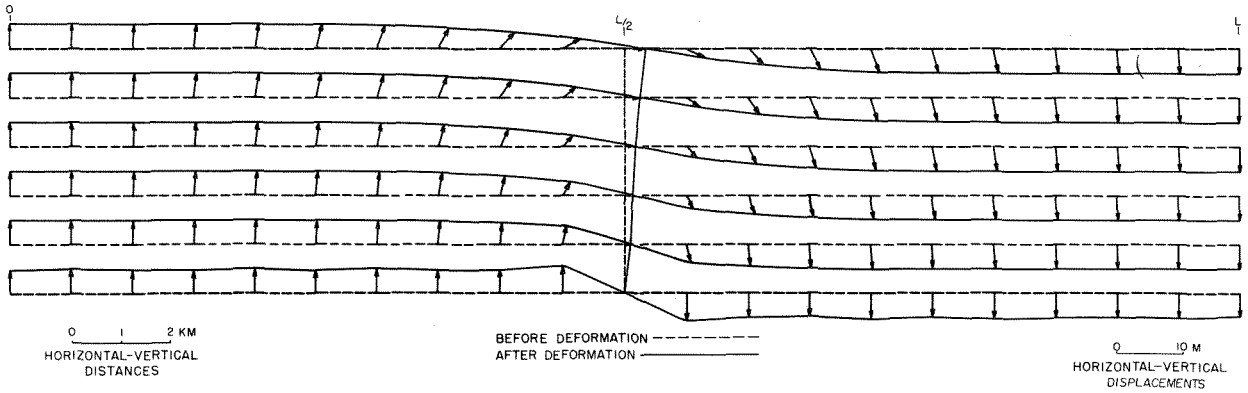

Figure 12. Example IIa - Displacement field.

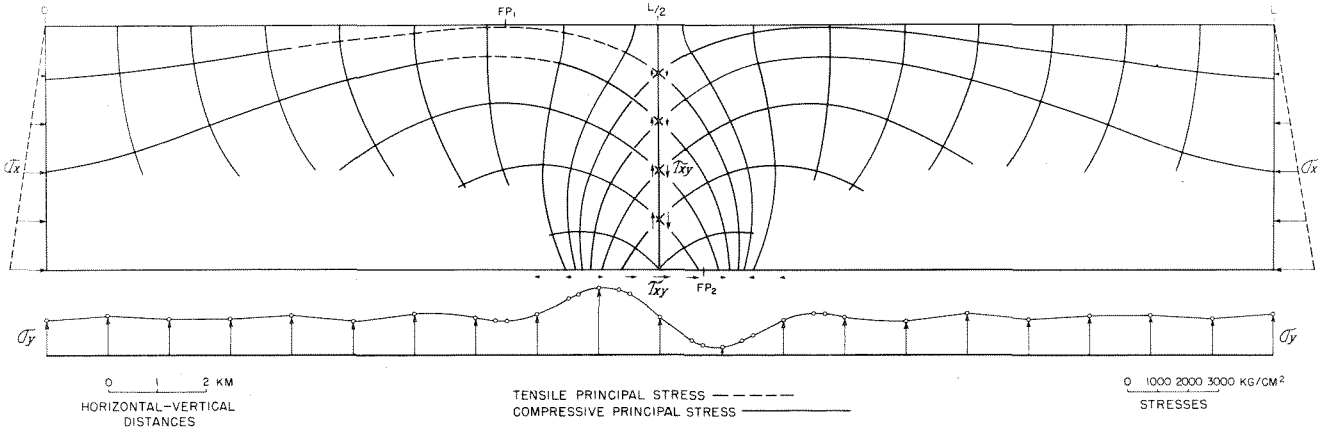

Figure 13. Example IIa - Stress distribution.

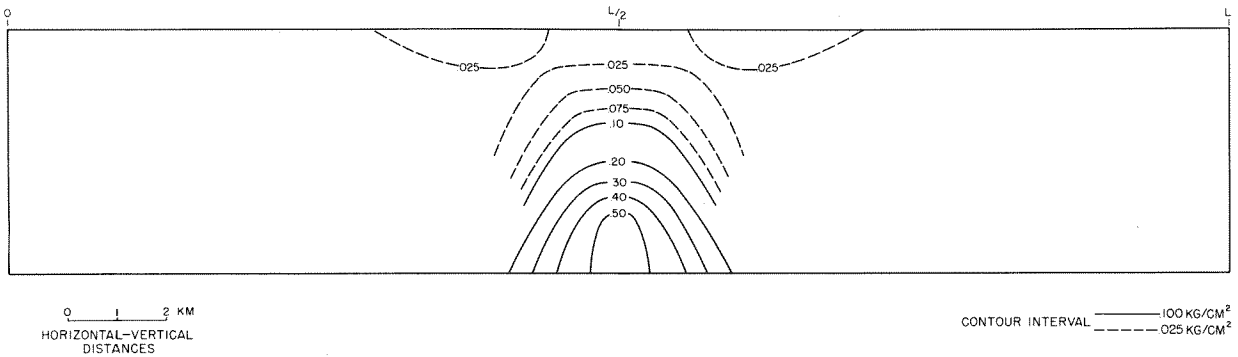

Figure 14. Example IIa - Distortional strain energy density.

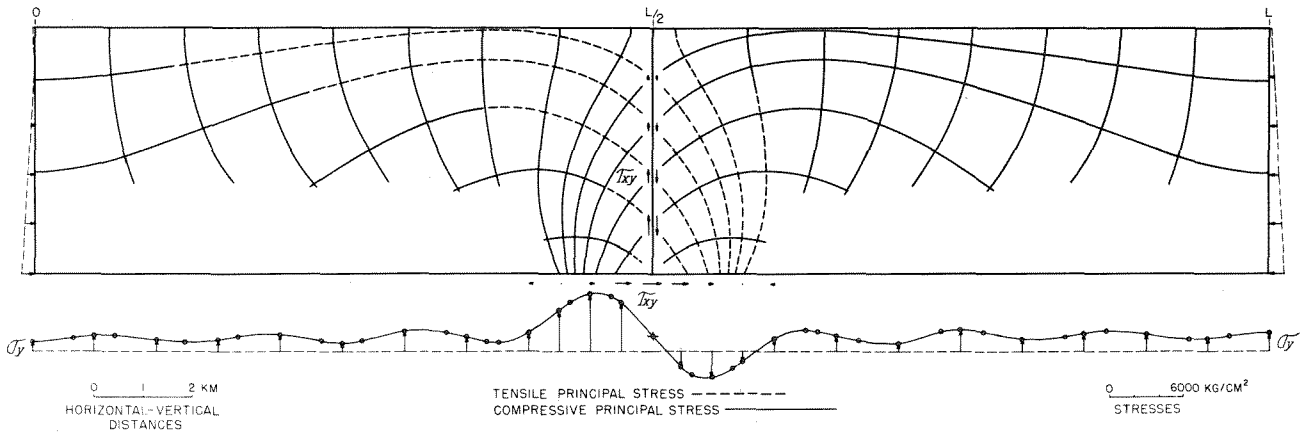

Figure 15. Example IIb - Stress distribution.

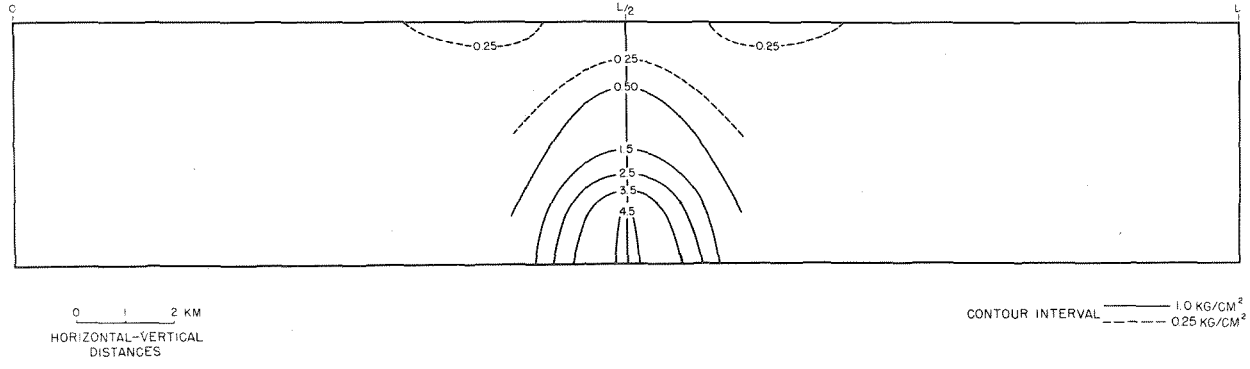

Figure 16. Example IIb - Distortional strain energy density.

X component of total force = 0 $$\int_0^H \sigma_x \, dy = \int_0^{L/2} \tau_{xy} \, dx \,, \qquad (41)$$

Y component of total force = 0 $$\int_0^{L/2} \sigma_y \, dx = \int_0^H \tau_{xy} \, dy \,, \qquad (42)$$

Total torque = 0 $$\left(\int_0^H \sigma_x \, dy \right) \cdot \bar{y} + \left(\int_0^{L/2} \sigma_y \, dx \right) \cdot \bar{x} = \left(\int_0^H \tau_{xy} \, dy \right) \cdot L/2 \,, \qquad (43)$$

where $\bar{x}$ and $\bar{y}$ = centers of force.

These equations were used to check the calculations. The integrations and determinations of center of force were made with a planimeter.

Discussion of the Numerical Examples

Category I Examples

Point of Initial Fracture and Critical Displacement. All examples fracture initially at the point of maximum horizontal tensile stress along the upper boundary (point FP on figs. 5, 7, and 10). The type of fracture is a vertical tensile crack. The critical displacement at which this point fractures is a function of the dimensions, the elastic constants, and the fracture properties of the layer. Fig. 17 shows the change in critical displacement with change in the elastic constants and dimensions of the layer while the fracture properties remain constant (τ_o = 250 kg/cm^2, ϕ = 35 degrees).

Displacement Field. The following are the important features of the displacement fields (see figs. 4 and 9):

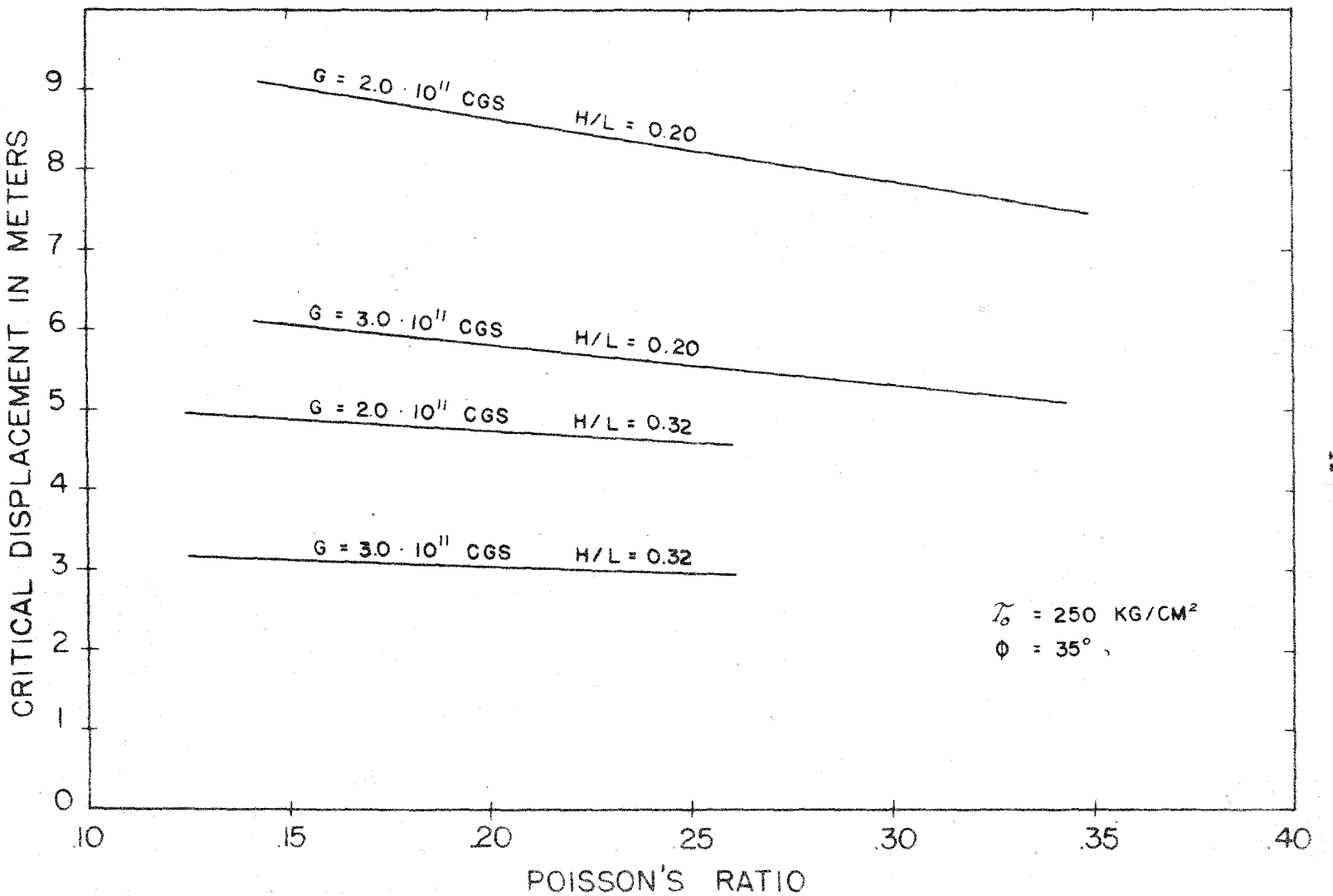

Figure 17. Category I - Variation of critical displacement with dimensions and elastic properties of the layer.

1. The shape of the elastic layer affects the appearance of the displacement field (compare figs. 4 and 9).

2. The relative magnitudes and the orientations of the displacement field vectors are only slightly influenced by Poisson's ratio of the layer material. For the same applied displacement, examples Ia ($\nu = .250$), Ib ($\nu = .167$), and Ic ($\nu = .333$) have nearly identical displacement fields (see fig. 4).

3. The horizontal displacement increases linearly from zero at the lower boundary to a maximum at the upper boundary. The variation in the maximum horizontal displacement (at $X = L/2$) at the boundaries with changes in the value of Poisson's ratio and the dimensions of the layer is shown in figs. 18 and 19.

4. The vertical displacements decrease in magnitude from the lower to the upper boundary. The variation in the maximum vertical displacement (at $X = 0$) at the boundaries with changes in the value of Poisson's ratio and the dimensions of the layer is shown in figs. 18 and 19.

Stress Distribution. The following are the important features of the stress distributions (see figs. 5, 7, and 10):

1. The shape of the elastic layer affects the appearance of the stress distribution (compare figs. 5 and 10).

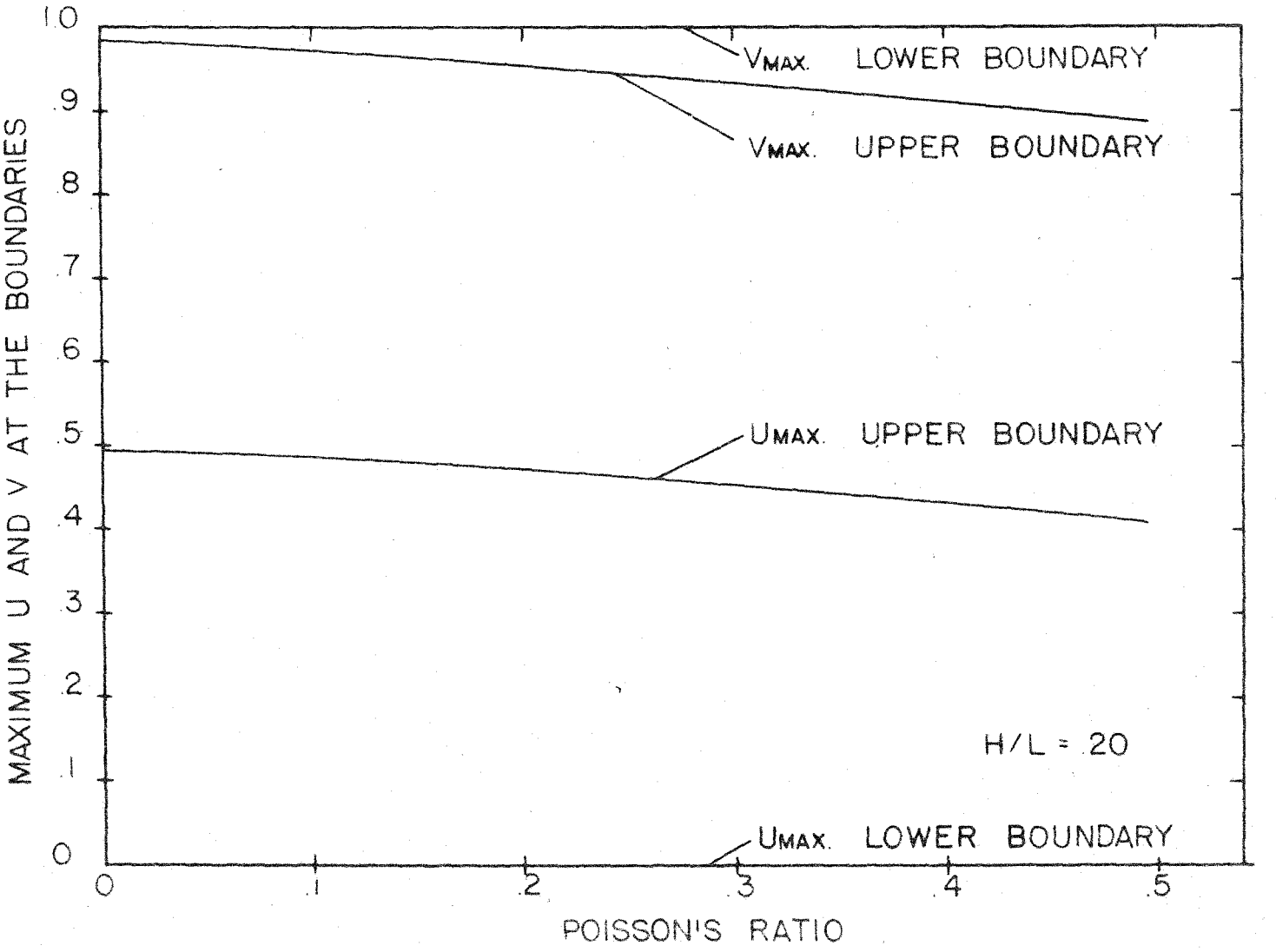

Figure 18. Category I - Horizontal and vertical displacements at the boundaries as a function of Poisson's ratio.

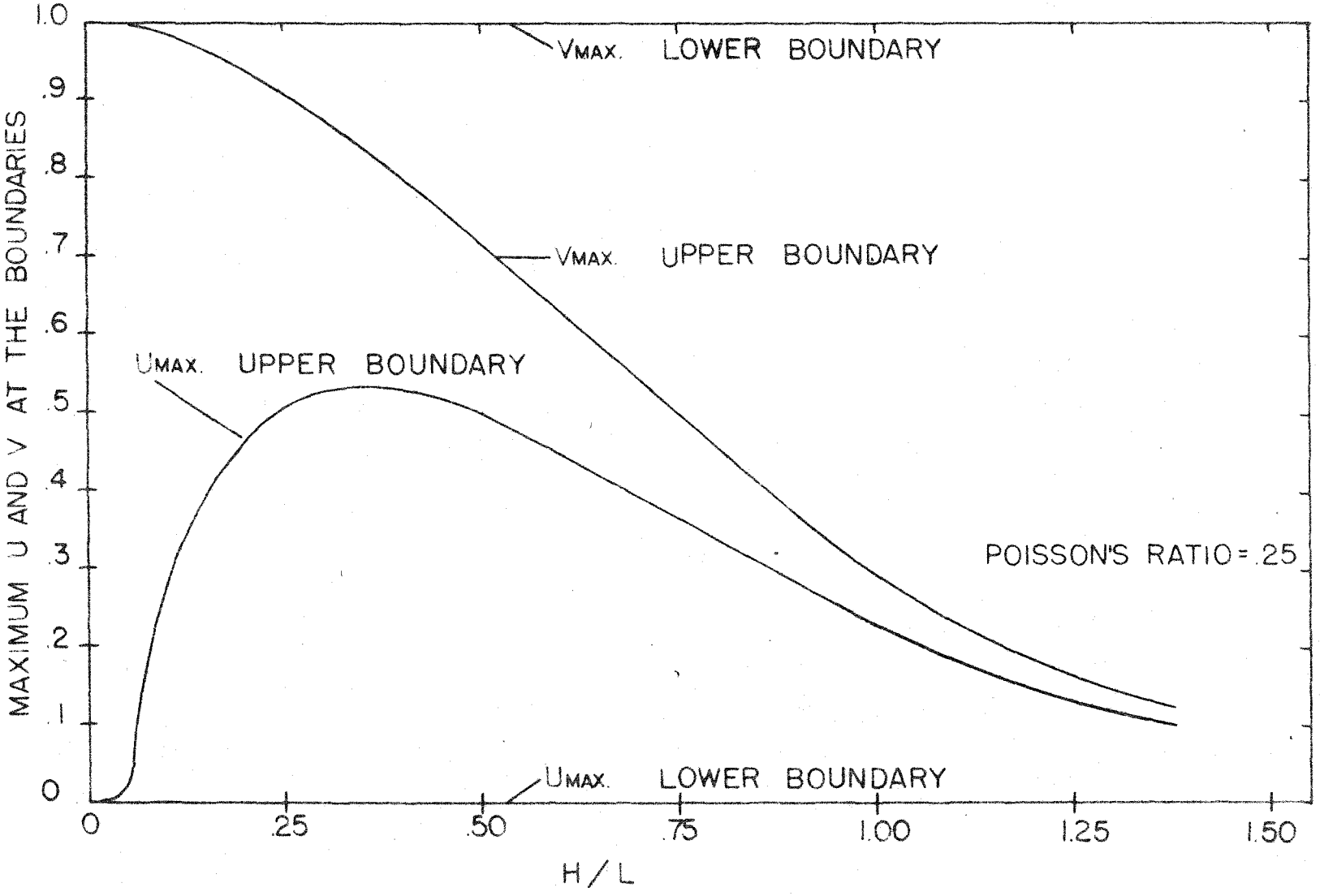

Figure 19. Category I - Horizontal and vertical displacements at the boundaries as a function of the dimensions of the layer.

2. The orientations of the principal stresses are only slightly influenced by Poisson's ratio of the layer material. Principal stresses in examples Ia, Ib, and Ic (see figs. 5 and 7) have nearly identical orientations throughout the layer even though the value of Poisson's ratio ranges from .167 to .333 in these examples.
3. The only area of tensile principal stresses is along and near the upper surface, and centered directly over the uplifted segment of the layer.
4. The neutral axis of stress (excluding the initial hydrostatic stress) is at a distance of 1/100 L or less from the bottom of the layer.
5. The distribution of vertical stress is the same as the distribution of vertical displacement.

The last feature indicates that similar results could have been obtained using the analytical method, described by Hafner (1951), in which stresses rather than displacements are specified along the lower boundary. For example, the orientations of the stress trajectories in fig. 5 are nearly identical with those in a diagram (Supplementary Stress System C) published by Hafner. The only difference between Hafner's and the writer's stress diagrams is the magnitude of stress along the lower boundary of the layer.

In fig. 5, the magnitude of this stress is just that amount necessary to place point FP in a fracture condition. The magnitude of the corresponding stress in Hafner's example is many times larger, so that large segments of the deformed block are in a fracture condition.

Distortional Strain Energy Density. There are two regions which are equally susceptible to yielding by plastic flow according to the distortional strain energy density distributions in figs. 6, 8, and 11. One region is centered in the upper half of the uplifted segment of the layer, the other is centered in the upper half of the downdropped segment of the layer. Fracture, according to the Mohr criterion, occurs at the surface in the center of the uplifted segment where there are high tensile stresses in the horizontal direction. Fracture does not occur at the corresponding point of the downdropped segment because the stresses at this point are compressive. Fracture is influenced by the type of the stress; yielding by flow is not, according to von Mises criterion.

Category II Examples

Point of Initial Fracture and Critical Displacement. The point of initial fracture is dependent on both the elastic and fracture properties of the layer. Two points of fracture are possible: one at $X = .375L$, $Y = 0$ (FP_1 on figs. 13 and 15); the other at $X = .530\ L$, $Y = H$ (FP_2 on figs. 13 and 15). The type of fracture at FP_1 is a vertical tensile crack. The type of fracture at FP_2 is a shear fracture. Fracture will occur at one or the other of these points, or at both simultaneously, depending on the combinations of elastic and fracture properties for the rock layer. In example IIb, which

is a very strong layer (perhaps too strong to be considered rock), fracture occurs first at FP_2. In example IIa, which has average elastic and fracture properties, fracture occurs first at FP_1. However, fig. 20 illustrates how a slight shift in the fracture properties of the layer in example IIa (assuming constant applied vertical displacement) can cause simultaneous fracture at FP_1 or FP_2, or fracture at FP_2 alone. The critical displacement necessary to start fracture at either FP_1 or FP_2 decreases with an increase in rigidity and a decrease in cohesion.

Displacement Field. The following are the important features of the displacement fields (see fig. 12):

1. The transition in vertical displacement becomes progressively less abrupt from the lower to the upper boundary of the layer. The change in the maximum vertical displacement (at $X = 0$) at the boundaries with a change in the dimensions of the layer is shown in fig. 21.
2. The horizontal displacement increases nearly linearly from zero on the lower boundary to a maximum at the upper boundary. The change in the maximum horizontal displacement (at $X = L/2$) at the boundaries with a change in the dimensions of the layer is shown in fig. 21.

A qualitative idea of the change in the displacement field with changes in Poisson's ratio can be obtained from an examination of examples in Category I. The solution of problems in Category II is found by superposing several solutions of the Category I

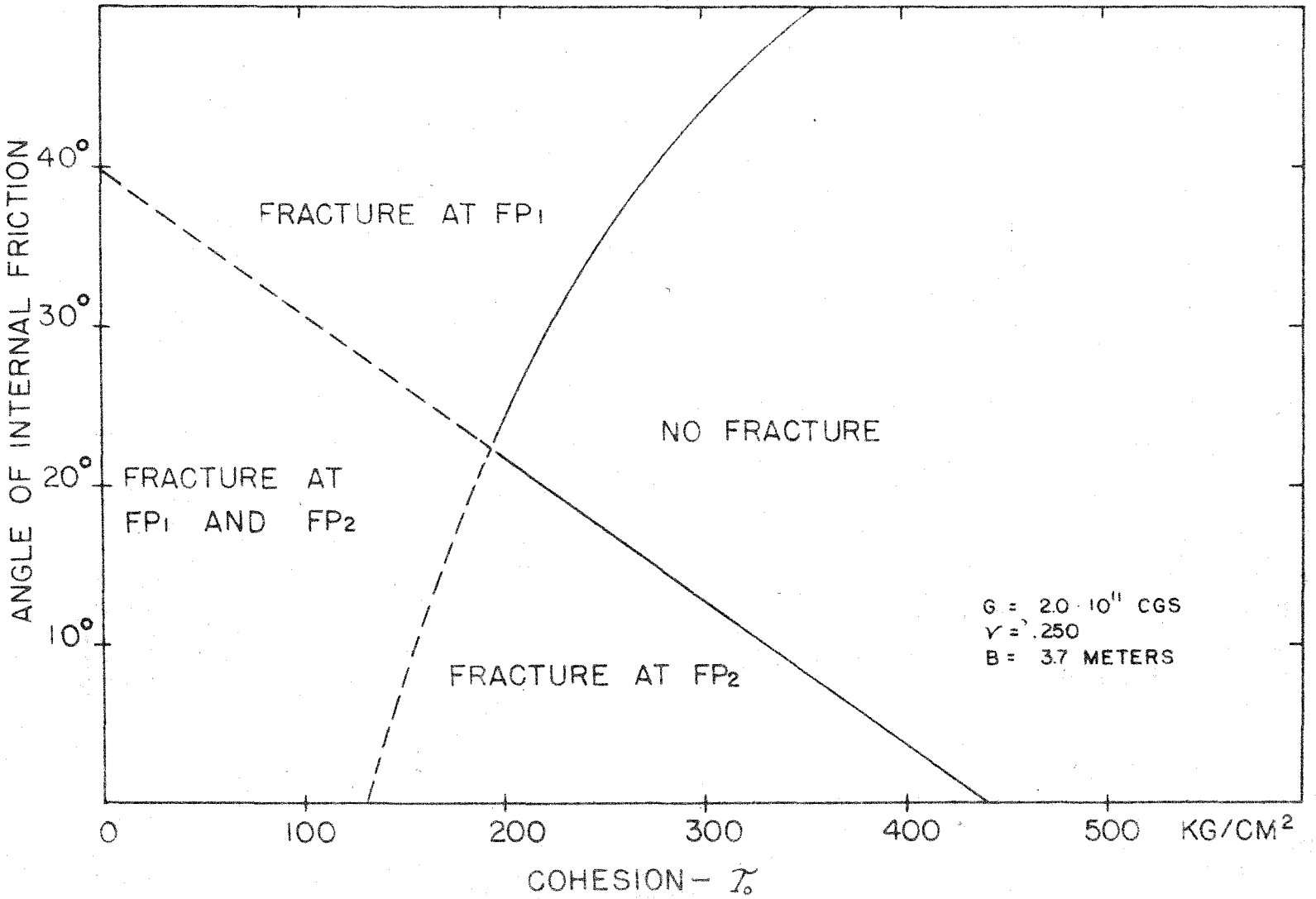

Figure 20. Example IIa - Location of the fracture point as a function of the fracture characteristics of the material of the layer.

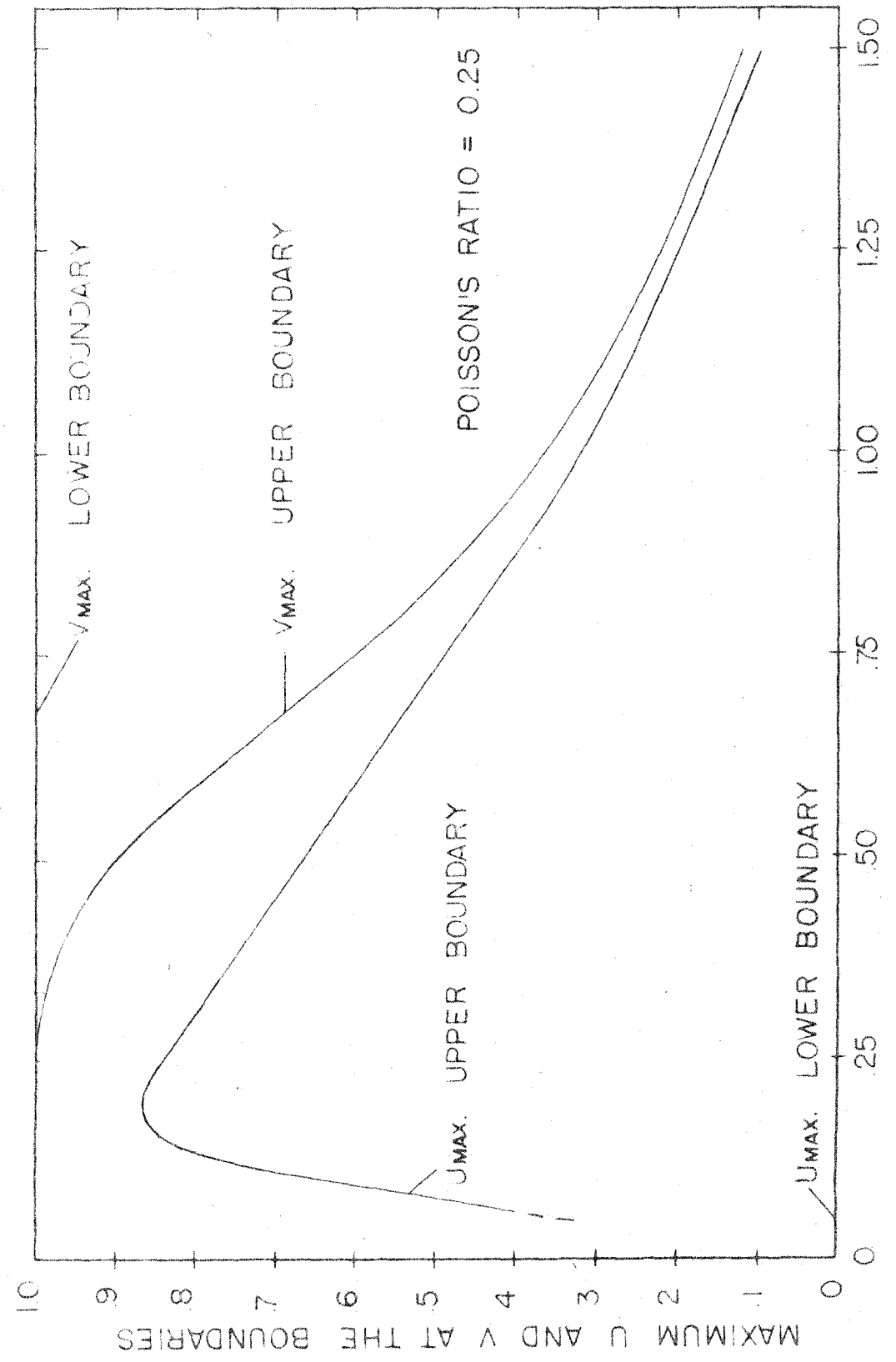

Figure 21. Category II - Horizontal and vertical displacements at the boundaries as a function of the dimensions of the layer.

type. The relative magnitude and orientations of displacement vectors in the latter examples are only slightly affected by changes in Poisson's ratio. Therefore, the displacement fields in Category II are not likely to change significantly with changes in Poisson's ratio.

Stress Distribution. The following are the important features of the stress distributions (see figs. 13 and 15):

1. The area of tensile principal stresses is along the upper surface near the edge of the uplifted segment. The stronger the layer is, the greater the extent of the tensional areas. For extremely strong layers, the area of tensile stresses extends to the base of the layer (fig. 15).
2. Most of the vertical stress along the bottom of the layer is concentrated towards the ends of adjoining uplifted and downdropped blocks. There are very minor oscillations of vertical stress along the entire lower boundary which cause irregular changes in the orientation of the stress trajectories near the base of the layer. For this reason, stress trajectories have been omitted near the lower boundary of the layer in figs. 13 and 15.
3. The stresses in the central regions of each block are nearly zero (if initial hydrostatic stresses (ρgy) are disregarded).

The last two features of the stress distributions are the

reasons for no deformation of layers which have been uniformly elevated or depressed. All deformation is restricted to the stressed regions that are located above the segments of the lower boundary which undergo rapid changes in vertical displacement. In addition, the lack of stress in the central regions of the layers indicates that a uniform displacement superposed on any of the above examples will not change the stress distribution. Therefore, the results shown in figs. 5, 7, 10, 13, and 15 are also solutions for examples in which all vertical displacements applied along the lower boundary of an elastic layer are in one direction.

Distortional Strain Energy Density. There are two separate regions of relatively high distortional strain energy density along the upper boundary of the layer (see figs. 14 and 16). The maximum Ed in these regions is equal to the maximum values found in the Category I examples. One of these regions is located in an area of large horizontal tensile stresses. The other region is located in an area of large horizontal compressive stresses. Fracture, according to the Mohr criterion, may occur in the first region mentioned above, but not in the second.

The highest concentration of distortional strain energy is at the bottom of the layer directly above the zone of transition in vertical displacement. Despite the much higher concentration of Ed in this region, fracture at FP_2 is not favored over fracture at FP_1, according to the Mohr criterion.

Scope of the Numerical Examples

The only factor which has a major influence on the orientations of the displacement vectors and the stress trajectories is

the shape of the layer. As a result, the numerical solutions given here are applicable to any homogeneous elastic layer providing (1) its shape is the same as the shape of the layer in the example, and (2) an appropriate scaling factor is used to determine the magnitudes of stress in the stress diagram. The scaling factor is based on the rigidity of the layer and the maximum applied displacement. The latter must be less than the amount of displacement necessary to initiate fracture.

Elastic properties of the layer do not have to be known to obtain the information necessary for a comparison of elastic analyses and scale model experiments. Displacements and fractures (see section entitled "Prediction of Fractures"), the only items easily observed in a model experiment, are independent of the elastic constants in the elastic analyses. Therefore, geometrical similarity of layer shapes is the only requirement for a comparison between a two dimensional elastic analysis and a two dimensional scale model.

Frictionless Lower Boundary

Introduction

A "welded" contact, which is specified along the lower boundary of the previous numerical examples, is one extreme of many possible contact conditions. The opposite extreme is a "frictionless" contact. An analytical investigation of the frictionless lower boundary case was made to determine the effect of contact conditions on deformation resulting from simple distributions of vertical displacement.

The analysis of the frictionless contact case can best be made with analytical procedure described by Hafner (1951). A frictionless condition at the lower boundary means that the shearing stress is zero along that boundary. The magnitude of applied horizontal displacement which gives zero shearing stress along the lower boundary is difficult to estimate. The easiest approach is to specify stresses as Hafner did in his work. As previously mentioned, Hafner's method and the writer's method give equivalent results when applied to simple situations. The choice of one or the other of these methods is dictated by what is known at the boundaries of the layer.

General Theory

The assumptions made and restrictions imposed on Hafner's analytical procedure are identical with those in the method previously discussed. Also, the basic requirements for a valid solution are the same. That is, the solution must satisfy equilibrium (equations 1 through 2), compatibility (equation 3), and specified boundary conditions. If the solution gives stresses and displacements which satisfy all of these conditions, then it can be shown that the solution is unique (Timoshenko and Goodier, 1951, p. 236; Muskhelishvili, 1953, pp. 66-71).

Derivation of the Analytical Method

The equilibrium equations are satisfied by the following expressions for stress:

$$\sigma_x = \frac{\partial^2 \phi}{\partial y^2}, \tag{44}$$

$$\sigma_y = \frac{\partial^2 \phi}{\partial x^2} \quad , \tag{45}$$

$$\tau_{xy} = -\frac{\partial^2 \phi}{\partial x \partial y} \quad , \tag{46}$$

where ϕ is a function of x and y. Substitution of these expressions into equation (3) shows that the compatibility requirement will be met if:

$$\nabla^4 \phi = 0 \quad . \tag{47}$$

(The function satisfying this single biharmonic equation is called the Airy stress function.)

The solution of problems in this procedure reduces to the solution of a single biharmonic equation which will give stresses satisfying the prescribed boundary conditions. The problem of interest here is the deformation of an elastic layer of thickness "H" under the following boundary conditions:

At Y = 0, $\sigma_y = 0$, $\tau_{xy} = 0$ (Stresses zero);

At Y = H, $\sigma_y = -A \sin \alpha x$, $\tau_{xy} = 0$.

The biharmonic equation and the boundary conditions are satisfied by:

$$\phi = \sin \alpha x \left[C_1' \cosh \alpha y + C_2' \sinh \alpha y + C_3' y \cosh \alpha y + C_4' y \sinh \alpha y \right] \quad . \tag{48}$$

(This solution is equivalent to equation 20.) Note that in this derivation, we do not have the difficulty which existed in the other derivation. There are an equal number of constants and boundary conditions. The constants in equation (48) are equal to:

$$C_1' = 0 \,,$$

$$C_2' = -\frac{C_3'}{\alpha} = \frac{C_4' K_1'}{\alpha} = \frac{C_4'}{\alpha}\left(\frac{\sinh\alpha H + \alpha H \cosh\alpha H}{\alpha H \sinh\alpha H}\right), \tag{49}$$

$$C_3' = -C_4 K_1' = -C_4'\left(\frac{\sinh\alpha H + \alpha H \cosh\alpha H}{\alpha H \sinh\alpha H}\right), \tag{50}$$

$$C_4' = \frac{A}{\alpha K_2'} = \frac{A}{\alpha[\sinh\alpha H(H\alpha + K_1') - K_1' \alpha H \cosh\alpha H]}. \tag{51}$$

The general equations for σ_y, σ_x, τ_{xy}, v, and u are:

$$\sigma_y = -\frac{A \sin\alpha x}{K_2'}\left\{\sinh\alpha y(y\alpha + K_1') - y\alpha K_1' \cosh\alpha y\right\}, \tag{52}$$

$$\sigma_x = +\frac{A \sin\alpha x}{K_2'}\left\{\sinh\alpha y(y\alpha - K_1') + \cosh\alpha y(2 - \alpha y K_1')\right\}, \tag{53}$$

$$\tau_{xy} = -\frac{A \cos\alpha x}{K_2'}\left\{\sinh\alpha y(1 - K_1'\alpha y) + \alpha y \cosh\alpha y\right\}, \tag{54}$$

$$v = \frac{A \sin\alpha x}{2\alpha G K_2'}\left\{(1-2\nu)\sinh\alpha y + K_1 \alpha y \sinh\alpha y - 2K_1'(1-\nu)\cosh\alpha y - \alpha y \cosh\alpha y\right\} + \text{const.}, \tag{55}$$

$$u = -\frac{A \cos\alpha x}{2\alpha G K_2'}\left\{-K_1'(1-2\nu)\sinh\alpha y + \alpha y \sinh\alpha y + 2(1-\nu)\cosh\alpha y - \alpha y K_1' \cosh\alpha y\right\} + \text{const.}. \tag{56}$$

Note that the elastic constants appear in the displacement equations, but not in the stress equations.

Numerical Example

Table 1 summarizes the results obtained from one numerical example (A). In example A, a gradual change in vertical stress (proportional to sin x/L) is applied to the lower frictionless boundary of an elastic layer. The elastic constants and fracture properties for the layer are: $\nu = .250$, $G = 2.0 \times 10^{11}$ dynes/cm^2, $\tau_o = 250$ kg/cm^2,

and $\phi = 35$ degrees. The results of the calculations are presented diagrammatically in figs. 22 through 24. Fracture point and critical displacement were determined by the Mohr fracture criterion (equations 39 and 40). The calculations were checked by equations 41 through 43 in the same manner as the previous numerical examples.

Discussion of the Results

The significant features of this example are listed below (see figs. 22 through 24):

1. The point of initial fracture is at the upper surface at the point of maximum horizontal tensile stress (point FP on fig. 23). The type of fracture is a vertical tensile crack.
2. The vertical displacements progressively decrease in magnitude from the lower to the upper boundary. The change in the maximum vertical displacement (at $X = L/2$) at the boundaries with a change in the dimensions of the layer is shown in fig. 25.
3. Horizontal displacements are zero near the center of the layer and increase linearly to nearly equal maximum values at the upper and lower boundaries. The change in the maximum horizontal displacement ($X = 0$) at the boundaries with a change in the dimensions of the layer is shown in fig. 25.
4. The neutral axis of stress (excluding the initial hydrostatic stresses) passes through the center of the layer.

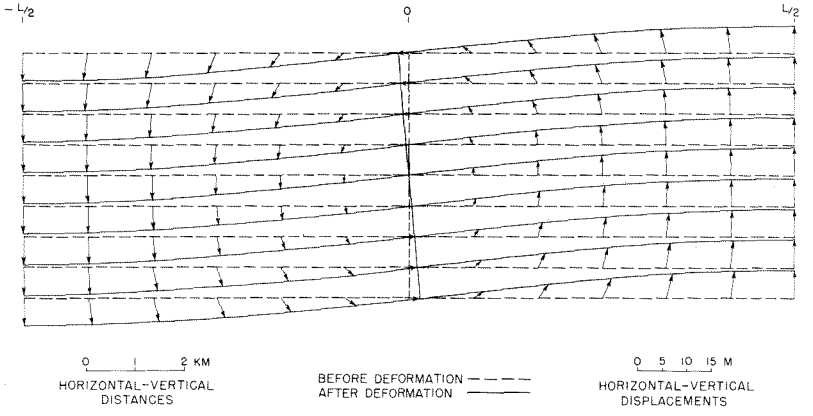

Figure 22. Example A - Displacement Field.

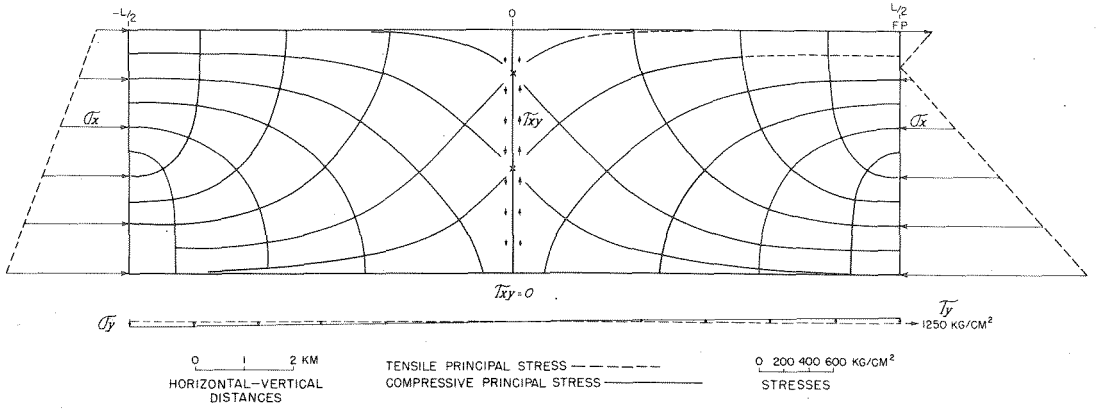

Figure 23. Example A - Stress distribution.

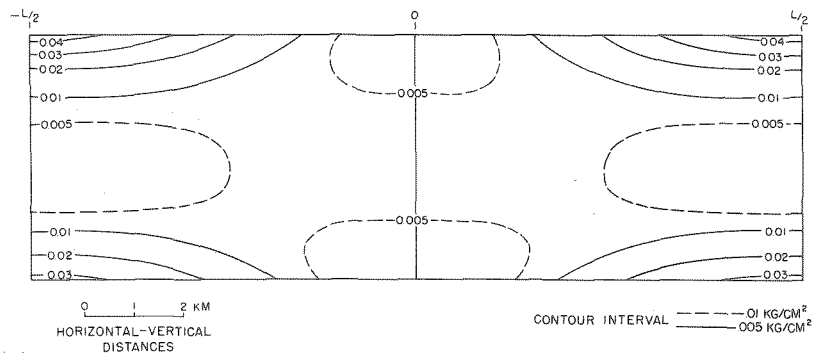

Figure 24. Example A - Distortional strain energy density.

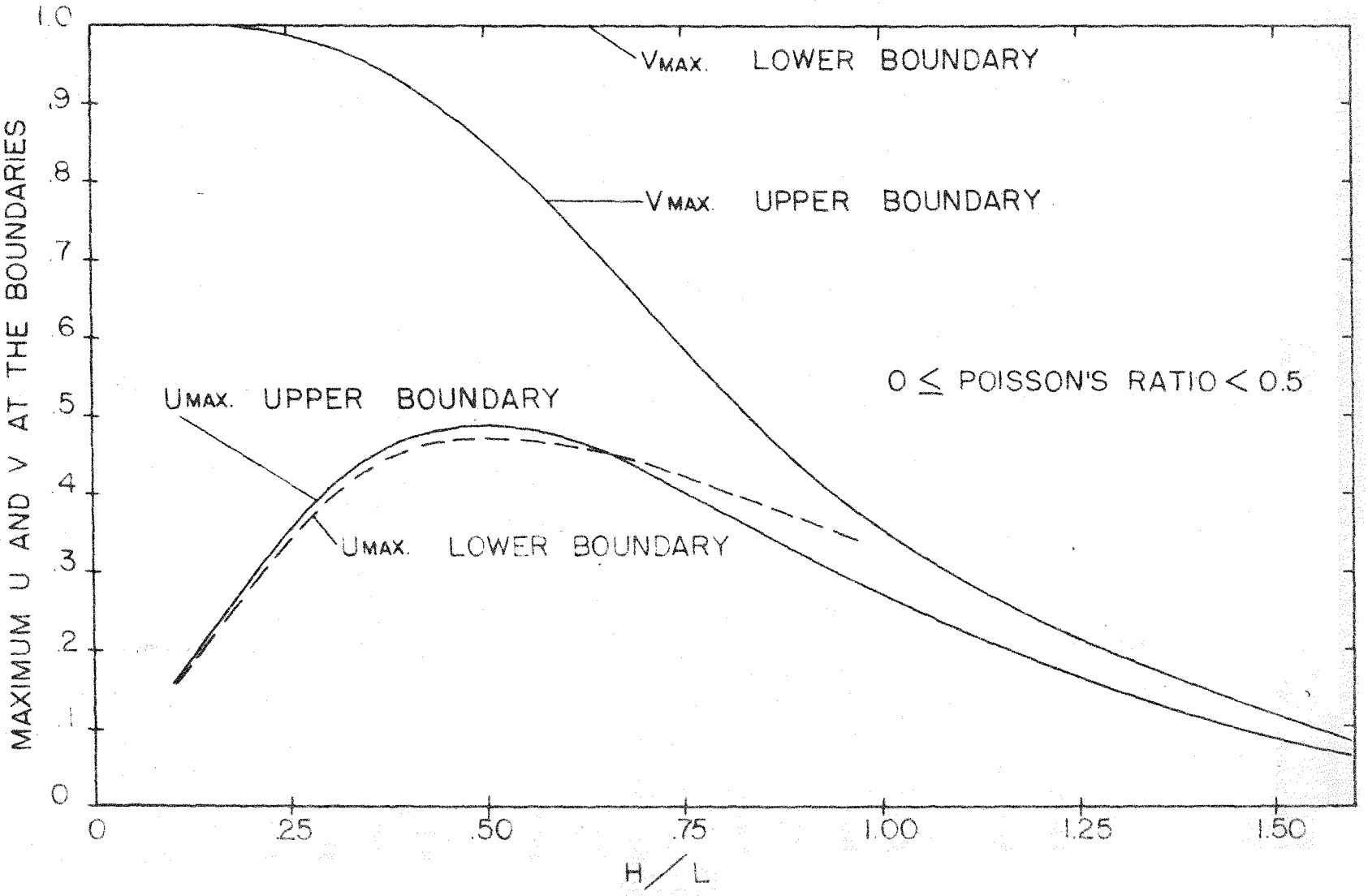

Figure 25. Example A - Horizontal and vertical displacements at the boundaries as a function of the dimensions of the layer.

5. The regions susceptible to plastic deformation are located along the lower boundary of the layer as well as the upper boundary (fig. 24).

Conclusions from the Numerical Calculations

A comparison of examples A and Id shows the maximum influence of the conditions at the lower boundary on the deformation resulting from a simple distribution of applied vertical displacement. The layers in these examples have identical dimensions, elastic constants, and fracture characteristics. Both undergo the same distributions of vertical displacement along the lower boundary. The only difference between the two is the contact between the layer and the underlying material. Example A has a frictionless contact, and example Id has a welded contact.

The following features of the deformation are not greatly affected by the nature of the contact:

1. The point of initial fracture as determined by the Mohr criterion.
2. The distribution of vertical and horizontal displacements at the upper boundary as a function of the dimensions of the layer (compare figs. 19 and 25).

The features which change when the lower boundary is frictionless are as follows:

1. The amount of applied vertical displacement before fracture is slightly greater.
2. Two additional areas are susceptible to yielding by plastic flow (compare figs. 11 and 24).
3. Horizontal displacements nearly equal to those on

the upper boundary occur along the lower boundary (compare figs. 9 and 22).

If displacement does occur along the lower contact of a layer, it will always be less than the amount found in example A. An absolutely frictionless contact between rock layers is not a reasonable boundary condition in geologic problems. For this reason, most features of the deformation in a homogeneous layer will tend to be closer to those occurring in the "welded" contact case.

Prediction of Fractures

According to the Mohr criterion, fracture occurs along lines which intersect the principal stresses at constant angles. The angle between the line of fracture and the stress trajectories is equal to (see fig. 2):

$$\theta = 45^\circ \pm \frac{\phi}{2} \,. \tag{57}$$

The extent to which the stress distributions in the analytical work can be used in predicting fractures with the Mohr criterion is difficult to determine. Any fracturing within the layer changes the stress distribution determined in the elastic analysis. If this change is confined to regions near the fracture, then formation and propagation of fractures are controlled by the original stress distribution. On the other hand, if the change extends a large distance from the fractures, formation and propagation of fractures are controlled by a stress distribution which changes continuously as the fractures are formed. One method of determining whether or not stress distributions from an elastic analysis can be used to predict fractures is to perform experiments.

EXPERIMENTAL STUDY

Introduction

Two problems were investigated in the scale model experiments. The first problem dealt with the deformation of a homogeneous layer resulting from the application of a broad curve in vertical displacement along its lower boundary. The second problem dealt with the deformation of a homogeneous layer resulting from the application of a step in vertical displacement along its lower boundary. Four types of modeling material were used on each problem. Quantitative information on displacement fields and fracturing was obtained for both problems with layers of each type of material.

Theory

A geologic structure and a scale model representation of the same structure must have degrees of similarity (Hubbert, 1937). The model must be similar in shape to the geologic structure; that is, lengths, areas, and volumes must be proportional:

$$\begin{aligned} L_m &= \lambda L_n \\ A_m &= \lambda^2 L_n^2 \\ V_m &= \lambda^3 L_n^3 \end{aligned} \tag{58}$$

(Subscripts "m" and "n" indicate model and nature, respectively.) The model must have a mass distribution similar to the original; that is, the mass for any element of volume in the model must be proportional to the mass of the corresponding element in the geologic structure:

$$dM_m = \mu dM_n \tag{59}$$

The time required for any given change of shape or position in the model must be proportional to the time required in the geologic structure:

$$T_m = \tau T_n \tag{60}$$

The constants of proportionality in the equations above, λ, μ, and τ, are the model ratios of length, mass, and time, respectively. Using these model ratios, we see that dynamic similarity between the model and the original exists if the ratio of each force acting on an element of mass in the model is proportional to the same force acting on the corresponding element of mass in the geologic structure:

$$\frac{dM_m L_m T_m^{-2}}{dM_n L_n T_n^{-2}} = \mu \lambda \tau^{-2} = \phi \tag{61}$$

All forces acting on corresponding elements of mass in the model and the original must satisfy the same model ratio of force. Model ratios of all forces must be equal to the ratio of gravity forces because the model and the original are subjected to the same gravitational field. The model ratio of gravity forces is:

$$\frac{F_m}{F_n} = \frac{dM_m g}{dM_n g} = \mu \tag{62}$$

From equation (62) we obtain the ratio of strength between the model and the original:

$$\sigma = \mu \lambda^{-2} \tag{63}$$

The model ratio of mass can be expressed as:

$$\mu = \delta \lambda^3 \tag{64}$$

where δ equals model ratio of density. Substituting equation (64) into equation (63) gives for the model ratio of strength:

$$\sigma = \delta\lambda \tag{65}$$

Replacing λ with the ratio of lengths gives:

$$L_n = \frac{\delta L_m}{\sigma} \tag{66}$$

Equation (66) can be used to establish the size of the geologic structure being modeled if the model ratios of strength and density are known.

The model ratios of time and length can not be selected arbitrarily. The model and geologic structure are subjected to the same gravitational field:

$$\frac{g_m}{g_n} = 1 = \lambda\tau^{-2} \tag{67}$$

The model ratio of time is related to the model ratio of length by:

$$\tau = \sqrt{\lambda} \tag{68}$$

A reasonable value for λ in the model experiments is 10^{-5}; that is, one centimeter in the model is equal to 1 kilometer in the geologic structure. Assuming that a geologic event takes place in a million years, about three thousand years would be required to duplicate the event in a model experiment. At first glance the time factor appears to be a serious block to successful model experiments of geologic structures.

Calculations based on the total time required to form a given geologic structure are misleading. Although the total time

is long, the time over which movement occurs may be fairly short. Present day seismic activity indicates that some structures are formed by many short period movements separated by long periods without movement. Thus, if one assumes that a structure is formed by 19,000 separate movements of one minute duration, the time required to model this structure is one hour when λ equals 10^{-5}.

Experimental Procedure

Modeling Materials

Composition. The materials used in the experiments are listed below:

Material 1	Beach sand
Material 2	Beach sand-85%, clay-15% (Enamel Sagger Ball Fire Wad, OM-4 Kentucky-Tenn. Clay Co.)
Material 3	Coarse St. Peter sand (Ottawa Silica Sands, Flint Shot)
Material 4	Fine St. Peter sand (Ottawa Silica Sands, #102)

The beach sand contains grains of quartz, feldspar, and mica. The St. Peter sand is composed entirely of quartz grains.

Density. The density of modeling materials is dependent on the amount of compaction of the material. Listed below are density values for two degrees of compaction:

	Uncompacted	Compacted
Material 1	1.3 gms/cm^3	1.6 gms/cm^3
Material 2	1.3 "	1.7 "
Material 3	1.5 "	1.7 "
Material 4	1.4 "	1.7 "

The first value is an average density for the material when it is poured into a container. The second value is an average density for the material when placed in a container by thin layers which are tamped after each layer is added.

Water Content. No water was added to any of the materials used. However, a small percentage of moisture was absorbed by the materials through contact with the atmosphere. Water content measurements showed that (1) 2.4 percent of the total weight of the clay in material 2 was water, and (2) 0.9 percent of the total weight of material 2 was water. Water content of the beach sand, on the basis of the relative percentages of sand and clay in material 2, was 0.6 percent.

Distribution of Grain Sizes. The distribution of grain sizes in the materials is shown in fig. 26.

Roundness and Sphericity. The roundness and sphericity of the sand grains in the materials are summarized in Table 2. Numerical values were assigned for the degree of roundness and sphericity by comparing the grain shapes with published charts (Krumbein and Sloss, 1951, p. 81). Grains which approach a perfect sphere in shape have the highest values of roundness and sphericity (maximum value equals 1.0).

Strength. Measurements of the strength of the modeling materials were made in three ways. In the first, the fracture characteristics for the material, τ_0 and ϕ, were determined from the behavior of the material in a rectangular container when support for one vertical edge was removed. The angle of fracture

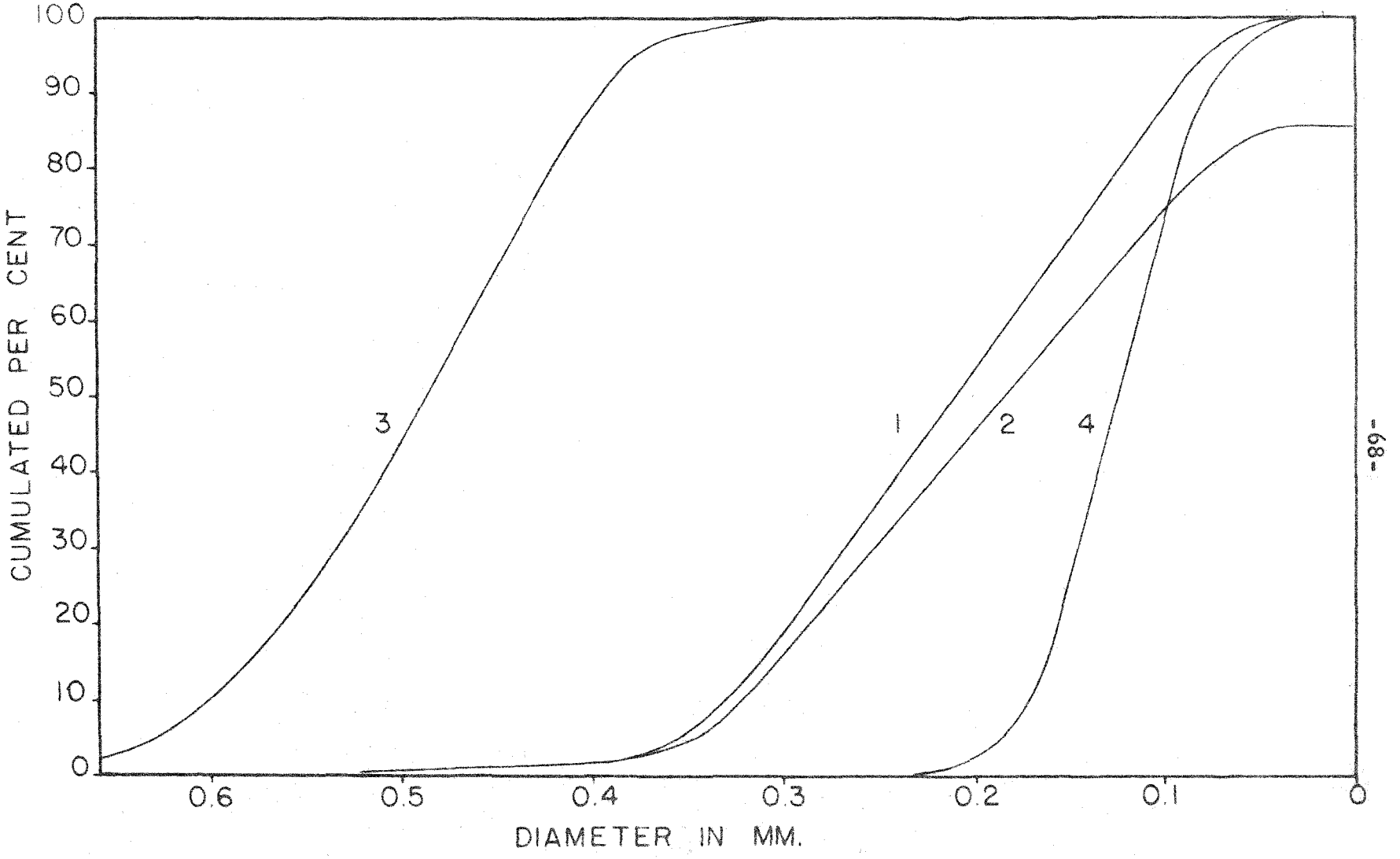

Figure 26. Distribution of grain sizes in the modeling materials.

Material	Size Interval in mm.	Roundness		Sphericity	
		Range	Average	Range	Average
No. 1 and No. 2	--.50	.1-.9	.5	.3-.9	.7
	.50--.30	.1-.9	.5	.3-.9	.7
	.30--.18	.1-.9	.5	.3-.9	.6
	.18--.15	.1-.9	.4	.3-.9	.6
	.15--.10	.1-.9	.4	.3-.9	.7
	.10--.07	.1-.9	.3	.3-.9	.7
	.07--.06	.1-.9	.5	.3-.9	.7
	.06--	.1-.9	.4	.3-.9	.6
No. 3	All grains	.8-1.0	.9	.8-1.0	.9
No. 4	--.22	.5-.9	.8	.3-.9	.7
	.22--.18	.5-.9	.7	.5-.9	.7
	.18--.15	.3-.9	.7	.3-.9	.7
	.15--.12	.3-.9	.6	.3-.9	.7
	.12--.10	.3-.9	.6	.3-.9	.7
	.10--.09	.3-.9	.6	.3-.9	.7
	.09--	.1-.9	.5	.3-.9	.7

Table 2. Roundness and sphericity of the grains in the modeling materials.

caused by removal of support at one vertical edge is related to the angle of internal friction by:

$$\theta = 45° - \frac{\phi}{2} \tag{69}$$

If the material possesses cohesive strength, an unsupported vertical edge of a thin layer will stand without fracturing. The maximum thickness or critical height (h_{cr}) without fracture is related to the cohesive strength by (Tschebotarioff, 1952, pp. 169-172):

$$\tau_o = \frac{\rho g h_{cr.}}{4 \tan \theta} \tag{70}$$

(Equations (69) and (70) assume the special linear case of the Mohr fracture criterion.) Equation (70) fails to consider the tensile stresses introduced by movement of material prior to fracture. These tensile stresses are located near the surface close to the unsupported edge. Inasmuch as the tensile strength of granular materials is low, vertical tensile fractures form at the surface before shear failure occurs lower in the layer. The effect of the tensile cracks is to reduce the observed critical height. The maximum depth of the cracks is estimated to be one half of the observed critical height (Tschebotarioff, 1952, p. 171). Thus, the maximum effect of the tensile cracks can be considered in a qualitative manner by multiplying the observed critical height by 3/2.

The above method was applied to all modeling materials with the following results:

	Uncompacted		Compacted	
	τ_o (dynes/cm^2)	ϕ	τ_o (dynes/cm^2)	ϕ
Material 1	0	34°	0	54°
Material 2	140-210	42°	1100-1700	58°
Material 3	0	22°	0	45°
Material 4	0	27°	0	52°

The strength measurements were taken under conditions similar to those used in the experiments. In the uncompacted tests, material was poured into the box. In the compacted tests, material was placed in the box by layers which were moderately tamped after each layer was added.

The second procedure used for measurement of strength was the triaxial shear test (Tschebotarioff, 1952, pp. 130-135). Tests were performed on material 2, but they failed to establish the value of cohesion because of apparatus limitations at low confining pressures. However, the triaxial tests did show that material 2 fractures according to the linear form of the Mohr criterion.

The last procedure used for measurement of strength was the controlled strain shear test (Tschebotarioff, 1952, pp. 143-145). With these tests, the shear strength of material 2 was determined under very low confining pressures. Tests were conducted for two degrees of compaction, strong and moderate. Results of these tests are shown in fig. 27. Note that the material fractures according to the special linear case of the Mohr criterion. Although the data are badly scattered at low normal stresses, the best curves drawn by eye give the following values of τ_o and ϕ for material 2:

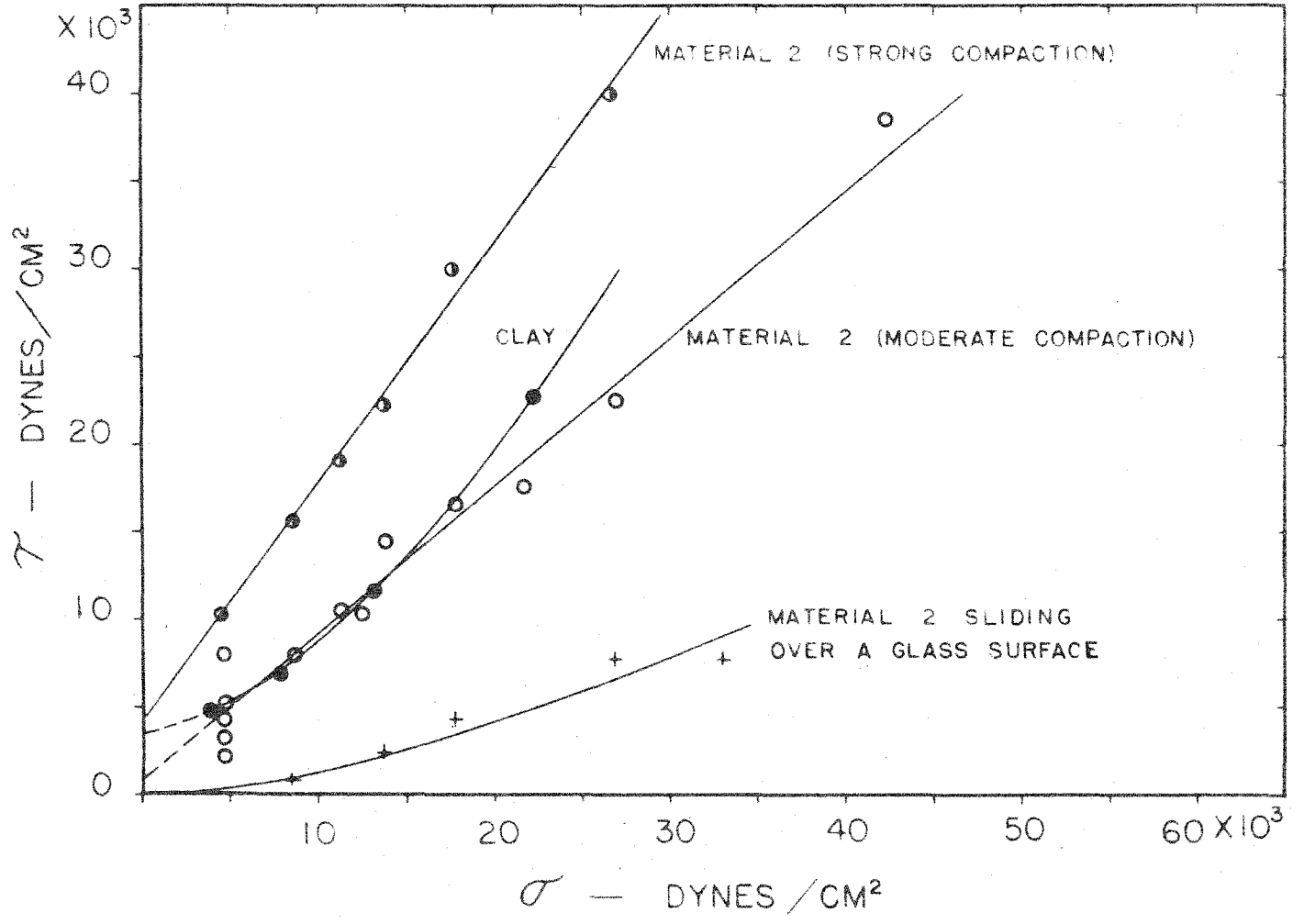

Figure 27. Results of controlled strain shear tests.

	Strong Compaction	Moderate Compaction
τ_o	4000 dynes/cm^2	1000 dynes/cm^2
ϕ	53°	40°

Plotted on fig. 27 are data for controlled strain shear tests on moderately compacted dry clay. The relatively high value of τ_o, 3500 c.g.s., indicates that the τ_o values obtained for the mixture of clay and sand in material 2 are reasonable.

The strength measurements illustrate one important characteristic of the modeling materials--an increase in strength with an increase in compaction. Inasmuch as the degree of compaction is difficult to control in the experiments, compaction appears to present a serious problem in model experiments. However, the strength measurements are only indicative of the material's strength as long as it is not disturbed in any manner. In all of the experiments, the material is disturbed before fracture and during fracture. This deformation reduces the amount of compaction and therefore the strength. Strength measurements made on uncompacted materials come nearest to duplicating the strength properties of materials in the experiments after some initial disturbance.

Restrictions Placed on the Scale Models by the Modeling Materials. Two properties of the modeling materials place restrictions on the type of rock layer which can be modeled in the experiments. Densities of the model materials are not influenced by the small amount of overburden used in the models. Thick shale layers which increase in density with increase in overburden can not be duplicated by these materials. Fortunately, there are many rock types whose densities are nearly independent of overburden (Birch,

et al., 1942, p. 62).

The model materials described above fracture according to the linear form of the Mohr fracture criterion. In order to have a correct model, strength properties of the model material and the rock of the geologic structure must be similar. Therefore, materials 1 through 4 can only be used to model rock which also fractures according to the linear form of the Mohr fracture criterion. A proper match of strengths requires that cohesive strengths be proportional and angles of internal friction equal.

Model Apparatus

The apparatus used for the experiments is shown in fig. 28. The inside dimensions of the upper portion of the box, which has glass sides and wooden ends, are 44.5 by 22.8 by 11.4 centimeters. The bottom of the box is fitted with three felt edged blocks for experiments that require steps in vertical displacement at the base of a layer. Each block can be moved independently in the vertical direction by four screws projecting through the bottom of the box. The felt edges of these blocks prevent passage of material between the blocks and the glass faces.

The bottom of the box is fitted with a felt edged rubber pad for experiments that require gradual changes in vertical displacement at the base of a layer. The central and end portions of the rubber pad can be moved independently in the vertical direction by screws projecting through the bottom of the box.

The ends of the box are fitted with vertical blocks which follow the vertical movement of the end blocks or end portions of the rubber pad. This design feature eliminates the drag which

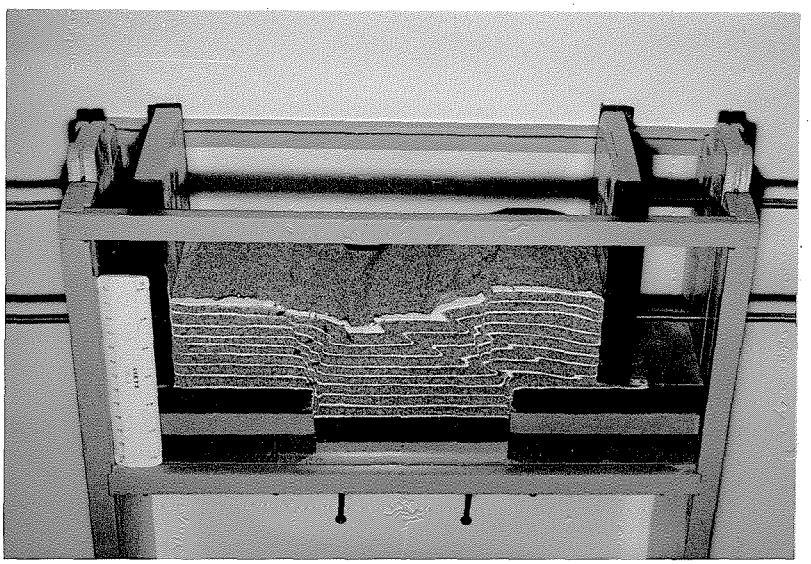

No. 8 Material 1

Figure 28. Model apparatus.

would occur if the ends of the box were fixed. Each end block can be displaced laterally by turning two large machine screws projecting out of the ends. Thus, simultaneous vertical and horizontal displacement of the material in the box is possible (see fig. 28).

One feature of the apparatus may influence the experimental results--the drag of the material along the glass face. Theoretically this drag should be zero in order that the model be a valid representation of the deformation normal to the long axis of a geologic structure. Unfortunately, experimental data can not be obtained without some drag along a glass face.

Controlled strain shear tests were performed to find the coefficient of friction between material 2 and a glass surface. The results of these tests are shown in fig. 27. The normal stress of material 2 against the glass face in the box ranges from 0 to a maximum of 10,000 c.g.s. The coefficient of friction for this range of normal stress is 0.12. This result agrees closely with the coefficient of friction of quartz grains moving over a solid quartz plate (Tschebotarioff, 1952, pp. 122-124) or dry metal moving over dry metal (Hodgman, 1955, p. 1990). Inasmuch as the measured coefficient for material 2 moving over a glass surface is only one fifth to one twenty-fifth the coefficient of friction of material 2 moving over material 2, drag along the glass face probably does not have a major influence on the experimental results.

Test Procedure

Setup. Material was placed in the box in successive layers

of 0.6 to 1.2 centimeters thickness. Each layer was separated from adjacent layers at the glass face by thin marker lines of flour or quartz sand dyed black. These marker lines extended a short distance into the box from the glass face. Two degrees of compaction were used after each layer was added--zero and approximately 10,000 c.g.s.

Test Run Procedure. The displacements were applied to the base of the layer in small increments. Direct and oblique photographs of the model were taken between intervals of displacement (figs. 29 and 30). In some instances, several increments of displacement was recorded on a single piece of film (figs. 31 and 32). The latter procedure was used exclusively for the determination of displacement fields. The total time required for a complete experiment was about one hour.

Discussion of the Experimental Results

Introduction

Two types of experiments were performed in the model studies. In Type I, a broad curve in vertical displacement was applied to the lower boundary of a homogeneous layer. In Type II, a step in vertical displacement was applied to the lower boundary of a homogeneous layer. Layers of each kind of modeling material were used one or more times in both types of experiments. A summary of the experiments performed is given below:

	No. of Experiments with Material				Total No. of Experiments
	#1	#2	#3	#4	
Type I	1	2	3	1	7
Type II	2	13	3	1	19

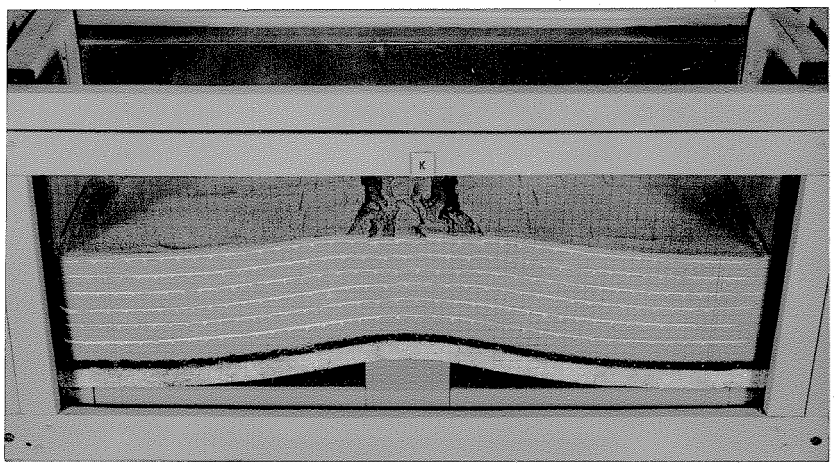

No. K Material 2

(Grid lines are 0.5 cm. apart)

Figure 29. Type I experiment - oblique photograph.

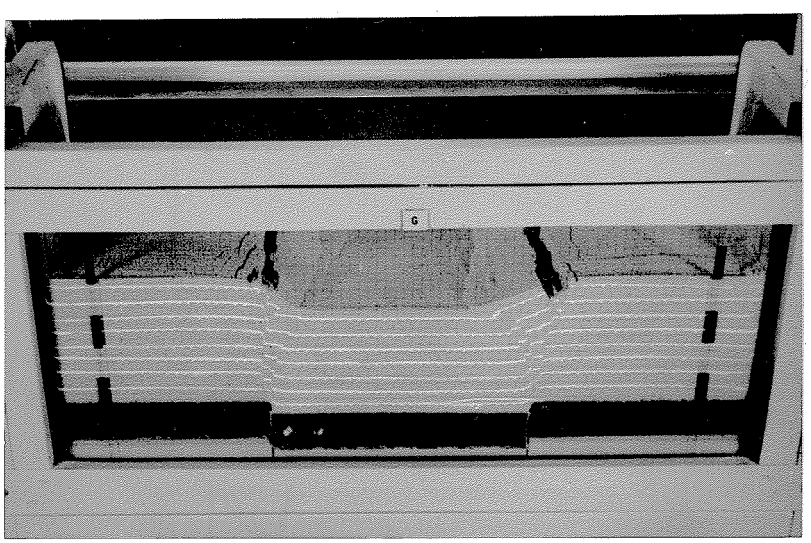

No. G Material 2

(Grid lines are 0.5 cm. apart)

Figure 30. Type II experiment - oblique photograph.

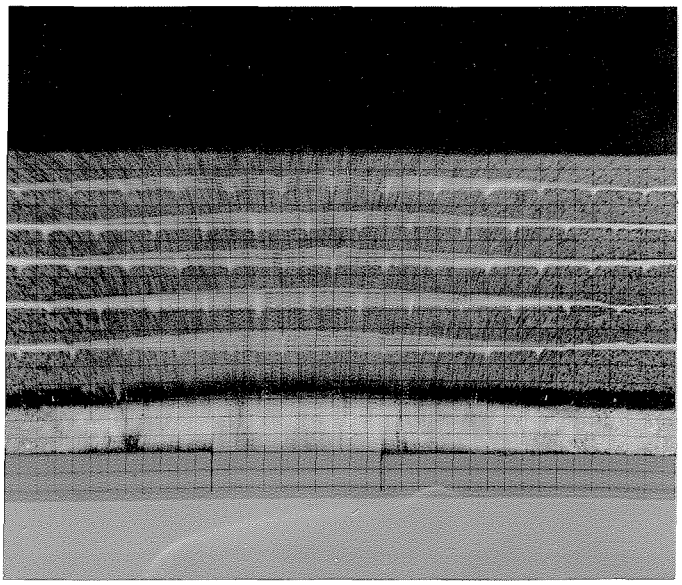

No. 0 Material 1

(Grid lines are 0.5 cm. apart)

Figure 31. Type I experiment - multiple exposure photograph.

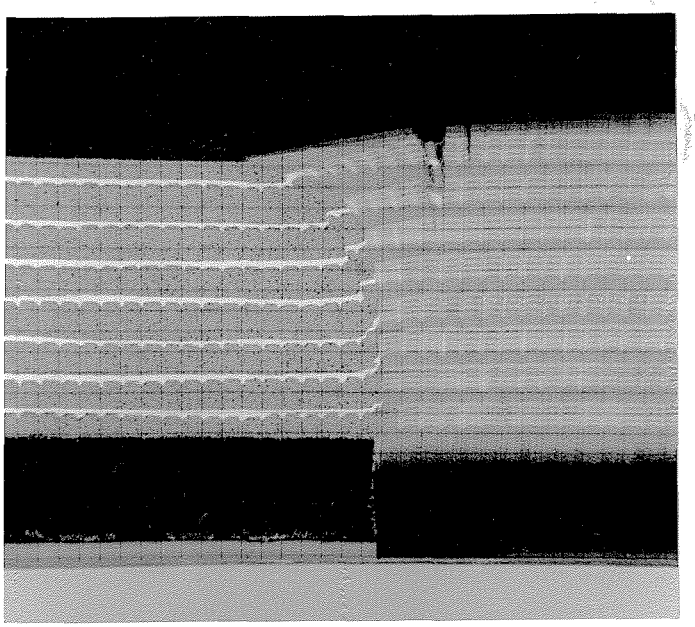

No. G Material 2

(Grid lines are 0.5 cm. apart)

Figure 32. Type II experiment - multiple exposure photograph.

Several figures showing different stages of deformation in the model experiments have been used in the following discussion of the experimental results. These figures are tracings of photographs taken during the experiments. The coordinates for the figures are the same as those used in the numerical examples (see fig. 1).

Type I Experiments

Displacement Fields. Examples of the observed displacement fields are given in fig. 33. The important features of the displacement fields were:

1. No measurable change in the displacement field with a change in the composition of the layer.
2. An increase in horizontal displacement from the lower to the upper boundary of the layer.
3. Maximum horizontal displacement at or very near the point of inflection in the fold ($X = L/2$ or $-L/2$).
4. A decrease in vertical displacement from the lower to the upper boundary of the layer.

Fractures with Material 2. Only models in which layers of material 2 were used produced fracturing at large displacements (see No. A and No. K of fig. 34). The sequence of fracture formation with increase in applied displacement was as follows:

1. Vertical tensile cracks at the crest of the fold.
2. A series of normal faults at or near the crest of the fold.
3. Additional normal faults intersecting the surface

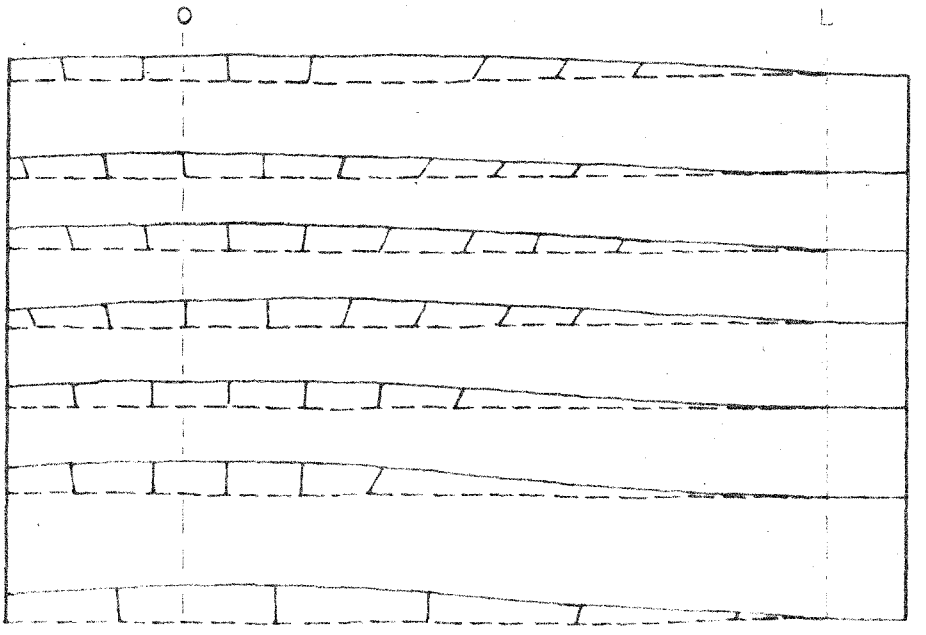

NO. K MATERIAL 2

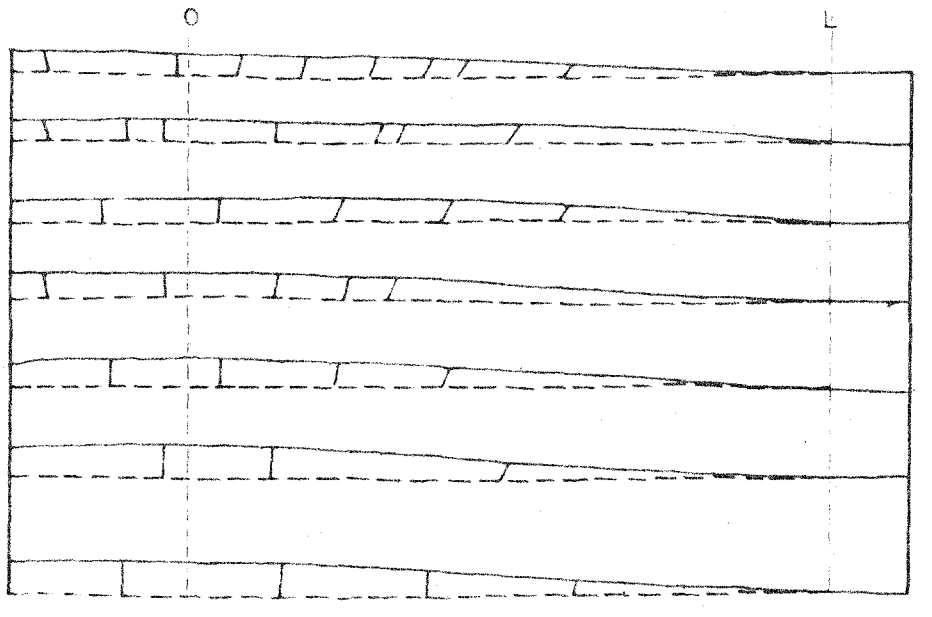

NO. O MATERIAL 1

0 1 2 3 CM.
SCALE

BEFORE DEFORMATION - - -
AFTER DEFORMATION ——

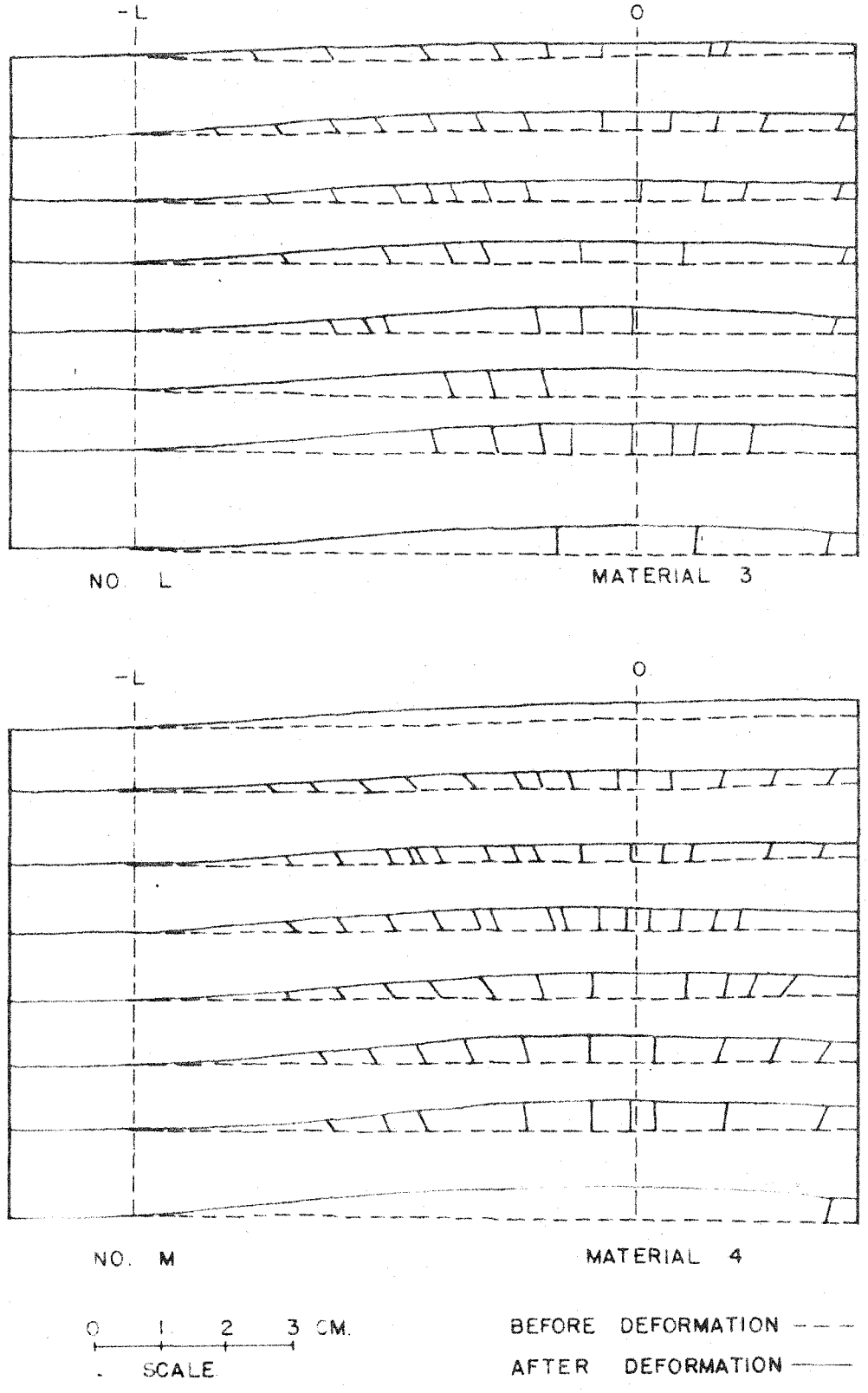

Figure 33. Displacement fields--Type I experiments.

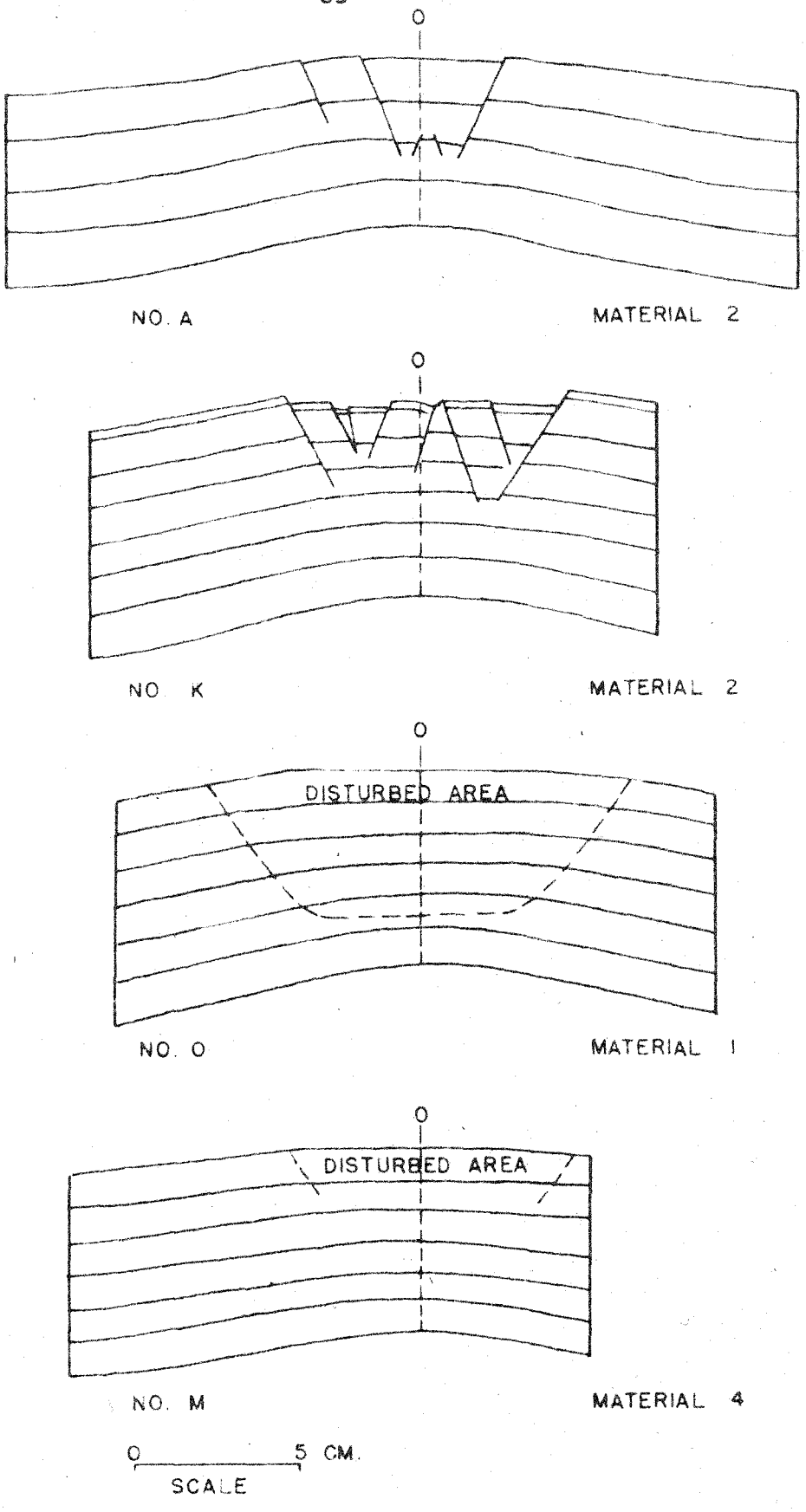

Figure 34. Fracturing and folding--Type I experiments.

at progressively greater distances from the crest of the fold.

The depth of the tensile cracks was never greater than one centimeter, usually much less. The major normal fractures were straight, had maximum displacement at the surface, and dipped towards the axis of the fold. Average dip of the major normal faults was 65 degrees.

The average angle of fracture and the depth of the tensile cracks (equivalent to the unsupported height in the strength measurements) can be used to determine the strength of the layer at the time of fracture. The computed angle of internal friction from equation (69) is 40 degrees. The computed cohesive strength from equation (70) is 200 c. g. s. These values are nearly identical to the values found in the strength measurements of uncompacted layers of material 2.

Deformation with Materials 1, 3, and 4. No fracturing was observed in the experiments with layers of material 1, 3, and 4. However, a cup shaped area over the crest of the fold was disturbed by the folding (see No. 0 and No. M in fig. 34). The main features of the disturbed zone were blurring of the marker lines, flattening of the upper boundary, and thinning of the layer. The thinning over the crest of the fold was about 6 per cent of the original thickness for an applied vertical displacement of one centimeter at $X \approx 0$, $Y \approx H$.

Type II Experiments

Displacement Fields. Examples of the observed displacement fields are given in fig. 35. The important features of the

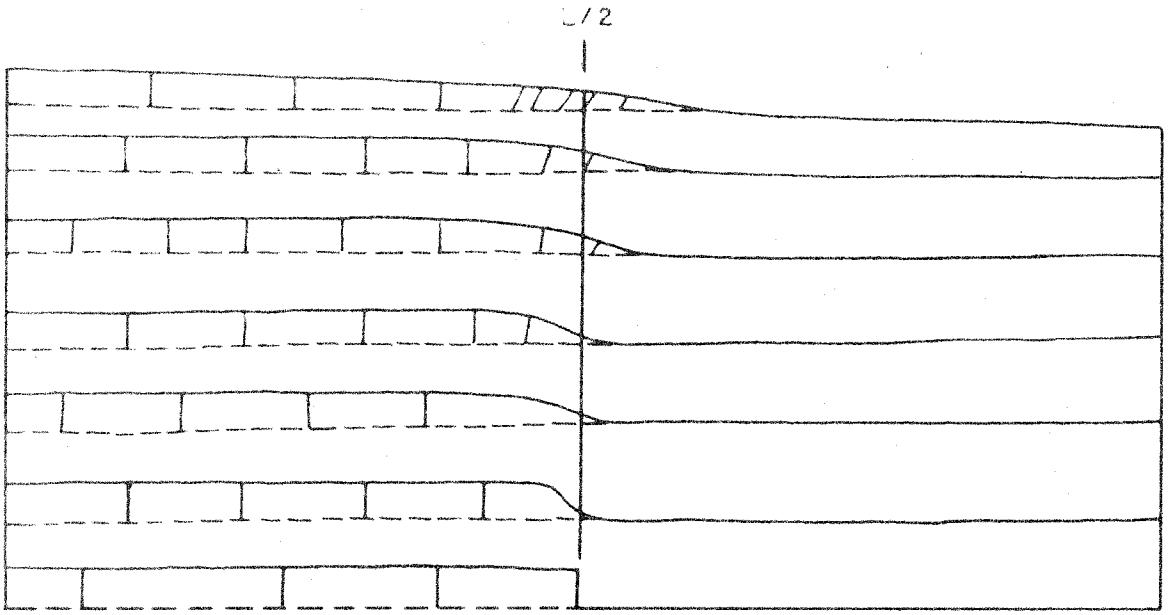

NO. P

MATERIAL 1

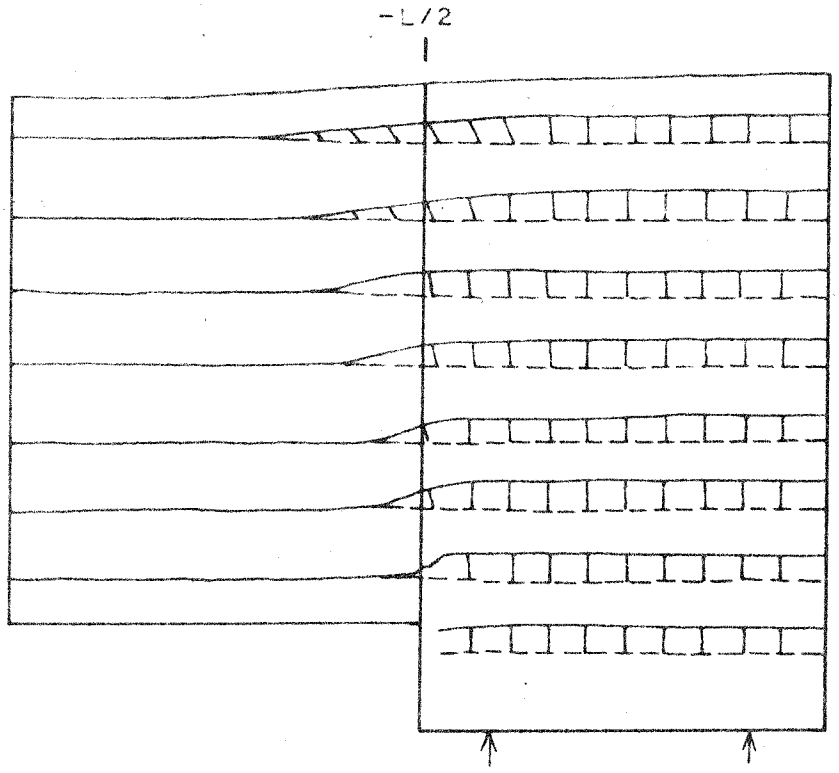

NO. G

MATERIAL 2

0 1 2 3 CM.

SCALE

BEFORE DEFORMATION - - - - -

AFTER DEFORMATION ———

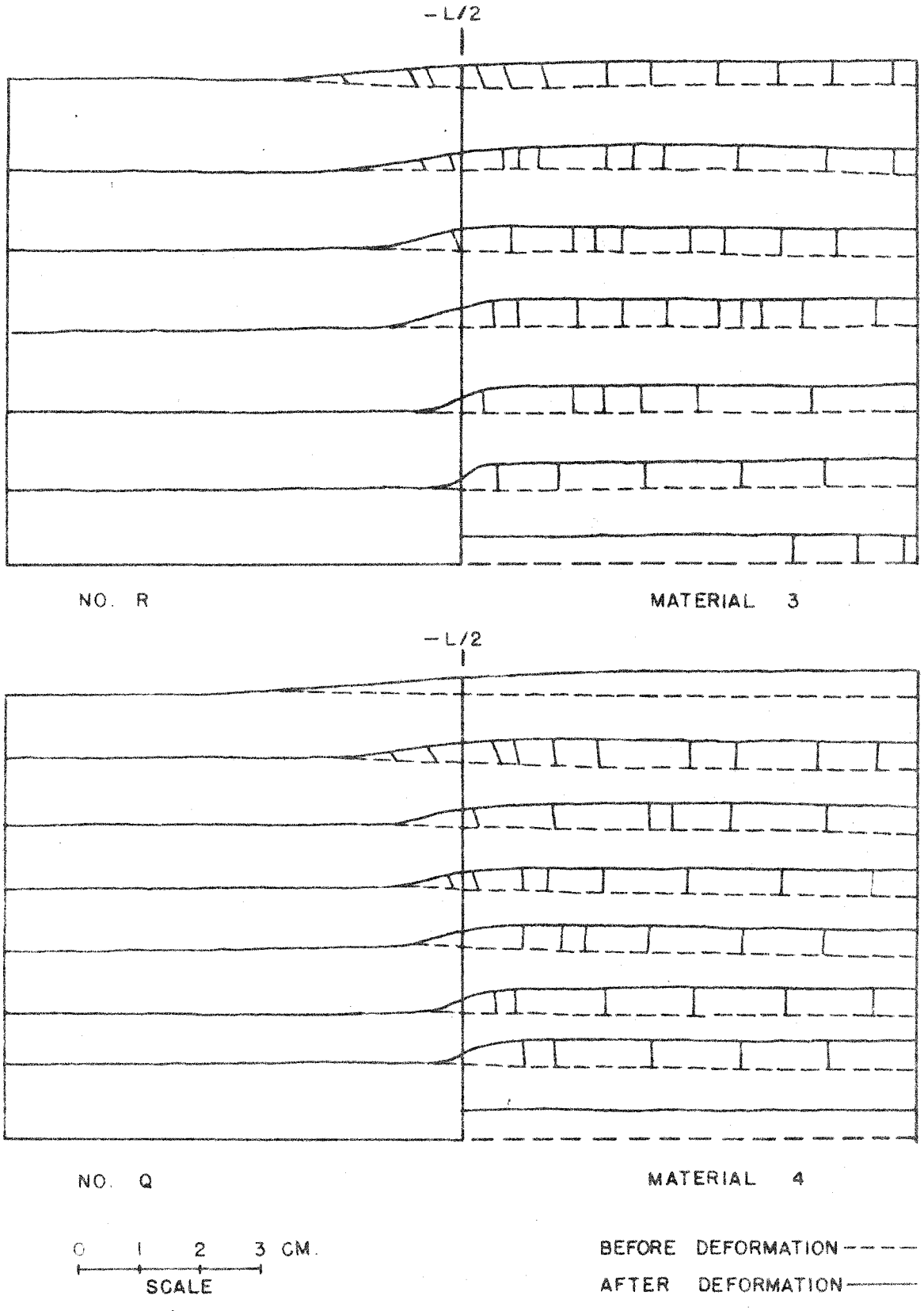

Figure 35. Displacement fields--Type II experiments.

displacement fields were:

1. No measurable change in the displacement field with with a change in the composition of the layer.
2. An increase in horizontal displacement from the lower to the upper boundary of the layer.
3. Maximum horizontal displacement at or very near $X = L/2$ or $-L/2$ along any horizontal line through the layer.
4. A progressively less abrupt transition in vertical displacement from the lower to the upper boundary of the layer.

Fractures with Material 2. Type II experiments with layers of material 2 produced distinct fractures at large applied vertical displacements (see fig. 36). The usual sequence of fracture formation with increasing applied vertical displacement was:

1. Simultaneous or nearly simultaneous formation of tensile cracks at the upper boundary and shear fractures at the lower boundary.
2. Propagation of one or more shear fractures (reverse faults) to the surface, and deepening and widening of the tensile cracks (see fig. 36).
3. Formation of normal faults in the tensile crack zone (see No. D of fig. 37).
4. Formation of a major normal fault from the tensile crack zone to the edge of the uplifted block at the lower boundary of the layer (see No. C of fig. 37).

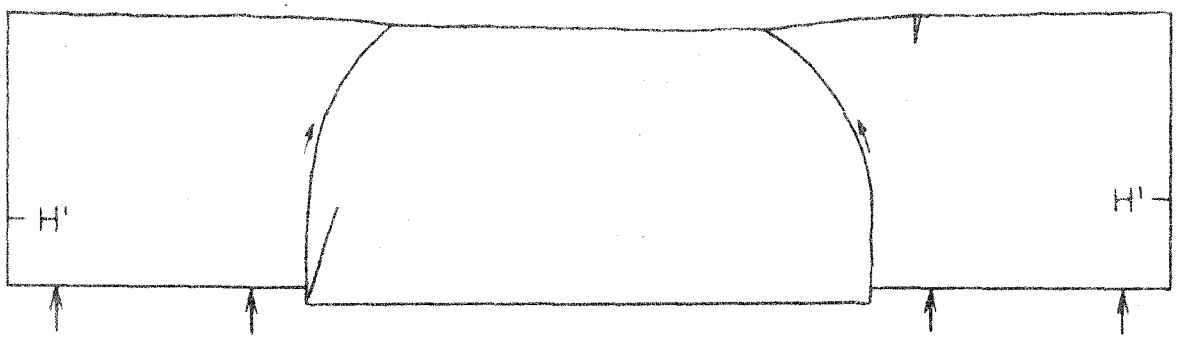

NO. 0 MATERIAL 2

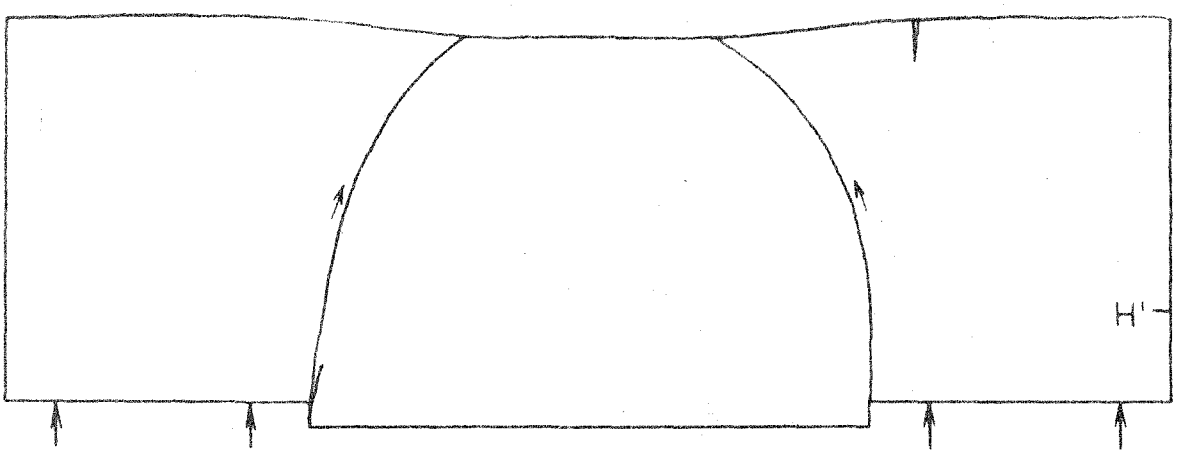

NO. 1 MATERIAL 2

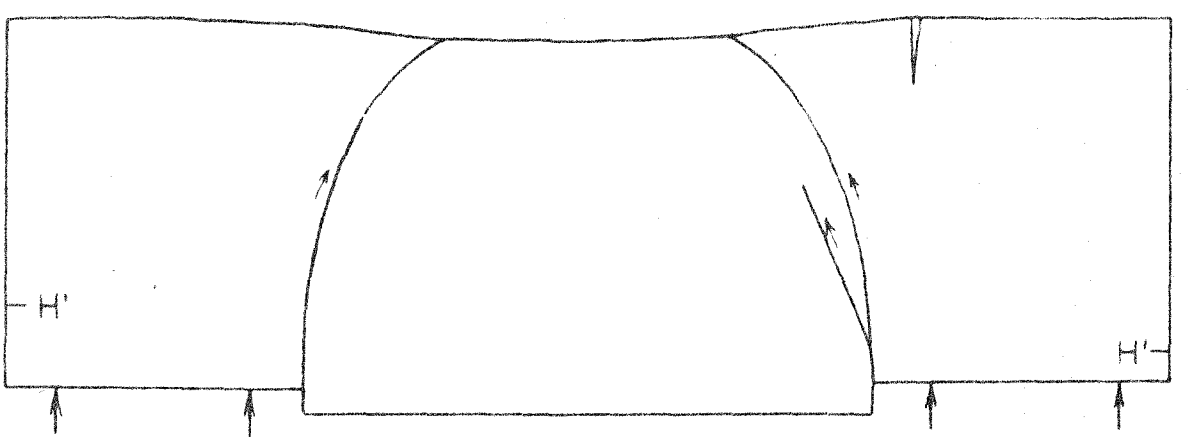

NO. 2 MATERIAL 2

0 5 CM
SCALE

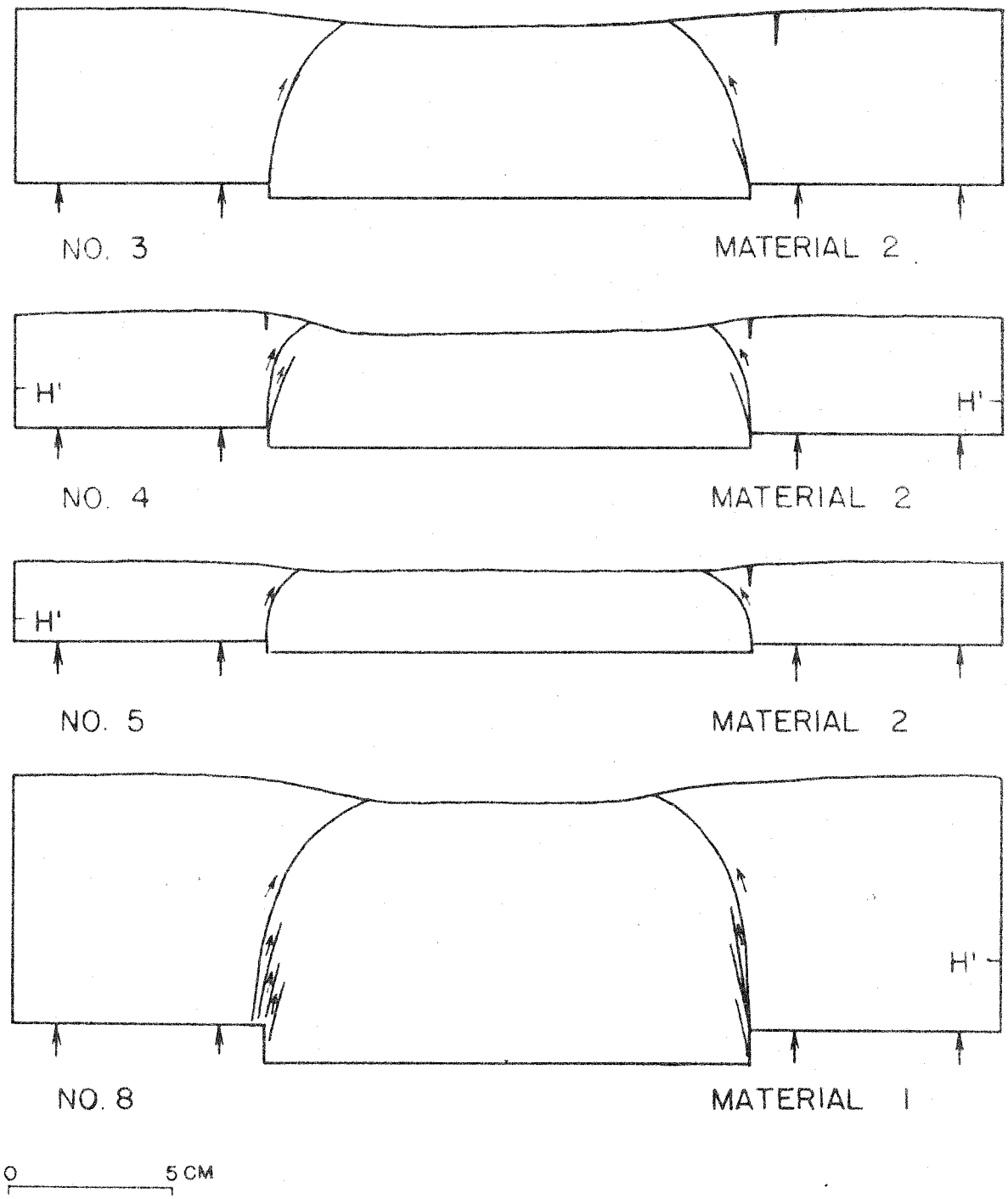

Figure 36. Fractures--Type II experiments.

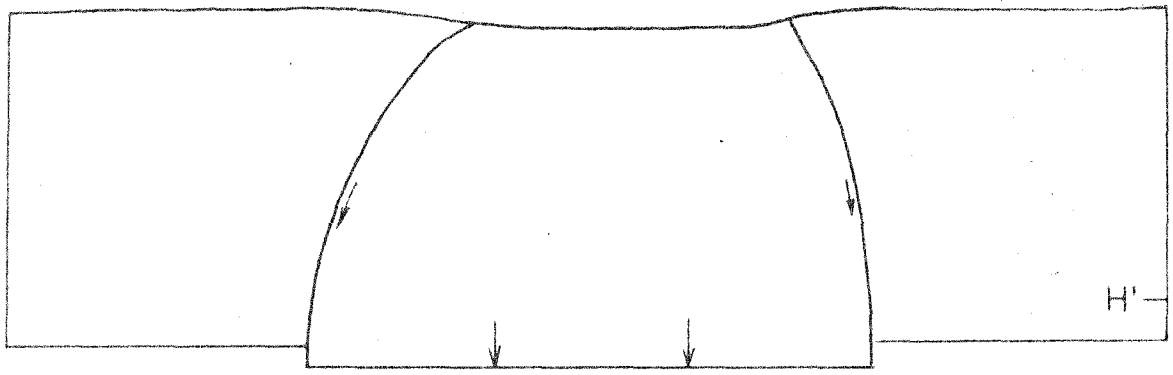

NO. 9 MATERIAL 2

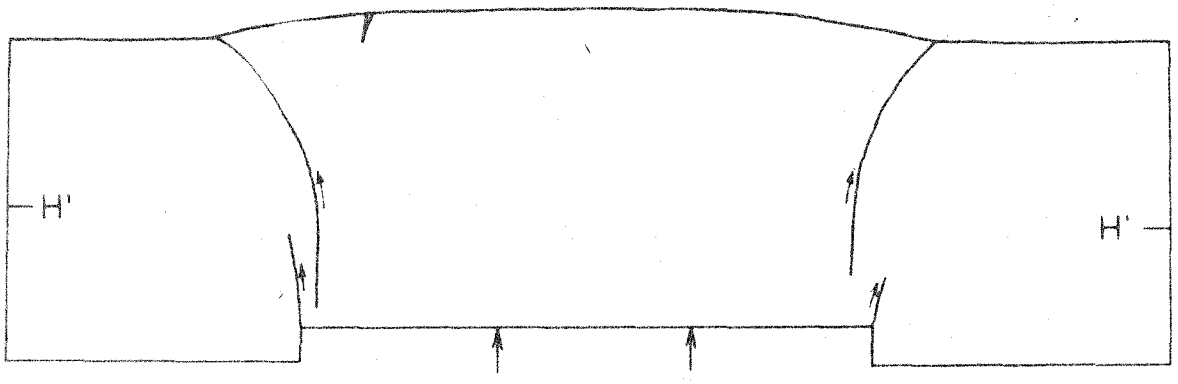

NO. B MATERIAL 2-UC

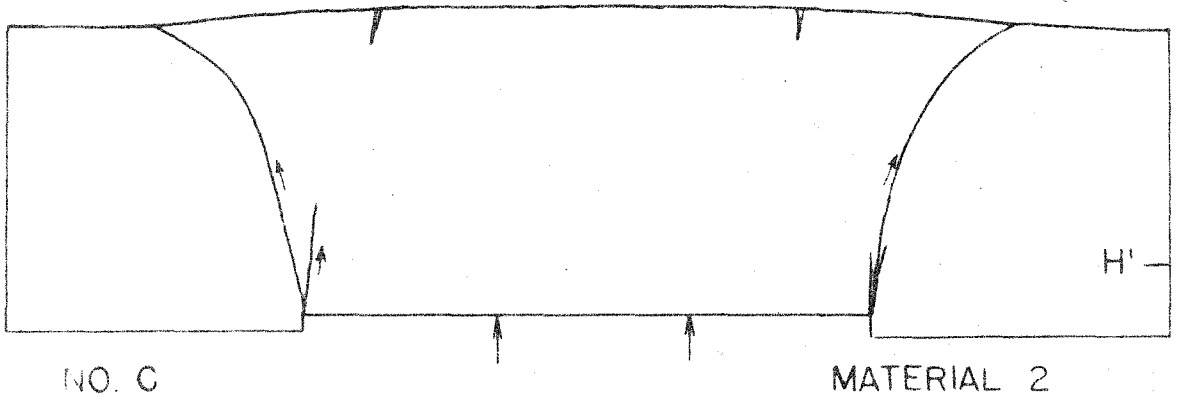

NO. C MATERIAL 2

0 5 CM
SCALE

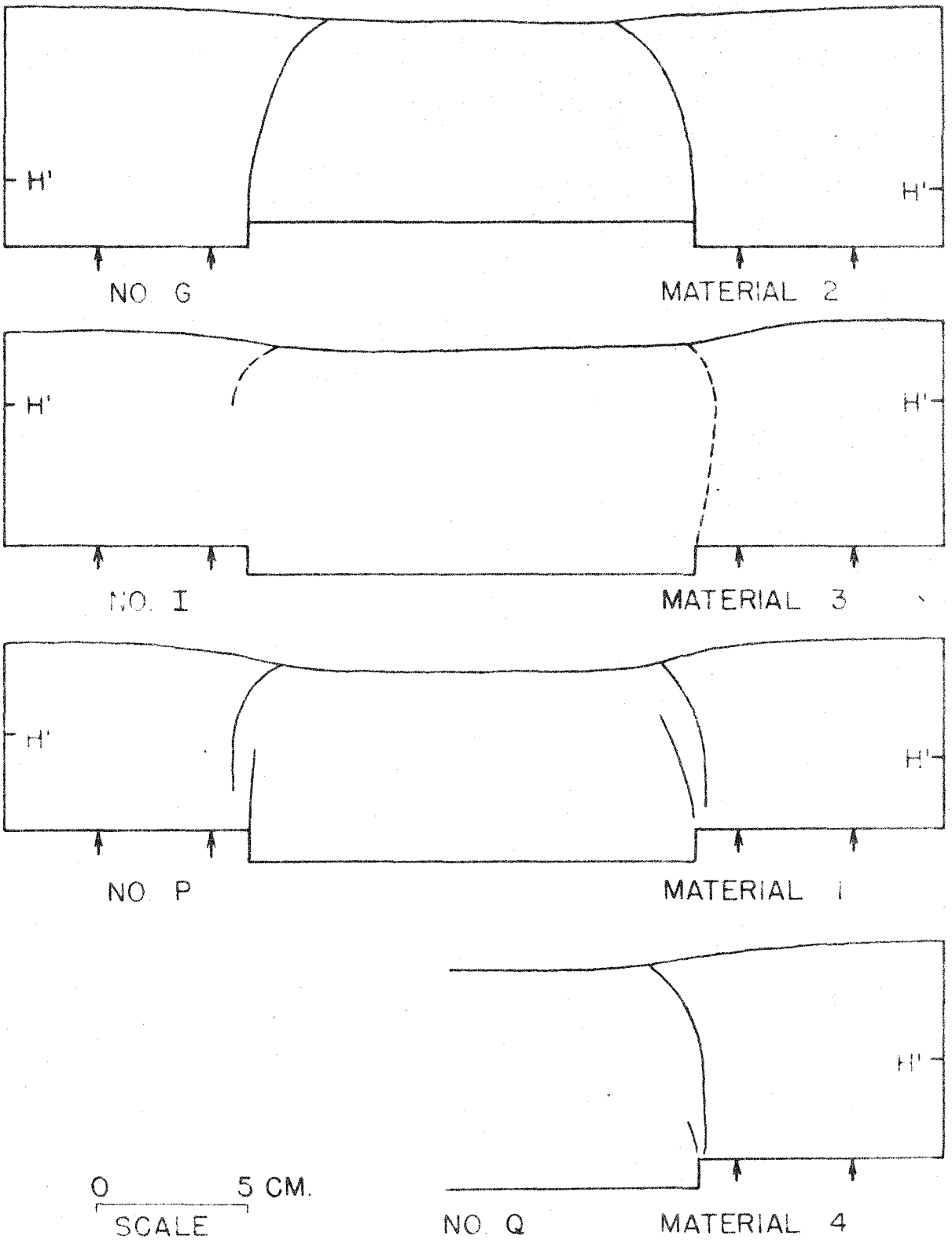

Figure 36 (Cont'd). Fractures--Type II experiments.

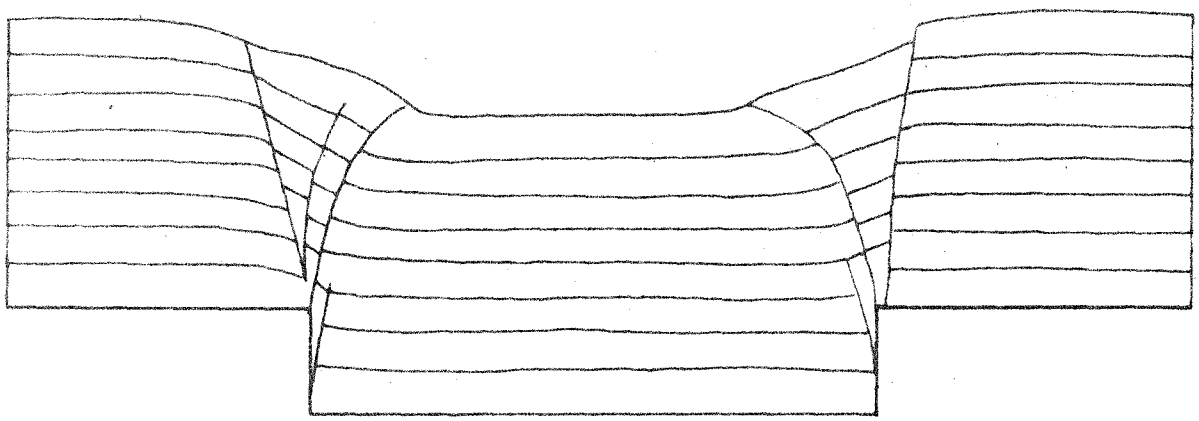

NO 8 MATERIAL 1

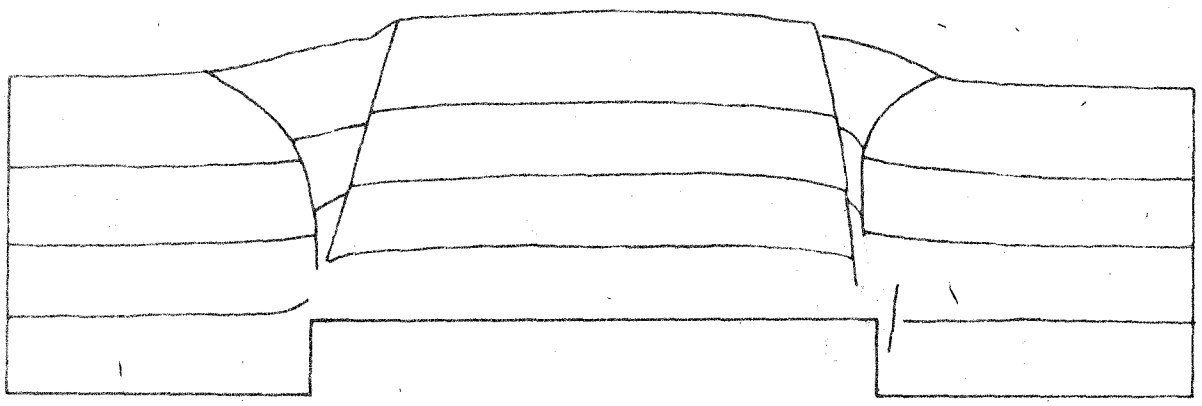

NO. B MATERIAL 2 UC

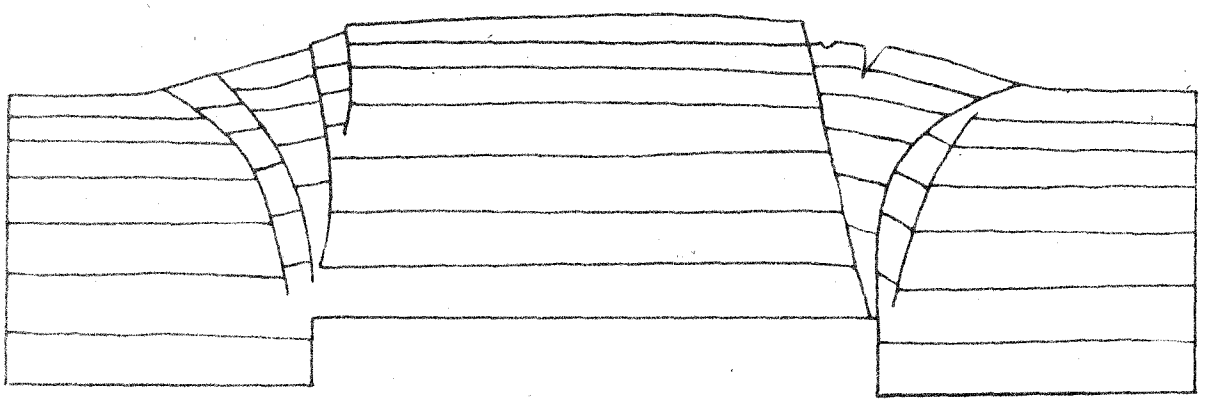

NO. C MATERIAL 2

0 5 CM.
SCALE

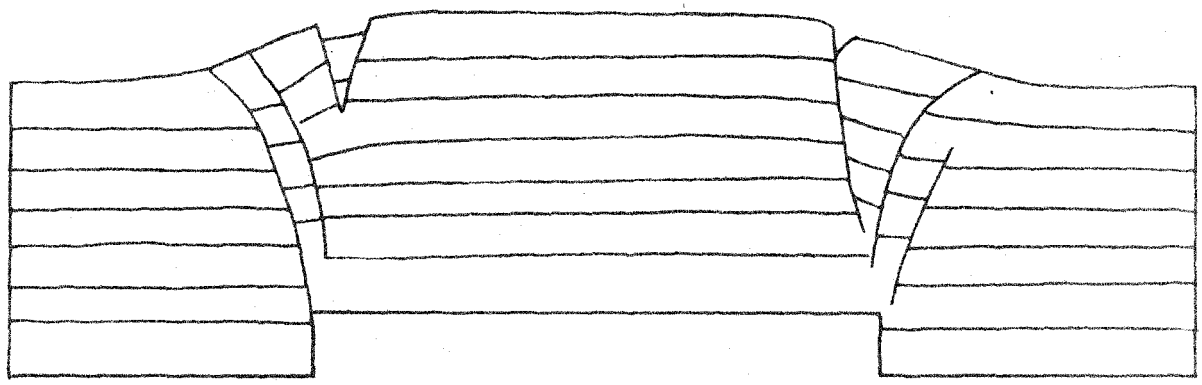

NO. D MATERIAL 2

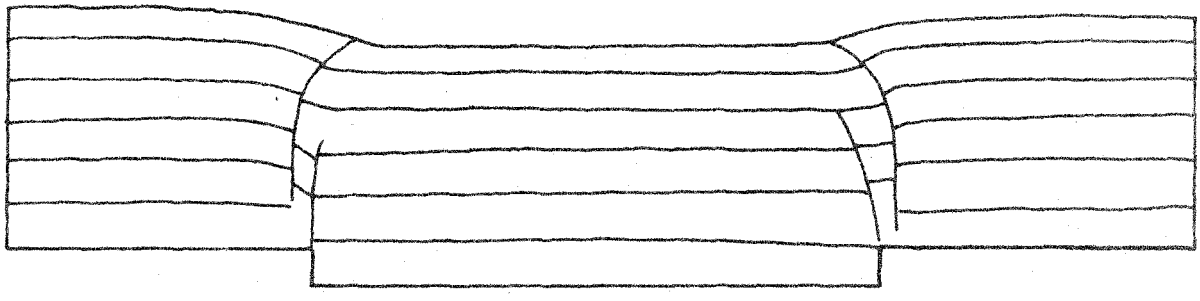

NO. P MATERIAL 1

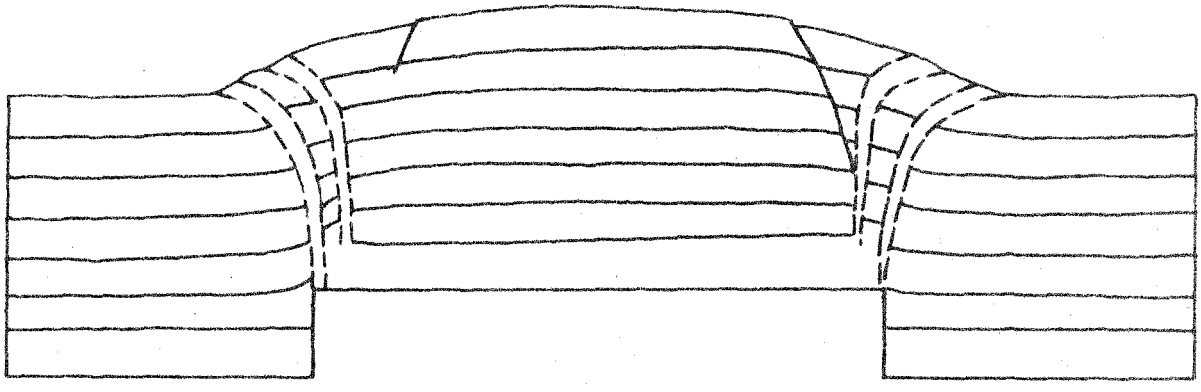

NO. Q MATERIAL 4

0 5 CM.
SCALE

Figure 37. Fracturing and folding--Type II experiments.

In most of the experiments a series of reverse faults rather than a single fault formed at the edge of the uplifted block. Formation of these fractures followed a definite sequence--progressively younger fractures started at progressively smaller angles to the vertical edge of the uplifted block. The end result was a series of diverging fractures: the oldest starting at about 8 degrees to the vertical, and the youngest starting vertically. Most of the fractures that started at an angle to the vertical only propagated a short distance. Many of these fractures were probably undetected in the experiments. In general, the younger fractures, which started vertically, eventually extended all the way to the upper surface. The applied vertical displacement that was required to propagate a shear fracture all the way to the upper surface was equal to about one twentieth (1/20) of the total length of the fracture. The same ratio between applied displacement and length of fracture (1 to 20) appeared to hold for all intermediate stages in the development of the fracture as well.

The most interesting feature of the reverse faults (see figs. 36 and 37) was the curvature of the line of fracture away from the uplifted block. Two factors influenced the curvature of the reverse faults: (1) the thickness of the layer, and (2) the number of short reverse faults formed before a particular reverse fault propagated to the surface. The influence of the second factor on curvature was eliminated in the study of these fractures by omitting the vertical portion of the fractures in the curvature measurements. These measurements were correlated with effective thicknesses (H') of the layers which were the vertical components of the curved portions of the fractures (see fig. 36).

Curvature measurements for three intervals of effective thickness are summarized in fig. 38. Although curvature measurements in adjacent intervals of effective thickness overlap, the mean values in each interval show a small systematic change of curvature with the effective thickness of the layer. The fractures have progressively greater curvature, and progressively lower dip at the upper surface, with a decrease in the effective thickness.

The curvature of the reverse faults was independent of the relative movement of the blocks. In experiment No. 9 (fig. 36), the center section was allowed to drop while the end sections remained stationary. The reverse faults produced by this mode of displacement were not appreciably different from the reverse faults produced by pushing up the end sections while keeping the center section stationary (Nos. 0, 1, and 2 of fig. 36).

In all of the Type II experiments with material 2, displacements occurred along the reverse faults after they had reached the upper surface. As a result of this movement, thin wedges of material at the fault edge of the uplifted block were thrust out over the upper surface of the stationary blocks (see fig. 37). In experiment No. G, the pointed edge of the wedge of material was moved a distance of 0.5 centimeters horizontally after 2.0 centimeters of applied vertical displacement at the lower boundary (see fig. 32).

In most of the experiments, vertical tensile cracks appeared at the surface at nearly the same time as the shear fractures formed at the edge of the uplifted block along the lower boundary. The measured positions of the tensile cracks for three intervals of effective thickness are summarized in fig. 38. There is a

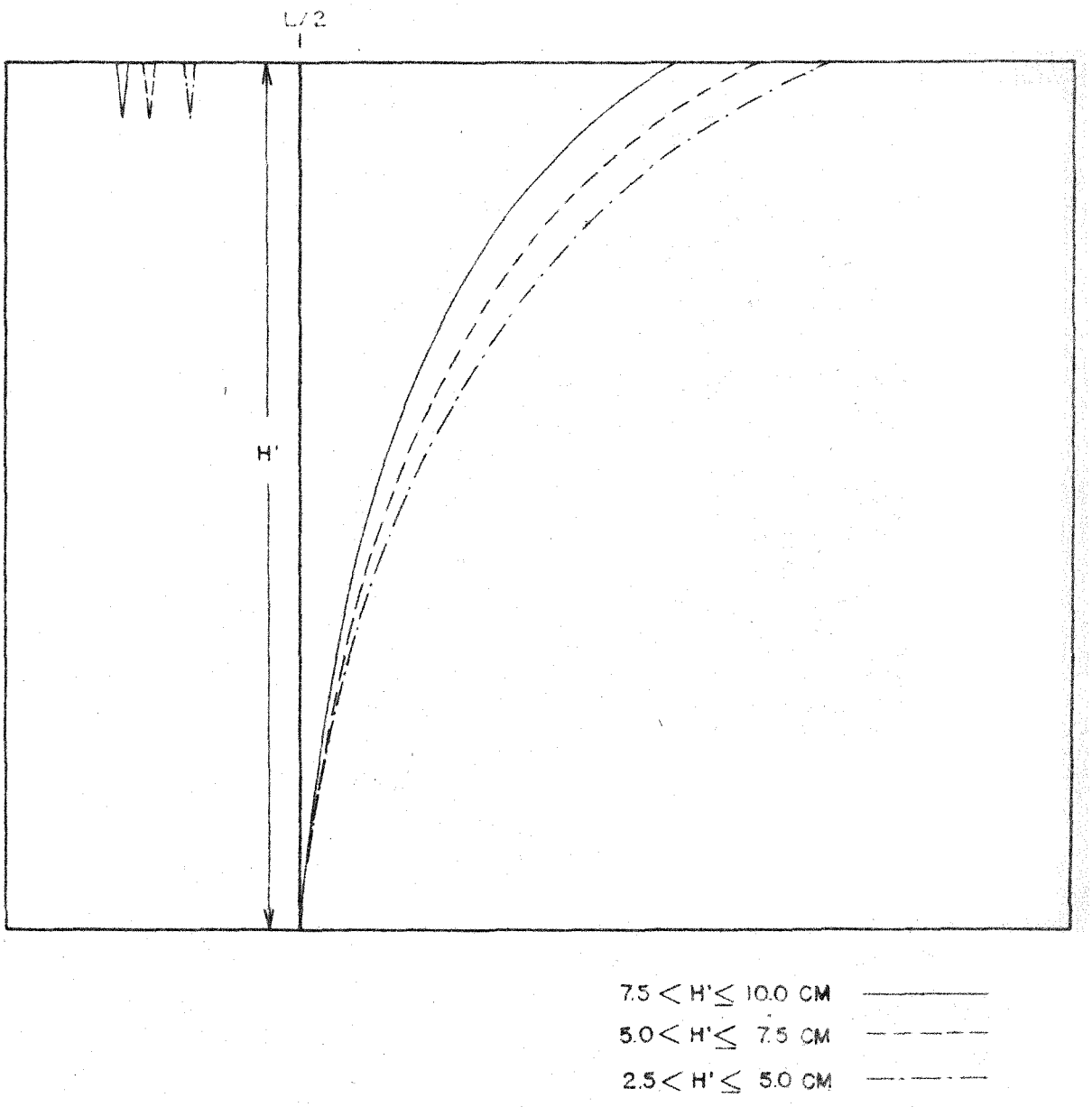

Figure 38. Curvature of reverse faults in Type II experiments.

systematic shift of the crack position with a change in the effective thickness of the layer.

Fracturing in the region of the tensile cracks followed the same pattern as the fracturing at the crest of the folds in the Type I experiments. The tensile cracks became deeper and wider with increased applied displacement. Eventually the crack reached a critical depth at which the material on each side of the crack was unable to support itself and normal fractures dipping towards the tension zone were formed. The maximum depth of the tensile cracks before normal faults were formed was 2.5 centimeters.

The final episode of fracturing in the experiments was the propagation of a steep normal fault (average dip 78 degrees) from the tensile crack zone to the edge of the uplifted block. After formation of the normal fault, displacement occurred along both the normal fault and the reverse faults. However, more displacement occurred along the normal fault than the reverse faults.

The sequence and characteristics of the fractures in Type II experiments were not affected by the initial strength (degree of compaction) of the layer. The fracturing in experiment B (figs. 36 and 37) in which the layer was initially weak (uncompacted) was the same as in the other experiments in which the layers were initially strong (moderately compacted).

The depth of the tensile cracks and the angle at which the reverse faults intersected the upper surface can be used to estimate the strength of the moderately compacted layers at the time of fracture. The computed cohesive strength from the maximum

depth of the tensile cracks is 600 c.g.s. The angle of internal friction from the average angle at which the fractures intersected the free upper surface (29 degrees) is 32 degrees. These values are fairly close to those obtained in the strength measurements on uncompacted layers of material 2.

Fractures with Materials 1 and 4. The fracture behavior of layers of materials 1 and 4 differed in two respects from the fracture behavior of layers of material 2: (1) tensile cracks were not formed (Nos. 8, P, and Q of fig. 36); and (2) the reverse faults formed were not sharp breaks, but narrow shear zones (No. Q of fig. 37). The curvature of the shear zones, however, was nearly identical to the curvature of the sharp reverse faults in the experiments with layers of material 2. Layers of material 1, which has a greater range in grain sizes and more irregularity in grain shape and roundness than material 4, had narrower zones of fracture than layers of material 4.

Deformation with Material 3. Folding rather than fracturing was the dominant type of deformation for experiments in which layers of material 3 were used. However, there were broad zones in the layers where the movement of the sand particles described trajectories (dashed line in No. I of fig. 36) which curved away from the uplifted block. In addition, ridges were formed on the upper surface similar to those associated with the reverse faults in the other experiments. Both of these features indicate that some characteristics of deformation with layers of material 3 are similar to the fracturing observed in the experiments with other model materials.

Summary of Experimental Results

The displacement fields, at small applied vertical displacements, appeared to be independent of the properties of the materials (size, shape, and sorting of the grains) used for the layers. Fracture, however, was influenced by the properties of the modeling materials. The sharpest fractures were formed in layers of material which had cohesive strength (material 2). The next sharpest fractures were formed in layers of material which lacked cohesive strength, but were composed of poorly sorted, irregularly shaped grains of sand (material 1). Layers composed of well sorted, well rounded, and spherical grains of sand did not appear to fracture (material 3).

Movement of the layer prior to the start of fracturing decreased the compaction of the material in the layer and thus reduced its strength. The strength of the layer at the time of fracturing was nearly the same as measured strengths of uncompacted layers.

Geologic Interpretation of the Experimental Results

Size Relationship Between Model and Geologic Structure

The relationship between the size of the model and the geologic structure that it represents is determined from equation (66). The model ratios of strength and density must be known to use this equation. Unfortunately, there is no means of estimating the strength of extensive layers of sedimentary rock in nature. The strength is probably determined to a large extent by the degree of fracturing and jointing in the layer. Layers of rock which have undergone

extensive jointing have no cohesive strength and probably react to applied vertical displacements like layers of material 1 do in the model experiments. Layers of rock which have not undergone jointing or faulting have a cohesive strength and probably react to applied vertical displacements like layers of material 2 do in the experiments.

A definite relationship between the size of a model and a geologic structure can not be established when the layer of rock in the geologic structure has no cohesive strength. A rock layer with no cohesive strength is generally modeled with a dry sand (similar to material 1) which also has no cohesive strength. If the angles of internal friction in the sand and the rock layer are equal, the strengths of the layers are identical. However, the cohesive strength of the rock layer is zero only if one considers an extensive layer. The individual pieces between joints have considerable cohesive strength. The strengths of the sand and rock layers will be identical only when the dimensions of individual blocks are related to the size of the rock layer in somewhat the same manner as the individual grains are related to the size of the sand layer.

A crude relationship between the model and the geologic structure can be obtained by comparing the size of sand grains with the size of joint blocks. The mean grain diameter for material 1 is 0.2 millimeters. A reasonable diameter for a joint block is 10 meters. The size relationship based on the above values is one centimeter of material 1 is equivalent to 0.5 kilometers of jointed rock.

A definite relationship between the size of the model and a geologic structure can be established when the layer of rock in the geologic structure has a cohesive strength. A layer with cohesive strength can be modeled with material 2 which has a very low cohesive strength, 1400 c.g.s., and an angle of internal friction of about 40 degrees. Representative values of cohesive strength and angle of internal friction for sedimentary rock are 250×10^6 c.g.s. and 40 degrees. The size relationship (from equation 66) between a layer of material 2 and a layer of rock with the strength properties above is one centimeter of material 2 equals 1.1 kilometers of rock.

The strength properties of (1) compacted layers of material 2, and (2) small rock samples (tested by the tri-axial method) have been used to establish the size relationship above. The strength of a layer of material 2 is considerably reduced by deformation of the layer prior to fracturing. A similar reduction in the strength of a layer of rock probably occurs in nature because of deformation before fracture. However, the strengths of the two layers may not be reduced in the same proportion, and the model ratio of their strengths will change. As a result, the possibility exists that the size relationship between the model and the geologic structure will change throughout the course of the experiment.

Fractures

Perhaps the most significant feature of the model experiments is the characteristic fracture pattern formed for each of

the two types of experiments. Each pattern is distinctive and relatively complex in view of the simplicity of the two distributions of applied displacement. The individual fractures in each pattern are related. Formation of one fracture triggers another in a definite sequence. The type and location of the primary fractures, which initiate the fracture sequence, are controlled by the distribution of applied displacement. The type and location of secondary fractures are determined partly by the distribution of applied displacement, and partly by conditions arising from the formation of the primary fractures.

The manner in which the fracture pattern forms in the two types of experiments suggests that other distributions of applied displacement at the base of a layer may also lead to distinctive fracture patterns. If the models are a true representation of fracturing in nature, fracture patterns observed in the models might be compared with fracture patterns observed on the surface of the earth, and in this manner be used to determine something about the distribution of displacement at depth.

The characteristic fracture pattern for Type I experiments is a complex zone of normal faults at the crest of the fold (see figs. 29 and 34). The fractured zone tapers inward to the axis of the fold, and dies out at depth. The Kettleman Hills anticline (Woodring, et al., 1940) is an excellent geologic example of a fold which has this type of fracture pattern.

The characteristic fracture pattern for Type II experiments is a series of curved reverse faults intersecting the upper surface

at low angles, and a series of normal faults in the uplifted block (see figs. 30 and 37). The most interesting fractures in the pattern are the reverse faults. Although they start as vertical faults at the lower boundary, they become thrusts at the upper boundary. The low angle or thrust portion of the fracture at the upper surface is due to horizontal compressive stresses. However, the horizontal compression is the result of vertical movement at depth and not of horizontal compression of the entire layer. Vertical movement at depth is an ideal mechanism for generating low angle thrusts in nature because the vertical movement required can be generated by a natural force--gravity.

Comparison of Experimental and Analytical Results

Type I Experiments and Category I Numerical Examples

Displacement Fields. The displacement fields in Type I experiments and Category I numerical examples are very similar, although this is not immediately apparent from an examination of the displacement field diagrams. Displacement fields in the analytical work (figs. 4 and 9) are produced by applied vertical displacements which change periodically in amplitude and direction. Displacement fields in the experimental work (fig. 33) are produced by applied vertical displacements which change in amplitude but not direction. Actually the only major difference between the two displacements fields is a uniform displacement in one direction. As previously noted, uniform movement of a layer does not change the stress distribution or distortional strain energy.

Therefore, superposition of a uniform upward displacement (equal to one-half the total amplitude of the applied vertical displacement) on the analytical displacement field will bring the two displacement fields into approximate agreement.

Although the general appearance of the displacement fields is similar, they differ considerably in detail. Listed below are the maximum vertical and horizontal displacements at the boundaries of the model and the corresponding theoretical displacements from fig. 19 (for the average H/L ratio of .85 in the experiments):

	Experimental	Theoretical
Vmax. Lower Boundary	1.00 B	1.00 B
Vmax. Upper Boundary	.60 B	.40 B
Umax. Lower Boundary	.30 B	0
Umax. Upper Boundary	.70 B	.30 B

(B equals the maximum applied vertical displacement.)

Two factors are responsible for most of the difference between theoretical and experimental values above. First, the boundary conditions in the experiments were different from the boundary conditions in the analytical examples. In the experiments, the applied vertical displacement did not vary exactly as the cosine of the horizontal distance, and horizontal displacement occurred along the lower boundary. Second, the displacements required in the experiments to record the displacement fields photographically were much larger than the critical displacements (Bc) in the analytical work. In nearly all of the experiments, there was

evidence of failure in the layer while photographing the displacement field.

Fractures. In the experiments with layers of material 2, the position of the vertical tensile cracks is the same as the position of the initial tensile fractures predicted in the numerical examples.

Type II Experiments and Category II Numerical Examples

Displacement Fields. The general appearance of the displacement fields in Type II experiments (fig. 35) and Category II examples (fig. 13) is very similar if a uniform upward displacement (equal to one-half the total amplitude of the applied displacement) is superposed on the analytical displacement field. However, the displacement fields differ slightly in detail. Listed below are the maximum vertical and horizontal displacements at the boundaries of the model and the corresponding theoretical displacements from fig. 21 (for the average H/L ratio of .47 in the experiments):

	Experimental	Theoretical
Vmax. Lower Boundary	1.00 B	1.00 B
Vmax. Upper Boundary	.95 B	.89 B
Umax. Lower Boundary	0	0
Umax. Upper Boundary	.60 B	.67 B

(B equals the maximum applied vertical displacement.)

The difference between the experimental and theoretical values above is small. In this case, the boundary conditions in the experimental work are nearly equivalent to the boundary conditions in the theoretical examples. Fracturing in the layer while photographing the

displacement fields probably accounts for most of the difference in the experimental and theoretical values.

Fractures. The predicted positions of the reverse faults in the Category II numerical examples are based on the stress distributions (figs. 13 and 15) and equation (57). The constant angle obtained from equation (57) is the orientation of the reverse faults with respect to the position of maximum compressive principal stresses throughout the layer. Inasmuch as the principal stress trajectories are curved, the reverse faults will also be curved. In fig. 39, three reverse faults based on the stress distributions have been drawn for three different angles of internal friction. Also shown on fig. 39 is a shear fracture based on measurements of reverse faults in model experiments which were geometrically similar to the numerical examples. The agreement between the experimental fracture and the theoretical fracture for a ϕ equal to 28 degrees is very good. A value of 28 degrees is a reasonable average angle of internal friction for the entire layer.

The tensile cracks in the experiments do not occur at the positions predicted in the analytical work (compare the position of tensile cracks on fig. 38 with the position of FP_1 on figs. 13 and 15). Apparently the formation of the reverse faults shifts the position of the large horizontal tensile stresses closer to the position of the reverse faults.

Elastic Solutions to Structural Problems from Models

Even with differences noted above, the agreement between analytical and experimental work is good. An elastic analysis is certainly a good first order approximation of the displacement

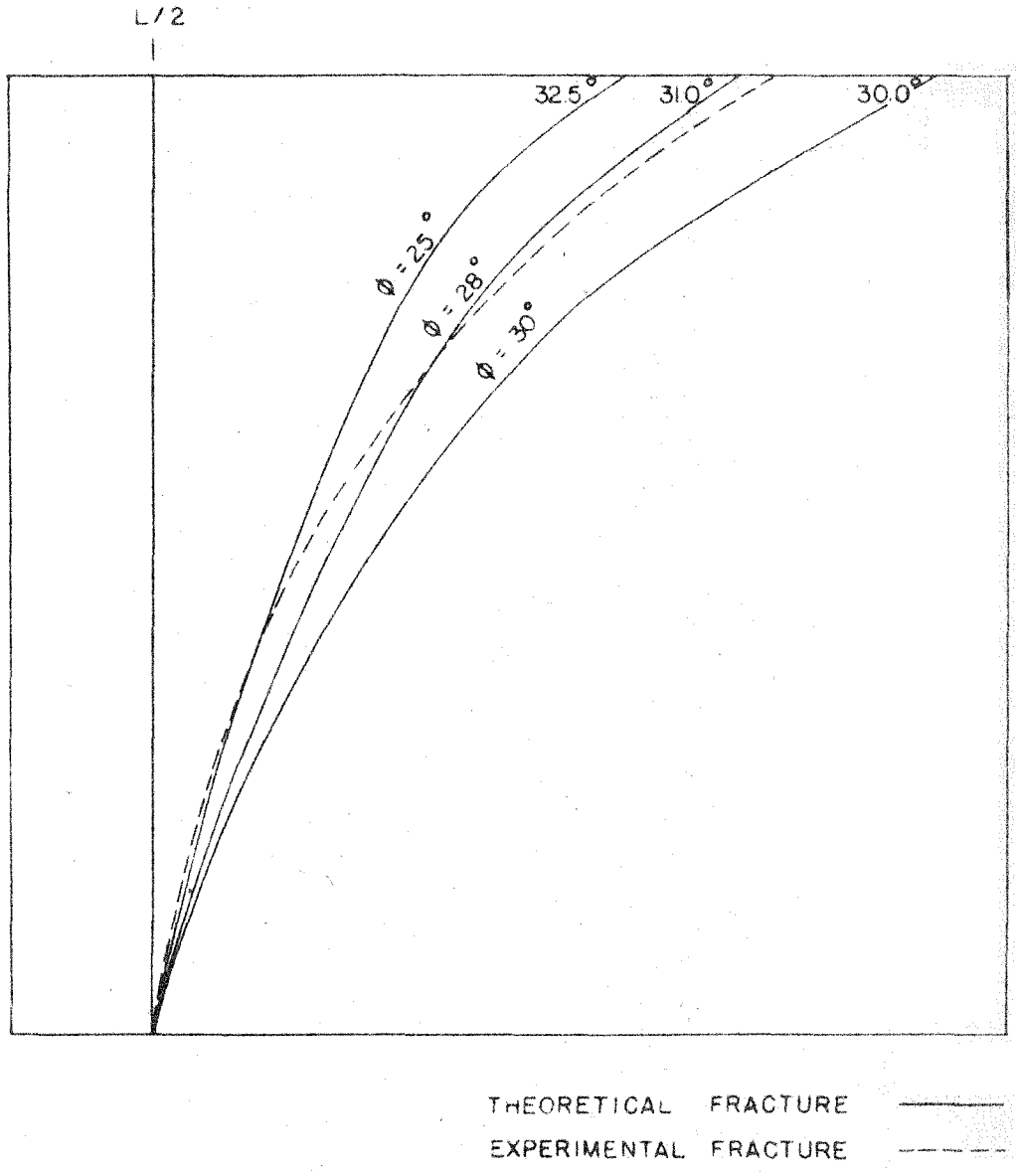

Figure 39. Comparison of theoretical and experimental fractures.

fields and the location of early fractures in the model experiments. In fact the agreement between the elastic analyses and models may be good enough to reverse the normal procedure and use the model experiments to solve elastic problems which are difficult to analyze with the standard elastic methods. The rates of change of the displacements with respect to the coordinates of the layer in the model displacement fields are related to the stresses. In addition, the lines of fracture have a definite angular relationship to the stress trajectories. Careful analyses of the model displacement fields can give the initial stress distributions. The location of the fractures will indicate what changes if any occur in the stress distributions after fracturing commences.

REFERENCES

Birch, F., et al., 1942, Handbook of physical constants: Geol. Soc. of Amer., Special paper no. 36, 325 p.

Gutenberg, B., 1951, Internal constitution of the earth, 2nd ed.: New York, Dover Publications, Inc., 438 p.

Hafner, W., 1951, Stress distributions and faulting: Bull. Geol. Soc. of Amer., v. 62, pp. 373-398.

Hodgman, C. D., 1955, Handbook of chemistry and physics, 37th ed.: Cleveland, Chemical Rubber Publishing Co., 3156 p.

Hubbert, M. K., 1937, Theory of scale models as applied to the study of geologic structures: Bull. Geol. Soc. of Amer., v. 48, pp. 1459-1520.

Hubbert, M. K., 1951, Mechanical basis for certain familiar geologic structures: Bull. Geol. Soc. of Amer., v. 62, pp. 355-372.

Jaeger, J. C., 1956, Elasticity, fracture, and flow: New York, John Wiley and Sons, Inc., 152 p.

Krumbein, W. C., and Sloss, L. L., 1951, Stratigraphy and sedimentation: San Francisco, W. H. Freeman and Co., 497 p.

Love, A. E. H., 1944, A treatise on the mathematical theory of elasticity, 4th ed.: New York, Dover Publications, Inc., 643 p.

Marin, J., 1952, Engineering materials: New York, Prentice Hall, Inc., 491 p.

Mills, A. P., et al., 1955, Materials of construction, 6th ed.: New York, John Wiley and Sons, Inc., 650 p.

Muskhelishvili, N. I., 1953, Some basic problems of the mathematical theory of elasticity, 3rd ed.: Groningen-Holland, P. Noordholf, Ltd., 704 p.

Phillips, H. B., 1933, Vector analysis: New York, John Wiley and Sons, Inc., 236 p.

Timoshenko, S., and Goodier, J. N., 1951, Theory of elasticity, 2nd ed.: New York, McGraw-Hill Book Co., Inc., 506 p.

Tschebotarioff, G., 1952, Soil mechanics, foundations, and earth structures, 1st ed.: New York, McGraw Hill Book Co., Inc., 655 p.

Woodring, W. P., Stewart, R., and Richards, R. W., 1940, Geology of the Kettleman Hills oil field, California: USGS, Professional paper no. 195, 170 p.

SECTION II

GRAVITY SURVEY OF A PART OF THE RAYMOND AND SAN GABRIEL BASINS, SOUTHERN CALIFORNIA

INTRODUCTION

The configuration of the bedrock surface underlying the eastern half of the Raymond basin and the adjacent northern margin of the San Gabriel basin is not well known. Surface mapping of the area has yielded little information because the region is covered with alluvial material. A few deep wells supply a small amount of information, but not enough to define the bedrock surface or answer other geologic questions. Important problems such as the displacement on the Raymond fault and the existence of Tertiary sedimentary rocks north of that fault can not be answered with the well data alone.

This report is based on a gravity survey. The work was started in 1954 and originally was confined to a detailed study of a four square mile area within the eastern part of the Raymond basin. Later the study was enlarged to a thirty-six square mile area which included the eastern part of the Raymond basin and the adjacent northern part of the San Gabriel basin.

DESCRIPTION OF THE AREA

The surveyed area lies within the southern California cities of Pasadena, Arcadia, Sierra Madre, and San Marino (fig. 40). The northern boundary ($34^{\circ}11'$N) is along New York Avenue in Pasadena and the base of the San Gabriel Mountains in Sierra Madre. The eastern boundary ($118^{\circ}02'$W) is along Santa Anita Avenue in Arcadia. The southern boundary ($34^{\circ}06'$N) follows Las Tunas Drive through the cities of Arcadia, San Gabriel, and Alhambra. The western boundary ($118^{\circ}08'$W) is along Lake Avenue in Pasadena

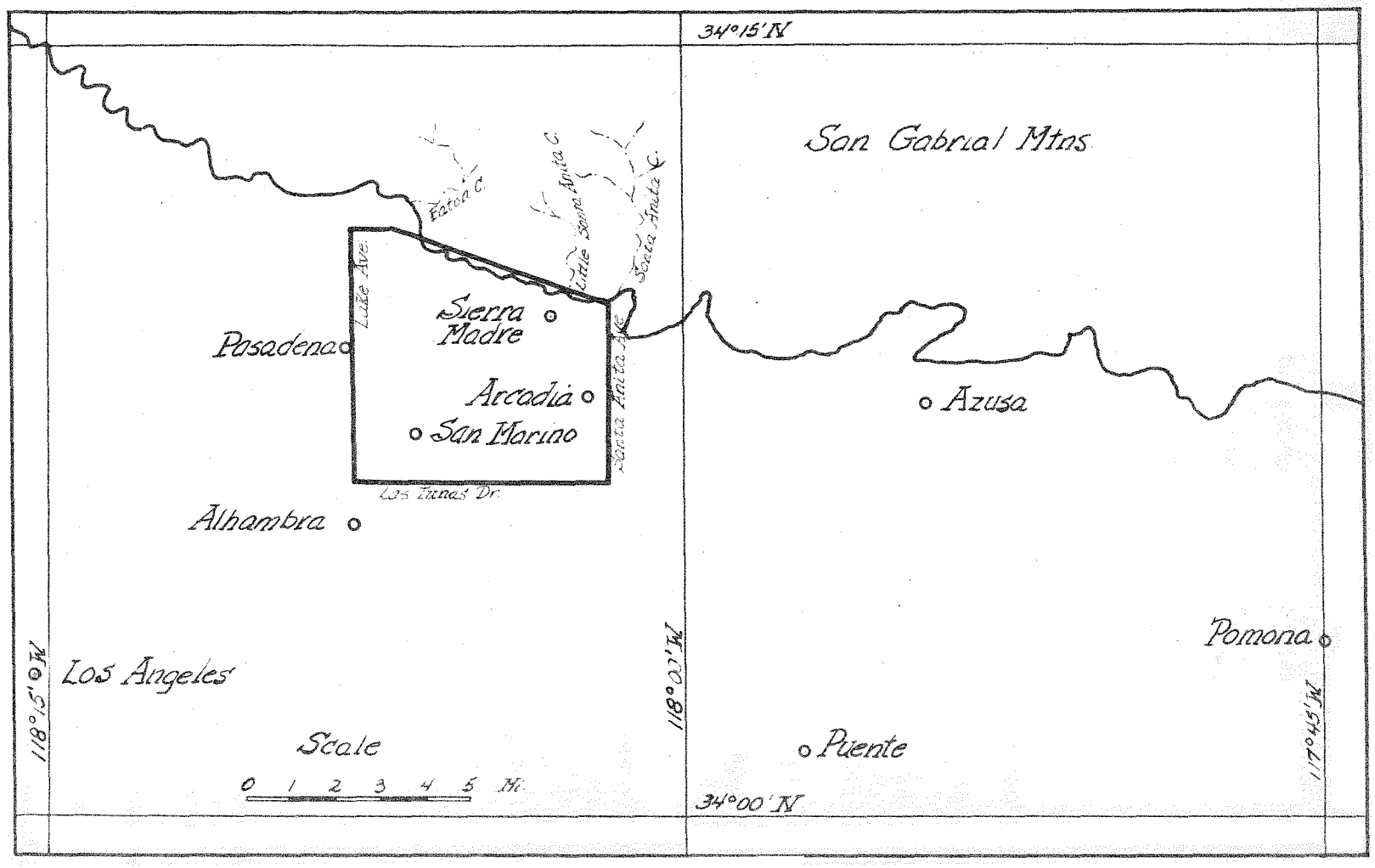

INDEX MAP

FIG 40

and the southward extension of this street into San Marino and Alhambra.

The alluvial surface over which the survey was conducted slopes southward from a maximum elevation of about 1200 feet along the northern boundary to a minimum elevation of about 400 feet along the southern boundary. The southward sloping alluvial surface is fairly smooth except for minor irregularities. A line of sharp bluffs and elongate hills passes through the central portion of the area. This alignment of bluffs and hills is the surface trace of the Raymond fault which separates the Raymond basin from the San Gabriel basin. A sharp straight bluff extends southeastward from the mouth of Eaton Canyon as far as Foothill Boulevard. The slope of the surface to the east of this feature is considerably steeper than that of the surface to the west. The other irregularities in the alluvial surface are the drainage channels which have been cut by streams flowing southward from Eaton, Little Santa Anita, and Santa Anita canyons in the San Gabriel Mountains.

GEOLOGY OF THE AREA

General Statement

The sub-surface geology of an area can not be determined from gravity data alone. The number of sub-surface mass distributions that satisfy a given surface distribution of gravity is infinite (Skeels, 1947). However, narrow limitations can be placed on the distribution of mass if sufficient geologic control is available (Nettleton, 1940, pp. 101-102, 119-121). Plate I and Table 3 summarize

the surface and sub-surface geologic information in the region of the survey. In the following sections, details of the stratigraphy and structure shown in Plate I are discussed with emphasis on the aspects important to a reasonable interpretation of the gravity data.

Stratigraphy

Principal Rock Groups

The three principal rock groups encountered on the surface or in wells in the area are Mesozoic basement rocks, Tertiary marine sedimentary rocks, and Quaternary alluvium.

Mesozoic Basement Rocks

The bedrock underlying the surveyed area is probably similar to the rock exposed in the San Gabriel Mountains, San Raphael Hills, and Monk Hill. These areas are composed of plutonic rocks (mainly of granitic and quartz dioritic composition), and metamorphic rocks (principally gneisses). Collectively, these rocks are called the Eastern bedrock complex.

The bedrock south of the Raymond fault may not be Eastern bedrock complex. Santa Monica slate was encountered in two oil wells near the western margin of the San Gabriel basin (Schoellhamer and Woodford, 1951). These wells are located about two miles south of the Raymond fault and four to six miles from the southwestern edge of the area of the gravity survey. If Santa Monica slate does exist south of the Raymond fault, it can not be detected from the gravity data because the densities of Santa Monica slate and Eastern bedrock complex are nearly the same -

2.76 ± .10 c.g.s. (Schoellhamer and Woodford, 1951).

Tertiary Marine Sedimentary Rocks

Surface exposures of Tertiary sedimentary rocks in the Raymond basin occur only between the Raymond and Eagle Rock faults. The rocks exposed in the four hills between these faults consist of massive conglomeritic sandstones and conglomerates with lesser amounts of interbedded shale. Water well data in the Raymond basin indicate that the Tertiary rocks extend eastward beneath the alluvium into the area of the gravity survey.

Total thicknesses of Tertiary rock in the Raymond basin are not known. Well C25d is the only well that possibly penetrated a significant thickness of Tertiary rock. This well was drilled to a depth of 1310 feet just south of the Eagle Rock fault. If the depth and location of this well are correct, about 1000 feet of Tertiary rock exists in this area (assuming the dip of the strata is not too great).

Tertiary rocks are exposed in the hills along the western margin of the San Gabriel basin. Well data indicate that Tertiary rocks extend eastward beneath the alluvium into the part of the San Gabriel basin covered in the survey. The Vosburgh oil well, located near the southeastern corner of the surveyed area, gives evidence for a thick section of Tertiary rock in the eastern part of the San Gabriel basin. This well is reported to have penetrated 3500 feet of Tertiary rock without reaching bedrock (Oakeshott, et al., 1952; Conkling, 1927, p. 94).

The relative ages of Tertiary rock in the Raymond and

San Gabriel basins are not important in the interpretation of the gravity data. All Tertiary rocks in the area, regardless of age, have nearly the same density - 2.35 c.g.s. (Peterson, 1935, p. 31).

Quaternary Alluvium

Two types of alluvium, Old (Upper Pleistocene (Eckis, 1934, p. 57)) and Recent, occur in the area. Most of the present surface of the area is composed of Old alluvium. The Old alluvium is a yellow to dark red, unconsolidated, aggregation of varying proportions of gravel, sand, and clay. The relative percentages of gravel, sand, and clay in the Old alluvium (from logs of water wells in Pasadena) are 48.5, 2.9, 48.6, respectively (Eckis, 1934, p. 100). Most of the clay is derived from the decomposition of the feldspathic minerals in the sands and gravels. The percentage of residual clay is considered an index of the length of time since the deposition of the alluvium.

The density of the Old alluvium is difficult to estimate. Increase in density with depth of burial is possible because of the high clay content of the Old alluvium. Density at the surface probably averages about 2.0 c.g.s. (Birch, et al., 1944, pp. 19-20) whereas at depth the density may approach that of Tertiary rocks.

In the Eaton, Little Santa Anita, and Santa Anita washes, and in south Arcadia, the surface is covered with Recent alluvium. The Recent alluvium is white to gray, low in clay content (probably less than 10%), and probably a little lower in average density

than the Old alluvium. Thick deposits of the Recent alluvium could be a major problem in the interpretation of the gravity data. Two lines of evidence suggest that deposits of Recent alluvium are thin. Drill holes (Buwalda, 1940) and gravel pits in Eaton wash encountered clayey material (Old alluvium) 26 to 70 feet below the surface. The relative percentages of gravel, sand, and clay in the alluvium penetrated by wells in the San Gabriel-Arcadia area are, 43.5, 10.9, and 45.7, respectively (Eckis, 1934, p. 100). The covering of Recent alluvium in the San Gabriel-Arcadia area must be fairly thin for these percentages to be nearly identical to those found for Old alluvium alone. Inasmuch as the deposits of Recent alluvium appear to be thin, the lower density of these deposits can be neglected without producing a significant error in the gravity interpretation.

Thicknesses of alluvium in the Raymond and San Gabriel basins are given in the seventh column of Table 3. The thicknesses are fairly well known in the western half of the Raymond basin where a large number of water wells were drilled through the alluvium and bottomed in either Mesozoic basement rock or Tertiary rock. In the surveyed area, thickness information from wells is sparse and in some cases questionable. Nine wells are reported to have been drilled through alluvium into either bedrock or Tertiary rock. Some of these wells, C115, C40, C42, and C104b, did not penetrate enough bedrock to eliminate the alternate possibility of large boulders in the alluvium. However, the reliable well data does give some indication of the thicknesses of alluvium.

In general, the alluvium thickens southeastward from the western margin of the area. Some representative thicknesses in the area are: 934 feet (C127) near the western boundary, 1150 feet (C87c) near the center, and 1400 feet (Vosburgh oil well) near the southeastern margin. The elevation of the base of alluvium at the three well locations above are 44 feet, 510 feet, and 1050 feet below sea level. These figures indicate considerable subsidence of the area since the start of alluvium deposition.

Structure

Regional Structure

The fault pattern in southern California includes two principal fracture sets. One set trends northwest with predominately right-hand strike-slip movement. The other set trends west with predominately reverse dip-slip movement. The survey was made in an area in which three faults (see below) of the second set occur. These faults have formed the boundaries of the San Gabriel and Raymond basins and are the most important structural features in the area.

Sierra Madre Fault Zone

The Sierra Madre fault zone is a crooked, braided, complex fault zone along the base of the San Gabriel Mountains. The average dip (mostly from evidence to the east of the Raymond basin) of the faults in this zone is 60 degrees north. In the Pasadena area, the block north of the fault zone has moved up a minimum of 5000 feet with respect to the block south of the fault zone (Eckis, 1934, pp. 72-74).

Raymond Fault

The surface expression of the Raymond fault is a line of sharp bluffs, elongate hills, and closed depressions in the alluvial surface. Sub-surface evidence of the Raymond fault is the difference in water levels on opposite sides of the fault. Ground water levels on the Raymond basin side of the fault are 200 to 300 feet higher than the water levels just south of the fault (Eckis, 1934, Plate E). Seams of gouge along the fault surface in the alluvium have prevented southward migration of ground water. Irregularities in the surface trace (Buwalda, 1940), and long narrow subsidiary ground water basins parallel to the north side of the fault, suggest that the Raymond fault is a system of fractures rather than a single fracture.

The southward facing scarps along the fault indicate that the north side of the fault has been displaced upward relative to the south side. The maximum height of these scarps is about 150 feet. In all probability, the heights of these scarps represent only the last episodes of movement on the fault. The sub-surface geologic information gives no indication of the total vertical displacement along any section of the fault. However, the depth to Tertiary rock at well C202c, which is located a short distance south of Raymond Hill (where Tertiary rock is exposed at the surface), is evidence for at least 222 feet of displacement since the deposition of the Old alluvium.

The dip of the fractures along the Raymond fault is probably about 70 degrees north (Buwalda, 1940). Deep water wells, a few hundred feet north of the surface trace, have water levels

considerably closer to those in the Raymond basin than to those in the San Gabriel basin. The fault surface must be fairly steep or some of these wells would have passed through the fault and encountered water at the San Gabriel basin level (200 to 300 feet lower than the Raymond basin). This ground water evidence does not exclude the possibility of normal rather than steep reverse faults. The strongest argument for reverse faults is the nature of faulting elsewhere in the area. All major faults in the region are reverse, including the faults of the Sierra Madre fault zone which the Raymond fault joins a short distance east of Arcadia.

Eagle Rock Fault

The east-west Eagle Rock fault, which brings crystalline rock on the north into juxtaposition with Tertiary rock on the south, can be traced on the surface from Glendale to the Arroyo Seco in Pasadena. East of the Arroyo Seco, the fault can not be followed on the surface because it is covered with undisturbed alluvial material. However, the surface exposures of Tertiary strata and the sub-surface distribution of the crystalline and Tertiary rocks define the position of the fault fairly well to a point just north of the intersection of Glenarm Street and Fair Oaks Avenue in Pasadena (see Plate I). On the basis of the sub-surface information, there appear to be two alternate courses for the fault to follow from this point. First, it could continue its southeasterly trend and join the Raymond fault south of Lake Avenue. Second, it could swing straight east and parallel the Raymond fault for a considerable distance. If the first course is

selected, Tertiary sediments must exist north of the Eagle Rock fault in the Pasadena area. If the second course is selected, all Tertiary sediments could be south of the Eagle Rock fault. Total displacements on the Eagle Rock fault are not known. Well C25d, if the depth figure is correct, indicates a minimum displacement of about 1000 feet near the eastern margin of the Raymond basin.

Other Faults

Miller (1928) describes two additional faults which possibly exist within the area. Miller believes that, "The distinct, straight scarp, extending from the mouth of Eaton Canyon three miles southeasterly in Quaternary alluvial material, is probably the result of late Quaternary faulting, though it may possibly be interpreted as an erosional effect. The fault idea is supported by the existence of a nearly wedge-shaped area of older gravels on the north lying between the scarp and the Sierra Madre fault. This area of gravel is quite certainly on an uplifted fault block". Eckis (1934, Plate E) has published ground water information which favors the existence of a fault at the above location. In January, 1933, water levels were higher east of this scarp than west. In addition, Eckis found that the specific yield of alluvial material east of the scarp was considerably lower than that to the west. The lower specific yield east of the proposed fault may be due to a higher than normal clay content for the Old alluvium. This might indicate that the alluvial material of this area is somewhat older than that found elsewhere in the region.

The second fault described by Miller (1928) extends westward from Glendora to Arcadia. In Arcadia, the fault

intersects the Raymond fault just below Colorado Boulevard. Miller cites well data which indicate that this fault has 1000 feet of vertical displacement with the north side up relative to the south side.

SURVEY PROCEDURE

Instrument

The instrument used in the gravity survey was a Worden gravity meter (No. 236 E) manufactured by Houston Technical Laboratories, Houston, Texas. The range of this instrument was 472 milligals with a sensitivity of approximately $\pm$ .025 milligals. The normal drift rate at constant temperature was + .02 milligals per hour. Under extreme increases in temperature, for example 10°F per hour, the instrument drifted as much as -.35 milligals per hour.

Field Procedure

Stations Occupied

A majority of the 640 stations in the survey were local elevation bench marks placed by engineering departments of the cities of Pasadena, Arcadia, and San Marino. In addition, United States Coast and Geodetic Survey bench marks were used. The accuracy of these station elevations was $\pm$ 0.1 feet. In special areas, stations were surveyed by the writer with an accuracy of $\pm$ 0.5 feet. A few stations along the margins of the area were placed at street intersections where elevations were recorded to the nearest foot on United States Geological Survey topographic

sheets. The relative inaccuracy of the latter two groups of bench marks was not serious inasmuch as the meter was only sensitive to changes in the elevation of approximately 0.5 feet.

Reading Procedure

The procedure followed was to occupy a base station, take readings at a series of stations, and return to the original base station at least once every hour. During periods of rapid temperature change, the base stations were reoccupied every one-half hour until a linear drift rate was established. All base stations were tied to a master station by repeated runs in short periods of time. Another reading check used in the survey was a random reoccupation of stations. During the survey, sixty-eight stations were occupied more than once. The maximum difference encountered at a single one of these stations was 0.16 milligals; the average was 0.06 milligals.

REDUCTION OF DATA

Latitude, Tidal, and Drift Corrections

The latitude, tidal, and drift corrections were made in the usual manner. A correction of 0.023 milligals per 100 feet was used for the latitude interval between 34° 06'N and 34° 11'N. Tidal and drift corrections were obtained by frequent reoccupation of base stations.

Elevation Corrections

The horizontal reference surface selected for elevation corrections intersected the southward sloping alluvial surface

near its maximum elevation (1200 feet) in the surveyed area. The wedge shaped gap between the reference surface and the southward sloping alluvial surface was assumed to be filled with material of the same density as the alluvium at the surface (2.0 c.g.s.). A combined Free Air and Bouguer correction (-0.0685 milligals per foot) was used to obtain a first order approximation of the gravity values at points on the reference surface directly above the actual station locations (Nettleton, 1940, p. 54).

Topography Correction

The San Gabriel Mountains rise to a height of 5000 feet within three miles of the northern margin of the surveyed area. These mountains, the southward slope of the alluvial surface, and other irregularities in topography in or near the area, had a strong effect on the gravity readings. The procedure used in calculating topographic corrections for the gravity data was suggested by Professor C. H. Dix. The topography of the region was divided into horizontal layers of specified thicknesses. A horizontal sheet passing through the center of each layer was assigned a surface density equal to $h\rho$, where h is the thickness of the layer and ρ its density. The attraction of each sheet at a given station was calculated by means of the following equation:

$$g_T = \sigma K H \Delta\theta \sum_{n=1}^{n} \frac{1}{r_i}$$

where

σ = surface density of each sheet.

K = gravitational constant.

H = difference in elevation between gravity station and each sheet.

$\Delta\theta$ = angle (in radians) between radial lines on a circular graticle.

n = number of $\Delta\theta$ intervals intersecting each sheet.

r_i = distances from station to center of sheet measured along the radial lines of the graticle.

Two assumptions were made in calculating topographic corrections for the area. First, the density of each layer was constant. Layers below an elevation of +1250 feet were assigned a density of 2.0 c.g.s., and those above a density of 2.7 c.g.s. Thus for correction purposes, the San Gabriel Mountains were considered a series of horizontal high density layers above a series of horizontal low density layers. The model adopted was not an accurate representation of the geologic situation. The substitution of low density material for the high density material existing beneath the mountains made the corrections too small, particularly near the mountain front.

The second assumption was that all layers extended from the mountain front to infinity. In other words, no allowance was made for valleys behind the San Gabriel mountain front. This made the corrections too large, particularly near the mountain front. The two assumptions made in the corrections lead to errors which cancel to some extent.

Even with these simplifying assumptions, the time required for a single correction prevented the calculation of corrections for each station. Instead corrections for thirty-five points scattered throughout the area were found, placed on a map, and contoured. Topographic corrections were applied by graphically

superposing this map and the gravity map obtained after elevation and latitude corrections.

On the topographic correction map, the lines of equal topographic correction were very smooth and paralleled the San Gabriel Mountain front. The maximum correction was 10 milligals at the mountain front, the minimum was 1.4 milligals six miles from the mountain front.

Regional Gravity Correction

The distribution of gravity obtained after all of the above corrections was dependent on deep crustal structure as well as near surface structure. The regional gravity due to deep crustal structure had to be separated from the total gravity before a correct interpretation of the near surface structure could be made. Several factors permitted the determination of a reasonably accurate regional gravity map for the surveyed area:

1. The density discontinuities contributing to the regional gravity were relatively deep with respect to the linear dimensions of the area. For example, the Mohorovicic discontinuity (which may have a density contrast of about 0.5 c.g.s. across it) was 35 kilometers deep, whereas the sides of the area were about 10 kilometers long (Gutenberg, 1951, pp. 357-360; Press, 1956). In view of the relationship between the size of the area and the depths of the density discontinuities, the assumption was made that the regional gravity was constant in direction and gradient throughout the surveyed area.

2. The surface geology of the area (Plate I) suggested that contours of equal gravity should parallel the San Gabriel Mountains along the mountain front after removal of the regional gravity. The gravity contours were parallel to the mountain front without the regional gravity removed. Therefore, the most reasonable direction for contours of equal regional gravity was the strike of the mountain front.

3. Gravity observations were made at points where the near surface geology was known. Theoretical differences in gravity between a base station and each occupied station were computed on the basis of the near surface geology. The theoretical differences in gravity were compared with the corresponding differences in observed gravity. A fairly uniform distribution of differences between observed and theoretical values was obtained in regions where geologic control was available.

The regional gravity map constructed after consideration of the factors listed above is shown on the inset of Plate II.

INTERPRETATION

Regional Structure

The direction of the regional gravity found in this survey agrees with the southern California regional gravity pattern obtained by the United States Coast and Geodetic Survey (Duerksen, 1949) (Plate II). However, there are differences in the gradient

of the regional gravity between the two surveys. The USCGS data show a smaller gradient to the northeast in the area of this writer's survey. In the USCGS data, however, no corrections were made for the lower density material above the bedrock in the Raymond and San Gabriel basins.

The regional gravity indicates a thickening of the earth's crust to the northeast. If all of the regional gravity is attributed to a density difference of 0.5 c.g.s. at the Mohorovicic discontinuity, the rate of thickening to the northeast is about 500 feet per mile or 100 meters per kilometer.

The USCGS gravity data on Plate II show a northeastward thickening of the crust for a considerable distance beyond the San Gabriel Mountains. In addition, Press (1956) has concluded that the crust is unaffected by the Transverse ranges (which include the San Gabriel Mountains) on the basis of thicknesses obtained from studies of the phase velocities of Rayleigh waves. Therefore, the observed thickening of the crust in the surveyed area does not appear to be an indication of a "root" beneath the San Gabriel Mountains.

Near Surface Geology

Gravity Map

The gravity map obtained after all corrections were applied is shown in Plate III. This map can be interpreted as a contour map of the bedrock surface. The interpretation is only approximate because irregularities in the bedrock surface are smoothed out by the gravity readings. On the gravity map, a

change of one milligal in gravity corresponds to a change of about 150 feet in bedrock elevation. The number of feet per milligal is higher in the southern portion of the area where Tertiary strata as well as alluvium lie above bedrock. The bedrock elevations at Monk Hill, the San Gabriel mountain front, and well C127 are 1150 feet, 1200 feet, and -44 feet, respectively. These elevations can be used with the gravity data on Plate III to compute approximate bedrock elevations throughout the area.

Most of the major features of the bedrock surface are shown on the gravity map. Two of the most interesting bedrock features are valleys in the Raymond basin. One valley extends eastward from well C127, the other southeastward from the intersection of Allen Avenue and New York Avenue. These two valleys meet near Wilson Junior High School.

The large number of wells drilled to basement in the western half of the Raymond basin define the position of the east-west valley up to the western margin of the surveyed area (Buwalda, 1940). Observed bedrock elevations at Monk Hill, well C127, and well C31f are 1150 feet, -44 feet, and 459 feet, respectively. Well C127 appears to be near the center of the valley. The gradient of the east-west valley, on the basis of the gravity data, is about 300 to 450 feet per mile. This high gradient is indicative of mountainous terrain.

The second valley trends N 30 W from Wilson Junior High School to St. Luke Hospital. North of the hospital the direction of the valley changes to about N 50 W. The bedrock elevation at the center of the valley near the intersection of

Allen Avenue and New York Avenue must be +100 feet or lower. This elevation is about 1100 feet below the elevation of bedrock exposures at Monk Hill and the San Gabriel mountain front. The computed gradient for this valley is about 300 feet per mile.

North of St. Luke Hospital shallow bedrock exposures indicate that the bedrock valley must lie west of the present Eaton wash. Bedrock is exposed on both sides of Eaton wash 4600 feet north of the hospital. Further north on the western edge of the wash, well C115 encountered bedrock 52 feet below the surface.

South of St. Luke Hospital the eastern margin of the valley appears to follow the course of the surface scarp which Miller (1928) considered a possible fault feature. The gravity map shows a change in bedrock slope along the scarp. The bedrock slope, just like the surface slope, is steeper on the east side of the scarp than on the west side. Unfrotunately, there is no means of telling from the gravity data whether the change in bedrock slope results from bedrock erosion, faulting, or a combination of the two.

The bedrock topography map in Buwalda's report (1940) shows a bedrock ridge projecting southward from the mountain front to well C43a. This ridge is based on a reported bedrock elevation of +687 feet at well C43a. This depth must be in error. The gravity value at C43a is nearly the same as the value at C52a. The latter well was drilled to -429 feet without reaching bedrock. Wells C42 and C40 north of C43a also have reported depths to bedrock which are not compatible with the gravity data. Both of these wells did not penetrate enough bedrock to exclude

the possibility of boulders in the alluvium.

The gravity map shows a rapid steepening of the bedrock surface near the mountain front. This steepening is substantiated by two wells, C40c and C40e, which are located within 1500 feet of exposures of bedrock at the mountain front. These wells are reported to have penetrated 400 to 500 feet of alluvium.

Geologic Sections

Construction of Geologic Sections.

Two geologic sections (Plate IV) have been constructed from the gravity, well, and surface information. The interpretations made on these sections are geologically reasonable and in agreement with the available well and surface data. However, other interpretations may be possible. Reliable check points for the gravity calculations, such as deep wells, are widely separated. As a result, considerable latitude is possible in making the geologic sections from the gravity data.

The geologic sections were constructed by determining the difference in bedrock elevation between well C127 and points along the section lines. Well C127 was selected as a base station for these calculations because of its reliable bedrock depth and its location. No sharp irregularities in the bedrock surface exist near this well which could influence the gravity value at the well location.

Differences in bedrock elevation were determined by the Bouguer formula (Nettleton, 1940, p. 54). This formula must be used with caution as it will give incorrect depths in areas of

extreme bedrock relief. Wells were projected into the section lines along the gravity contour passing through each well location. This procedure may lead to errors in depth at the section lines. Changes in the average density of the material above the bedrock surface can destroy any direct correspondence between a gravity contour line and a bedrock elevation contour line.

Section AA'. A density contrast of 0.5 c.g.s. between bedrock and alluvium was used for calculation of bedrock elevation along section AA'. Computed and observed bedrock depths did not agree at well C104b. The computed depth to bedrock was 500 feet lower than the reported depth. The error in computed depth was averaged out in a three mile interval extending westward from the well.

Inasmuch as many factors can cause variations in the gravity values, it is not surprising that the bedrock depths computed with the Bouguer formula at well C104b and other points in the area do not agree with the known depths. Unknown lateral changes in the density contrast between alluvium and bedrock can lead to errors in the computed depths. The gravity values themselves may not be correct due to the imperfect nature of the elevation, topography, and regional corrections. In view of all the factors which might lead to errors, the computed depths at well C104b and other points in the area are remarkably close to the known depths.

Section AA' shows a smooth decrease in bedrock elevation from -44 feet at well C127 to -1000 feet at Sierra Madre Villa Boulevard. Eastward from this point the bedrock surface rises gradually to an elevation of +75 feet at well C104b.

Section BB'. The bedrock depth at the intersection of

lines AA' and BB' was used as a base point for bedrock elevation calculations on line BB'. Initially, computations were made with a density contrast of 0.5 c.g.s. between bedrock and overlying material (shown by dashed line on section BB'). This density contrast gave a bedrock elevation at least 1100 feet above bedrock at the Vosburgh oil well. This well bottomed in Tertiary rock at about 4500 feet below sea level. The Vosburgh well and other evidence cited below suggested the existence of a wedge of Tertiary strata between the alluvium and the bedrock surface. A wedge of Tertiary rock 3500 feet thick at the Vosburgh well and zero feet thick at the base point appeared reasonable on the basis of the geologic information. A density contrast of 0.15 c.g.s. between alluvium and Tertiary rock was used for calculating the effect of the wedge of Tertiary rock. The bedrock surface after correction for the Tertiary strata is shown by a solid line on section BB'.

The anomaly shown on the gravity profile for line BB' has been interpreted as a fault. The center of the anomaly is about 800 feet south of the surface trace of the Raymond fault. The computed bedrock displacement is about 600 feet. The interpretation of the Raymond fault shown on the geologic section is based on the geologic information previously cited.

The Tertiary rock-alluvium contact at the Vosburgh well is 1050 feet below sea level. The same contact at the El Rancho oil well 8000 feet southeast of the Vosburgh well is 1560 feet below sea level (see Plate I). On the basis of this well data, a

dip of one degree south for the Tertiary rock-alluvium contact has been assumed for the segment of section BB' south of the Raymond fault. North of the fault this contact probably slopes northward. Well C87c is reported to have penetrated shale (Tertiary?) at -510 feet, an elevation somewhat below the Tertiary rock-alluvium contact just north of the Raymond fault.

Surface geology suggests that the Tertiary rock-alluvium contact should be nearest the surface just north of the Raymond fault. Line BB' crosses an east-west lense-shaped hill just north of the surface trace of the fault. Buwalda (1940) has interpreted the hill as a fault block of alluvium which is older than the Old alluvium on the surface near the hill. A block of ancient alluvium is more likely to be faulted to the surface if the layer of alluvium is thin.

The distribution of gravity west of line BB' and north of the Raymond fault is also possible evidence for the existence of Tertiary sediments north of the Raymond fault. The bedrock valleys shown in Plate III meet near Wilson Junior High School and form a single valley which extends southward across the Raymond fault. Although the gravity control is poor in this area, there can be no question that the southward slope of gravity is greater in the lower valley than in the two upper valleys. Transposing the gravity slope to bedrock slope (density contrast equal to 0.5 c.g.s.) gives a bedrock gradient of 600 to 700 feet per mile in the lower valley. This is nearly twice the maximum gradient of the upper valleys. One would normally expect the

same or a somewhat lower gradient below the junction of the two valleys. However, the distribution of gravity south of Wilson Junior High does not have to be interpreted as a steep gradient valley cut in bedrock. A valley cut in Tertiary rock at the same gradient as the upper valleys can also give the same distribution of gravity. In the latter case, the increased southward slope of gravity is due to a northward pointing wedge of Tertiary rock between the alluvium and the bedrock.

Well data support the interpretation made above. Two wells located near the center of the lower valley, C120a and C87c, are reported to have bottomed in shale (Tertiary?). Both wells were drilled about fifty years ago and thus their data are subject to question. However, well C120a penetrated 100 feet of shale which makes the report difficult to ignore despite the early drilling date. The depth to shale at well C87c is about 300 feet deeper than at well C120a. The gravity value at C87c is about 0.6 milligals lower than C120a. If one assumes the same depth to bedrock at both wells, the observed difference in gravity, and depth to shale, can be explained by a 0.15 c.g.s. density contrast between the alluvium and the shale.

Summary

In the northern part of the surveyed area, the peaks and valleys in the bedrock surface beneath the alluvium indicate bedrock relief equal in magnitude to the present surface of the San Raphael Hills. The bedrock relief is more uniform in the southern part of the area where Tertiary rock lies between bedrock and alluvium. This intermediate layer of Tertiary rock may extend

northward more than a mile into the Raymond basin.

The elevations to the base of the alluvium demonstrate at least 1000 feet of subsidence since Upper Pleistocene time. The subsidence and corresponding rise in base level have caused the deposition of alluvium which now covers nearly all the major bedrock features.

A vertical bedrock displacement of about 600 feet has occurred along at least one section of the Raymond fault, probably since the deposition of the Tertiary rock. North of the Raymond fault, the gravity data give no indication of an eastward extension of the Eagle Rock fault parallel to the Raymond fault.

Table 3. Well Data for the Raymond and San Gabriel Basins

Well No.	Year Drilled	Elev.-Top of Well	Elev.-Bottom of Well	Total Depth	Elev.-Base of Alluvium	Thickness of Alluvium	Minimum Thickness of Tertiary Rock	Rock at the Bottom of the Well
C6	1918	1151	578	573	578	563	0	Bdrk.
C6a	1929	1134	433	701	433	686	0	Bdrk.
C7	1909	1109	543	566	543	542	0	Bdrk.
C8	1916	1085	625	460	625	448	0	Bdrk.
C10	1921	1046	850	196	850	190	0	Bdrk.
C10a	1903	997	489	508	489?	508?	0	Bdrk?
C11	1922	1189	409	780	409	775	0	Bdrk.
C12	1919	1130	625	505	643	487	0	Bdrk.
C13	1912	1122	614	508	-	-	-	Alluvium
C14	1918	1109	484	625	501	608	0	Bdrk.
C16	1921	917	217	700	237	680	0	Bdrk.
C17	1902	943	192	751	194	749	0	Bdrk.
C20	1921	775	674	101	677	98	0	Bdrk?
C23a	1907	764	665	99	758	8	0	Bdrk.
C23f	1938	643	177	466	389	254	212	Tert. rk?
C24a	1931	753	558	195	-	-	-	Tert. rk?
C25a	1916	757	577	180	625	131	49	Tert. rk.
C25b	1927	757	582	175	605	152	0	Bdrk.
C25d	1899	802	-508	1310	-	-	-	Tert. rk.
C26	1901	756	588	168	588	168	0	Tert. rk.
C27	1911	755	496	259	550	205	54	Tert. rk.
C30e	1910	753	468	285	478	275	10	Tert. rk.
C30l	1891	755	625	130	657	98	32	Tert. rk.
C30m	1903	756	226	530	521	235	295	Tert. rk.
C31a	1925	772	582	190	589	183	0	Bdrk.

Table 3. (Continued)

Well No.	Year Drilled	Elev.-Top of Well	Elev.-Bottom of Well	Total Depth	Elev.-Base of Alluvium	Thickness of Alluvium	Minimum Thickness of Tertiary Rock	Rock at the Bottom of the Well
C31e	1931	758	548	210	558	200	0	Bdrk.
C31f	1931	794	442	352	459	335	0	Bdrk.
C40	1924	953	635	318	637	316	0	Bdrk.
C40b	1926	936	383	553	-	-	-	Alluvium
C40c	1922	1330	697	633	850	480	0	Bdrk.
C40d	1930	916	442	474	-	-	-	Alluvium
C40e	1923	1335	865	470	905?	430?	0	Bdrk?
C42	1924	865	415	450	417	448	0	Bdrk.
C43a	1906	802	580	222	687	115	0	Bdrk.
C44	1924	876	-214	1089	-	-	-	Alluvium
C52a	1930	791	-429	1220	-	-	-	Alluvium
C56	1920	715	478	237	533?	182?	55?	Tert. rk?
C57a	1931	701	-33	734	387?	314?	420?	Tert. rk?
C58	1922	714	229	485	231	483	2	Tert. rk
C63	?	665	305	360	317	348	12	Tert. rk
C64	1923?	639	279	360	?	?	?	?
C80a	1932	591	-311	902	-	-	-	Alluvium
C87c	?	640	-510	1150	-510	1150	-	Tert. rk?
C104b	1928	503	73	430	75	428	0	Bdrk.
C106	1907	753	447	306	453	300	6	Tert. rk.
C110a	1919	698	-76	774	-	-	-	Alluvium
C111	1934	776	161	615	-	-	-	Alluvium
C115	?	1115	1063	52	1063	52?	0?	Bdrk.
C120a	1905	655	-297	952	-199	854	98+	Tert. rk?
C127	1926	890	-63	953	-44	934	0	Bdrk.

Table 3. (Continued)

Well No.	Year Drilled	Elev.-Top of Well	Elev.-Bottom of Well	Total Depth	Elev.-Base of Alluvium	Thickness of Alluvium	Minimum Thickness of Tertiary Rock	Rock at the Bottom of the Well
C130	1920	676	217	459	-	-	-	Alluvium
C134	1926	708	-21	729	-	-	-	Alluvium
C201	1925	506	-279	785	-	-	-	Alluvium
C201a	1925	498	-304	802	-	-	-	Alluvium
C201b	1925	546	-56	602	-	-	-	Alluvium
C201c	1928	547	-244	791	-	-	-	Alluvium
C202	1930	561	56	505	-	-	-	Alluvium
C202a	1921	520	16	504	196	308	180	Tert. rk?
C202c	1921	681	459	222	-	-	-	Tert. rk.
C206	1923	534	-27	561	-	-	-	Alluvium
A1	1956	493	-307	800	-	-	-	Alluvium
VOW	1925	350	-4525	4875	-1050	1400	3475	Tert. rk.
EROW	1934?	340	-1560	1900	-1560	1900	-	Tert. rk.

VOW - Vosburgh Oil Well

EROW - El Rancho Oil Well

REFERENCES

Birch, F., et al., 1944, Handbook of physical constants: Geol. Soc. of Amer., Special paper no. 36, 325 p.

Buwalda, J., 1940, Geology of the Raymond basin: Unpublished report for the Pasadena Water Dept., 130 p.

Conkling, H., 1927, San Gabriel investigation: Calif. Dept. of Public Works, Div. of Water Rights, Bull. no. 5.

Eckis, R., 1934, South coastal basin investigation - geology and ground water storage capacity of valley fill: Calif. Dept. of Public Works, Div. of Water Resources, Bull. no. 45, 273 p.

Duerksen, J., 1944, Pendulum gravity data in the United States: U. S. Dept. of Commerce, Coast and Geodetic Survey, Special publication no. 244, 218 p.

Gutenberg, B., 1951, Internal constitution of the earth, 2nd ed.: New York, Dover Publications, Inc., 438 p.

Miller, W., 1928, Geomorphology of the southwestern San Gabriel Mountains of California: Univ. of Calif. Publications, Bull. Dept. of Geol. Sciences, v. 17, no. 6, pp. 194-227.

Nettleton, L., 1940, Geophysical prospecting for oil, 1st ed.: New York, McGraw Hill Book Co., Inc., 444 p.

Oakeschott, G., et al., 1952, Exploratory wells drilled outside of oil and gas fields in California to Dec. 31, 1950: Calif. Div. of Mines, Special paper no. 23, 77 p.

Peterson, R., 1935, Results of gravity measurements in southern California: Unpublished Ph. D. Thesis, Calif. Inst. of Tech.

Press, F., 1956, Determination of crustal structure from phase velocity of Rayleigh waves, Part I: Southern California: Bull. Geol. Soc. of Amer., v. 67, pp. 1647-1658.

Schoellhamer, J. and Woodford, A., 1951, The floor of the Los Angeles basin, Los Angeles, Orange, and San Bernardino counties, California: U. S. Geol. Surv., Oil and Gas Inv., map OM 117, 2 sheets.

Skeels, D., 1947, Ambiguity in gravity interpretation: Geophysics, v. 12, no. 1, p. 43.